Large Eddy Simulation of Wall-bounded Turbulent Flows Using

Discontinuous Spectral Element Method

by

Seyyed Ziaoddin Ghiasi
B.S., University of Tehran, Tehran, Iran, 2011
M.S., University of Illinois at Chicago, Chicago, IL, United States, 2017

Thesis submitted in partial fulfillment of the requirements
for the degree of Doctor of Philosophy in Mechanical Engineering
in the Graduate College of the
University of Illinois at Chicago, 2018

Chicago, Illinois

Defense Committee:
Farzad Mashayek, Chair and Advisor
Committee members:
Suresh K. Aggarwal
Kenneth Brezinsky
Gustaaf Jacobs, San Diego State University
W.J. Minkowycz

To my parents,

my brother,

and my sister.

ACKNOWLEDGMENTS

ACKNOWLEDGMENTS (Continued)

TABLE OF CONTENTS

TABLE OF CONTENTS (Continued)

LIST OF TABLES

LIST OF FIGURES

LIST OF ABBREVIATIONS

0D	Zero-Dimensional
1D	One-Dimensional
2D	Two-Dimensional
3D	Three-Dimensional
BFS	Backward-Facing Step
CMSM	Chebyshev Multidomain Spectral Method
CFD	Computational Fluid Dynamics
CFL	Courant-Friedrichs-Lewy
CMTL	Computational Multiphase Research Laboratory
DChT	Discrete Chebyshev Transform
DCT	Discrete Cosine Transform
DES	Detached Eddy Simulation
DNS	Direct Numerical Simulation
DSEM	Discontinuous Spectral Element Method
ENO	Essentially Non-Oscillatory
FD	Finite Difference
EV	Entropy Viscosity

FFT	Fast Fourier Transform
FFTW	Fastest Fourier Transform in the West
FMDF	Filtered Mass Density Function
GGG	Gauss-Gauss-Gauss
GGL	Gauss-Gauss-Lobatto
GLG	Gauss-Lobatto-Gauss
iDChT	Inverse Discrete Chebyshev Transform
iDCT	Inverse Discrete Cosine Transform
ILES	Implicit Large Eddy Simulation
IP	Interpolant-Projection
LES	Large Eddy Simulation
LGG	Lobatto-Gauss-Gauss
MWR	Method of Weighted Residuals
NS	Navier-Stokes
ODE	Ordinary Differential Equation
PDE	Partial Differential Equation
PDF	Probability Density Function
PoC	Proof of Concept

LIST OF ABBREVIATIONS (Continued)

RMS   Root-Mean-Square

SFS   SubFilter-Scale

SGS   SubGrid-Scale

STE   Scalar Transport Equation

TKE   Turbulence Kinetic Energy

WENO   Weighted Essentially Non-Oscillatory

SUMMARY

The objective of the present dissertation is to develop numerical tools and techniques that facilitate the high-fidelity simulations of the air flow within ramp-cavity combustors using a discontinuous spectral element method. The supersonic turbulent reacting flow within the ramp-cavity combustor is a multi-scale, multi-physics, complex flow. The concurrent presence of shocks, turbulence, and reaction, as well as their interactions, make the simulation of such a flow one of the most challenging ones in the field of computational fluid dynamics. There have been efforts to simulate such a flow using low-order numerical schemes such as finite volume and finite difference, but a high-order method that is capable of dealing with the entire physics of the flow is highly desired. Spectral element methods provide high accuracy, are flexible with complex geometries, and can be efficiently parallelized. The focus of the present work is on the turbulence aspect of the flow. A new explicit modal filtering procedure is introduced, implemented, and tested for use in large eddy simulations without any sub-grid scale model. The method is tested for isotropic turbulence and turbulent flow in a channel, and accurate mean and fluctuation statistics are obtained comparing with direct numerical simulation. The computational overhead of the proposed method is less than 3% (compared to 45% for dynamic Smagorinsky model). Moreover, a sensor that improves the performance of the standard Smagorinsky model for separating flows is developed, implemented, and tested for a backward-facing step configuration. The error of the prediction of the reattachment length is reduced from 18.4% to 0.5% by applying the proposed sensor. The near-wall spatial

SUMMARY (Continued)

resolution requirement for direct numerical simulations of wall-bounded turbulent flows is also studied in detail. It is shown that the near-wall resolution requirement strongly depends on the approximation order; for an approximation order of $P = 7$, eight grid points within $y^+ = 10$ is sufficient for accurate statistics, while for an approximation order of $P = 2$, even having 11 points within $y^+ = 10$ results in inaccurate statistics. Preliminary steps are also taken towards the simulations of turbulent supersonic flows. Large-eddy simulations of non-reactive turbulent supersonic flow in a ramp-cavity combustor with fuel injector are presented.

CHAPTER 1

INTRODUCTION

The present work is a part of the ongoing research on the high-fidelity simulation of supersonic turbulent reacting flows in ramp-cavity (RC) combustors in the Computational Multiphase Transport Laboratory (CMTL) of the University of Illinois at Chicago. The focus of the present dissertation is on direct numerical simulations (DNS) and large eddy simulations (LES) of wall-bounded turbulent flows, especially channel flows and separating and reattaching flows. The accurate and efficient simulation of such flows is a crucial step towards the simulation of ramp-cavity combustors.

Separating and reattaching fluid flows have numerous applications in diverse industries including automotive, aviation, and energy. Prime examples of separating flows occur in dump combustors, turbine and compressor blades, diffusers, stalled airfoils, buildings, suddenly expanding pipes, etc. The research on separating flows emerged as Ludwig Prandtl presented the boundary layer theory (2) in the early twentieth century. The flow separates from the surface of an object when the boundary layer moves far enough against an adverse pressure gradient that the relative speed of the boundary layer to the object falls near to zero (3; 4). The flow detaches from the surface and instead forms eddies and vortices. The characteristics of separated flows have been studied through experiments for decades to understand better the physical mechanisms that govern the flow separation, its instability, and the large coherent structures associated with it.

Due to the expensive nature of the experiments and the limitations associated with them, numerical simulations became favorable, especially after the emergence of powerful computers. Researchers in the field of computational fluid dynamics (CFD) have employed various numerical methods to perform flow simulations by solving the Navier-Stokes equations or their variations. Even though the numerical simulations have proven to be a promising alternative to experiments, they come with their own complications. Numerical stability, computational cost, calculations accuracy, and correct case setup including boundary and initial conditions are among the numerous challenges associated with CFD simulations. An ideal numerical simulation is straightforward to set up, provides accurate results, and requires a reasonable amount of time to complete. However, especially in industrial applications, one usually compromises between accuracy and manageability based on their need.

High-order numerical methods are preferred over low-order methods because of their potential to deliver higher accuracy with lower cost. A k-th order numerical scheme is a scheme that its error, e, is proportional to h^k, where h is the mesh size. In some CFD communities, the term *high-order* methods may refer to the methods with order three or higher; however, in general (and in this work), the high-order method refers to spectral methods (5). Spectral methods use basis functions that are non-zero over the whole domain or at least over the whole sub-domain (element). The error in spectral methods decreases exponentially (called exponential or spectral convergence) for smooth solutions, which makes them more accurate than local methods such as finite element methods.

Direct numerical simulations directly solve the Navier-Stokes equations to calculate the whole range of time and spatial scales of the flow. Since most flows in engineering applications are highly turbulent, the time and spatial scales span an extensive range. Covering the full range of scales demands excessively refined mesh and small time stepping and becomes nearly impossible for very high Reynolds number flows due to the limitations in computational power and resources. Therefore, turbulence modeling techniques, such as large eddy simulation (LES), are often employed to simulate most of the engineering problems. In LES, the motions are separated into small and large scales by applying a filter on the velocity field. Then, the large scales are directly calculated by solving the filtered Navier-Stokes equations, and the effects of the small scales on the large-scale motions are often modeled by various methods such as applying eddy viscosity.

Simulations of turbulent supersonic reacting flows in three-dimensional (3D) ramp-cavity combustors is a prime example of practical problems that deal with separating flows and involve multiple flow physics. The simultaneous presence of shocks, turbulent structures, turbulent boundary layer, turbulent shear layer, fuel injectors, and reaction makes this problem one of the most challenging ones in CFD. The existence of each of those flow components require extensive care to achieve stability and accuracy of the computations, while their interactions with each other add to the complexity of the simulation. Generating a mesh that meets the resolution requirements while maintaining a reasonable computational cost is another major challenge in this problem.

The majority of the previous numerical simulations of high-speed combustors are performed using RANS or LES/RANS. This is due to the complexity of the problem. RANS simulations are more manageable and computationally less expensive than LES; however, they do not provide detailed unsteady characteristics of the flow. Also, most of the previous simulations are performed using low-order methods of finite volume or finite difference (FD). Developing a high-order scheme, which is able to perform LES of such a complex flow, is extremely challenging, but will immensely help achieve a deeper understanding of the physics of such flow and mechanisms that govern the interactions of different phenomena in the flow.

The objective of the present dissertation is to develop and implement numerical tools and techniques that facilitate the process of simulating the turbulent supersonic reacting flows in 3D ramp-cavity combustors using a high-order method. A discontinuous spectral element method (DSEM) is employed to implement the tools and techniques and perform the simulations in this work.

The first step in setting up a CFD simulation, after determining the geometry of the problem, is to generate a mesh. An ideal mesh (i) provides sufficient resolution in different regions of the domain to provide the required accuracy and stability and (ii) does not hugely affect the simulation's computational cost due to extremely small grid sizes. The grid generation near the walls for simulations of turbulent flows requires additional care due to the sensitivity of the boundary layer to the grid. Determining the adequate and efficient grid resolution in the vicinity of the wall needs even more considerations in DSEM or any other numerical method that uses the Chebyshev distribution of points. A low near-wall resolution results in inaccurate statistics

and a high resolution hugely increases the computational cost due to the non-uniformity nature of the Chebyshev points. A comprehensive study on the near-wall resolution requirement for DNS of turbulent flows using DSEM is performed by simulating a 3D periodic channel flow using different grid resolutions and different polynomial orders and is presented in chapter 3. The effect of the polynomial order on the near-wall resolution requirement is also studied in detail. This study is a prerequisite for the DNS of the turbulent flow over the backward-facing step (BFS) in chapter 5.

Performing DNS of the turbulent supersonic reacting flow in a ramp-cavity combustor is extremely expensive in terms of the computational cost due to the complexity of the geometry, small-scales of turbulence and reaction, and the small time step size demanded by the reaction. Therefore, LES of such complex flow is highly desired. Two LES turbulence models are considered in this work: (i) A modal filtering technique is proposed, and (ii) the standard Samagorinsky model is improved for the separating flows.

Developing a turbulence model that is computationally inexpensive and compatible with the nature of the numerical scheme is a crucial step in expanding the application of DSEM for LES of turbulent flows in complex geometries. In chapter 4, an element-level modal low-pass explicit filtering procedure, which operates in the spectral space, is introduced. The modal filter is implemented in the DSEM, and its application is studied for LES without a subgrid-scale (SGS) model. The method is tested for a configuration featuring 3D isotropic decaying turbulence, and its performance is compared with a previously used method—a spectral interpolation-based nodal filter. The filtering procedure is also applied to a 3D turbulent channel flow, and the

results are compared with those from the DNS. An anisotropic version of the modal filter, which damps high-frequency modes in a specific direction, is also introduced and tested for the channel flow case.

The accurate LES of the BFS geometry is the preliminary step in the successful simulation of turbulent flow over a ramp-cavity. The BFS geometry may be considered the same as an RC geometry without the ramp. The BFS flow is a well-studied benchmark, and its successful simulations ensure that the numerical method is capable of accurately simulating the shear layer that is formed at the step and exists in both BFS and RC geometries. The standard Smagorinsky model is one of the popular turbulence models due to its manageability, simplicity of implementation, and low cost. However, it is well known that the model performs poorly in the vicinity of walls by introducing excessive artificial viscosity in those areas. A sensor that improves the performance of the standard Smagorinsky model for separating flows is developed and is introduced in chapter 5. The sensor, which is a function of only density, time, and space, differentiates between the high turbulent activity areas and the near-wall regions. The sensor is implemented and tested in conjunction with the standard Smagorinsky model, and its performance is studied for the flow over a BFS. The addition of this sensor to the Smagorinsky model prevents the eddy viscosity model to introduce excessive and undesired viscosity to the near-wall region and consequently improves the prediction of the flow statistics and considerably enhances the accuracy of the model. A DNS of 3D turbulent flow over BFS is also performed and compared with previous work to validate our numerical method for such flow and also to provide a benchmark for LES simulations of the same problem.

LES of turbulent supersonic flow in a 3D ramp-cavity combustor is also performed using DSEM and is presented in chapter 6. An entropy viscosity (EV) shock capturing technique (6) is used to handle the shocks generated downstream of the cavity, and standard Smagorinsky model is used for turbulence modeling. A sensor is also introduced and implemented that differentiates between turbulence areas and shock regions and prevents the turbulence model to introduce undesired artificial viscosity in the shock regions. The flow is simulated for two configurations: with and without an injector on the ramped wall of the cavity. The effect of the injector on the flow characteristics are studied by comparing the results from the two cases. The effect of the Reynolds number on the shock wave is also demonstrated.

The governing equations, as well as the numerical method used in this work, are presented in chapter 2. The near-wall resolution requirements for DNS of turbulent flow using DSEM is studied in chapter 3. Chapter 4 presents the modal filtering technique. The DNS of BFS, as well as the LES of BFS using the Smagorinsky model and the wall sensor, is presented in chapter 5. The simulation of turbulent supersonic flow in a ramp-cavity combustor with the injector is presented in chapter 6. Finally, a summary of the work and the important conclusions are drawn in chapter 7. Also, the background and previous work relating to each aspect of the present work is provided in their corresponding chapter.

CHAPTER 2

GOVERNING EQUATIONS AND NUMERICAL METHOD

In this chapter, the governing equations of the problems that are addressed in this work, i.e., the Navier-Stokes equations, are presented in detail. Moreover, the details of the numerical method employed, i.e., the discontinuous spectral element method (DSEM), are described.

2.1 Governing Equations

In this section, the governing equations are presented in both dimensional and non-dimensional forms. The non-dimensional form of the equations are used in this work.

2.1.1 Dimensional Form

The governing equations of the problems addressed in this work are the 3D equations of motion for an unsteady compressible Newtonian fluid. The dimensional equations of mass, momentum, and energy, i.e. the Navier-Stokes equations, are presented in a conservative form in Cartesian coordinates as

$$\vec{Q}_{t^*}^* + \vec{F}_{x^*}^{a*} + \vec{G}_{y^*}^{a*} + \vec{H}_{z^*}^{a*} = \vec{F}_{x^*}^{v*} + \vec{G}_{y^*}^{v*} + \vec{H}_{z^*}^{v*}, \tag{2.1}$$

8

where the arrow indicates a vector, and the star superscript denotes dimensional variables. In

Equation 2.1,

$$\vec{Q}^* = \begin{bmatrix} \rho^* \\ \rho^* u^* \\ \rho^* v^* \\ \rho^* w^* \\ \rho^* e^* \end{bmatrix} \tag{2.2}$$

is the solution vector, where ρ^* is the density, u^*, v^*, and w^* are three components of velocity,

and

$$\rho^* e^* = \rho^* c_v^* T^* + \frac{1}{2}\rho^* (u^{*2} + v^{*2} + w^{*2}), \tag{2.3}$$

is the sum of internal and kinetic energy per unit volume, where c_v^* is the constant volume specific heat, and T^* is the temperature. The advective fluxes in Equation 2.1 are defined by

$$\vec{F}^{a*} = \begin{bmatrix} \rho^* u^* \\ p^* + \rho^* u^{*2} \\ \rho^* u^* v^* \\ \rho^* u^* w^* \\ u^* (\rho^* e^* + p^*) \end{bmatrix}, \quad \vec{G}^{a*} = \begin{bmatrix} \rho^* v^* \\ \rho^* u^* v^* \\ p^* + \rho^* v^{*2} \\ \rho^* v^* w^* \\ v^* (\rho^* e^* + p^*) \end{bmatrix},$$

$$\vec{H}^{a*} = \begin{bmatrix} \rho^* w^* \\ \rho^* u^* w^* \\ \rho^* v^* w^* \\ p^* + \rho^* w^{*2} \\ w^* (\rho^* e^* + p^*) \end{bmatrix}, \tag{2.4}$$

where p^* is the pressure. The viscous fluxes are defined by

$$\vec{F}^{v*} = \begin{bmatrix} 0 \\ \tau_{11}^* \\ \tau_{12}^* \\ \tau_{13}^* \\ u^*\tau_{11}^* + v^*\tau_{12}^* + w^*\tau_{13}^* + \kappa^* T_{x^*}^* \end{bmatrix},$$

$$\vec{G}^{v*} = \begin{bmatrix} 0 \\ \tau_{21}^* \\ \tau_{22}^* \\ \tau_{23}^* \\ u^*\tau_{21}^* + v\tau_{22}^* + w^*\tau_{23}^* + \kappa^* T_{y^*}^* \end{bmatrix},$$

$$\vec{H}^{v*} = \begin{bmatrix} \tau_{31}^* \\ \tau_{32}^* \\ \tau_{33}^* \\ u^*\tau_{31}^* + v^*\tau_{32}^* + w^*\tau_{33}^* + \kappa^* T_{z^*}^* \end{bmatrix}, \tag{2.5}$$

where κ^* is the fluid's conductivity, and

$$\tau_{11}^* = 2\mu^*[u_{x^*}^* - (u_{x^*}^* + v_{y^*}^* + w_{z^*}^*)/3],$$

$$\tau_{22}^* = 2\mu^*[v_{y^*}^* - (u_{x^*}^* + v_{y^*}^* + w_{z^*}^*)/3],$$

$$\tau_{33}^* = 2\mu^*[w_{z^*}^* - (u_{x^*}^* + v_{y^*}^* + w_{z^*}^*)/3],$$

$$\tau_{12}^* = \tau_{21}^* = \mu^*[v_{x^*}^* + u_{y^*}^*],$$

$$\tau_{13}^* = \tau_{31}^* = \mu^*[w_{x^*}^* + u_{z^*}^*],$$

$$\tau_{23}^* = \tau_{32}^* = \mu^*[w_{y^*}^* + v_{z^*}^*],$$

are the components of the stress tensor, where μ^* is the fluid's dynamic viscosity. The subscripts of the components of the stress tensor, τ_{ij}^*, denote the direction of the stress and the plane it is acting on, where 1, 2, and 3 represent the x-, y-, and z-directions. The non-dimensional total energy is

$$\rho e = \frac{p}{\gamma - 1} + \rho \frac{u^2 + v^2 + w^2}{2} \tag{2.6}$$

The assumptions made regarding the governing equations in this work are as follows:

- It is assumed that the bulk viscosity of the fluid, μ_b^*, is zero, i.e., $\mu_b^* = 3\lambda^* + 2\mu^* = 0$. This assumption is known as *Stokes hypothsis*.

- It is also assumed that the Fourier's law governs the heat flux in the energy equation. The Fourier's law is given, e.g., in the x-direction by $q_1^* = -\kappa^* T_{x^*}^*$, where q^* is the heat flux, and its subscript indicates its direction.

- The viscosity, conductivity, and specific heats of the fluid are generally functions of temperature. However, for the range of temperature fluctuations in this work, the changes in the above-mentioned quantities are not very significant ($< 10\%$). Therefore, it is assumed that those quantities are not a dependent on the temperature.

- The fluid is an ideal gas, and its properties follow the ideal gas law, i.e., $p^* = \rho^* R^* T^*$, where R^* is the gas constant. The addition of the equation of state to the Navier-Stokes equations closes the governing equations by providing the sixth equation for the six unknowns, i.e., ρ^*, u^*, v^*, w^*, p^*, and T^*.

2.1.2   Non-dimensional Form

In this work, the governing equations are employed in the non-dimensional form since the disparity of the physical variables can cause numerical errors. Therefore, all variables are non-dimensionalized using the reference length, L_f^*, reference density, ρ_f^*, reference velocity, U_f^*, and reference temperature, T_f^*. The non-dimensionalized variables are given by

$$
\begin{aligned}
\rho &= \rho^*/\rho_f^*, & u &= u^*/U_f^*, \\
v &= v^*/U_f^*, & w &= w^*/U_f^*, \\
T &= T^*/T_f^*, & p &= p^*/(\rho_f^* U_f^{*2}), \\
x &= x^*/L_f^*, & y &= y^*/L_f^*, \\
z &= z^*/L_f^*, & t &= t^* U_f^*/L_f^*.
\end{aligned}
\tag{2.7}
$$

Applying the same non-dimensionalization to Equation 2.1 generates the governing equations

in the non-dimensional form, given by

$$\overrightarrow{Q}_t + \overrightarrow{F}^a_x + \overrightarrow{G}^a_y + \overrightarrow{H}^a_z = \frac{1}{Re_f}\left(\overrightarrow{F}^v_x + \overrightarrow{G}^v_y + \overrightarrow{H}^v_z\right). \tag{2.8}$$

In Equation 2.8,

$$\overrightarrow{Q} = \begin{bmatrix} \rho \\ \rho u \\ \rho v \\ \rho w \\ \rho e \end{bmatrix} \tag{2.9}$$

is the solution vector, where

$$\rho e = \frac{p}{\gamma - 1} + \frac{1}{2}\rho(u^2 + v^2 + w^2). \tag{2.10}$$

Also,

$$\vec{F}^a = \begin{bmatrix} \rho u \\ p + \rho u^2 \\ \rho uv \\ \rho uw \\ u(\rho e + p) \end{bmatrix}, \quad \vec{G}^a = \begin{bmatrix} \rho v \\ \rho uv \\ p + \rho v^2 \\ \rho vw \\ v(\rho e + p) \end{bmatrix}, \quad \vec{H}^a = \begin{bmatrix} \rho w \\ \rho uw \\ \rho vw \\ p + \rho w^2 \\ w(\rho e + p) \end{bmatrix} \tag{2.11}$$

are the vectors of advective fluxes, and

$$\vec{F}^v = \begin{bmatrix} 0 \\ \tau_{11} \\ \tau_{12} \\ \tau_{13} \\ u\tau_{11} + v\tau_{12} + w\tau_{13} + \frac{1}{(\gamma-1)M_f^2 Pr}T_x \end{bmatrix},$$

$$\vec{G}^v = \begin{bmatrix} 0 \\ \tau_{21} \\ \tau_{22} \\ \tau_{23} \\ u\tau_{21} + v\tau_{22} + w\tau_{23} + \frac{1}{(\gamma-1)M_f^2 Pr}T_y \end{bmatrix},$$

$$\vec{H}^v = \begin{bmatrix} 0 \\ \tau_{31} \\ \tau_{32} \\ \tau_{33} \\ u\tau_{31} + v\tau_{32} + w\tau_{33} + \frac{1}{(\gamma-1)M_f^2 Pr}T_z \end{bmatrix} \qquad (2.12)$$

are the vectors of viscous fluxes, where

$$
\begin{aligned}
\tau_{11} &= 2[u_x - (u_x + v_y + w_z)/3], \\[6pt]
\tau_{22} &= 2[v_y - (u_x + v_y + w_z)/3], \\[6pt]
\tau_{33} &= 2[w_z - (u_x + v_y + w_z)/3], \\[6pt]
\tau_{12} &= \tau_{21} = v_x + u_y, \\[6pt]
\tau_{13} &= \tau_{31} = w_x + u_z, \\[6pt]
\tau_{23} &= \tau_{23} = w_y + v_z.
\end{aligned}
\tag{2.13}
$$

Three non-dimensional parameters are generated during the non-dimensionalization process:

- The reference Reynolds number measures the domination of the effects of the advective fluxes over the effects of the viscous fluxes. and is defined by $Re_f = \rho_f^* U_F^* L_f^* / \mu^*$.

- The Prandtl number measures the ratio of momentum diffusivity to thermal diffusivity and is defined by $Pr = c_p^* \mu^* / \kappa^*$, where c_p^* is the constant pressure specific heat.

- The reference Mach number is defined by $M_f = U_f^* / c^*$, where c^* is the reference speed of sound, defined by $c^* = \sqrt{\gamma R^* T_f^*}$, and γ is the heat capacity ratio of the fluid.

The equation of state is presented in the non-dimensional form as

$$
p = \frac{\rho T}{\gamma M_f^2}.
\tag{2.14}
$$

2.2   Numerical Method

In this work, the discontinuous spectral element method (DSEM) is used to discretize the governing equations, Equation 2.8. The DSEM is based on the conservative staggered-grid Chebyshev multidomain spectral method (CMSM), which was first introduced by Kopriva (7; 8; 9) in two dimensions. Later, the method was extended for three dimensions by Jacobs (10). The DSEM has negligible diffusion and dispersion errors and is spectrally convergent within each element for smooth solutions (7; 9). The method has been employed for DNS and large eddy simulations (LES) of compressible flow in complex geometries (11; 12; 13). In the DSEM, the governing equations are solve locally inside the elements; therefore, the method is flexible with complex geometries, allows for local grid refinement, and provides parallelization efficiency. The capability of simulating supersonic flows and capturing shocks distinguishes the DSEM from most spectral element codes. The method solves the governing equations of compressible flows and allows for discontinuity of the solution on interfaces of the elements. The discretization procedure in DSEM is described in the next sections. In section 2.2.1, the discretization is explained for a 1D scalar equation. The extension of the discretization method for a 3D euler equation is presented in section 2.2.2. In section 2.2.3 the extension to the the full 3D Navier-Stokes equations is provided.

2.2.1   1D Scalar Equation

In this section, the discretization procedure in DSEM is described. We start with a one-dimensional (1D) scalar equation in conservative form,

$$u_t + f_x(u) = 0, \quad a \le x \le b, \tag{2.15}$$

where u is the solution unknown, and f is the flux. The interval $[a, b]$ is subdivided into multiple, non-overlapping subdomains, or the so-called elements. The elements are then transformed to unit intervals using an isoparametric mapping. After the mapping, the governing equation becomes

$$u_t + \frac{1}{x_X} f_X(u) = 0, \quad 0 \le X \le 1. \tag{2.16}$$

Two staggered sets of points are placed inside each mapped element: the Gauss points, defined by

$$X_{j+\frac{1}{2}} = \cos\left[\frac{(2j + 1)\pi}{2N}\right], \quad 0 \le j \le N - 1, \tag{2.17}$$

and the Lobatto points, defined by

$$X_j = \cos\left[\frac{j\pi}{N}\right], \quad 0 \le j \le N. \tag{2.18}$$

Within each element, the solution, u, and the flux, f, are approximated by Lagrangian interpolants and are represented by truncated expansions of the basis functions as

$$u(X) \approx \tilde{u}(X) = \sum_{i=0}^{N-1} \tilde{u}_{i+\frac{1}{2}}\, h_{i+\frac{1}{2}}(X) \tag{2.19}$$

and

$$f(X) \approx \tilde{f}(X) = \sum_{i=0}^{N} \tilde{f}_i\, l_i(X), \tag{2.20}$$

where $h_{i+1/2}$ and l_i are the basis functions and are chosen to be Lagrange polynomials defined by

$$h_{i+\frac{1}{2}}(X) = \prod_{j=0\ j\neq i}^{N-1} \frac{X - X_{j+\frac{1}{2}}}{X_{i+\frac{1}{2}} - X_{j+\frac{1}{2}}} \tag{2.21}$$

and

$$l_i(X) = \prod_{j=0\ j\neq i}^{N} \frac{X - X_j}{X_i - X_j}. \tag{2.22}$$

The Lagrangian basis functions can be also expressed in terms of Chebyshev polynomials such that

$$l_i(X) = \frac{2}{N} \sum_{n=0}^{N} \frac{1}{\bar{c}_i\, \bar{c}_n}\, T_n(X_j)\, T_n(X), \tag{2.23}$$

where T_n is the Chebyshev polynomial defined by

$$T_n(X) = \cos\left(n.\arccos(X)\right), \tag{2.24}$$

and

$$\bar{c}_k = \begin{cases} 2, & k = 0, N, \\ \\ 1, & k \neq 0, N. \end{cases} \qquad (2.25)$$

The collocation points for the solution, $\tilde{u}$, are chosen to be the Chebyshev-Gauss quadrature points, Equation 2.17, which are found by determining the roots of T_{N+1}. The reason for choosing this particular collocation points for the Lagrangian interpolant $\tilde{u}$ is that

$$\|u - \tilde{u}\| \ll \left(\frac{1}{N}\right)^k, \quad N \to \infty, \quad \text{for all } k, \qquad (2.26)$$

(for $u \in C^\infty$, where C^p is the space of functions that are continuous and have continuous derivatives up to order p) as can be demonstrated by Sturm-Liouville theory (14). The roots of the derivative of T_{N+1}, Equation 2.18, are chosen as the collocation points for the flux, $\tilde{f}$. Substituting the approximations, Equation 2.19 and Equation 2.20, into the governing equation, Equation 2.16, we get

$$\sum_{i=0}^{N-1} \frac{\mathrm{d}\tilde{u}_{i+\frac{1}{2}}}{\mathrm{d}t} h_{i+\frac{1}{2}}(X) + \frac{1}{x_X} \cdot \frac{\partial}{\partial X}\left[\sum_{i=0}^{N} \tilde{f}_i l_i(X)\right] = R(X), \qquad (2.27)$$

where $R(X)$ is the residual due to the approximation. The method of weighted residuals (MWR) is used to minimize the approximation residual. In the MWR, the intent is to set the inner product of the residual with respect to some test functions, $\psi_j(X)$, to zero

$$\int_0^1 R(X)\,\psi_j(X)\,\mathrm{d}X = 0. \qquad (2.28)$$

In other words, MWR is a method that minimizes the error of approximation by fitting trial functions into the PDE. There are two widely used types of spectral methods: spectral Galerkin methods and spectral collocation methods. In the spectral Galerkin methods, the test functions are the same as the trial functions, while in spectral collocation methods, which is used in the DSEM, the test functions are the shifted Dirac delta functions located at so-called collocation points (15). There are two types of spectral formulations: modal and nodal formulations. In the modal formulation, the unknowns are the expansion coefficients, while in the nodal formulation, which is used in the DSEM, the unknowns are the solution values at the collocation points. The more natural choice for collocation methods is the nodal formulation, and it always leads to an uncoupled system since the test functions are the Dirac delta functions (15). The Dirac delta function is defined by

$$
\delta(x) = \begin{cases} +\infty, & x = 0 \\ 0, & x \neq 0 \end{cases} \tag{2.29}
$$

and is constrained to satisfy

$$
\int_{-\infty}^{\infty} \delta(x)\, \mathrm{d}x = 1. \tag{2.30}
$$

Here, we choose the Gauss points, Equation 2.17, as the collocation points. Therefore, the test functions are defined by

$$
\psi_j(X) = \delta(X - X_{j+\frac{1}{2}}). \tag{2.31}
$$

Substituting the test function, Equation 2.31, into the MWR, Equation 2.28, we get

$$\int_0^1 R(X)\,\delta(X - X_{j+\frac{1}{2}})\,\mathrm{d}X = 0. \tag{2.32}$$

Applying the definition of the Dirac delta function, Equation 2.29 and Equation 2.30, we have

$$R(X_{j+\frac{1}{2}}) = 0. \tag{2.33}$$

This means that choosing Dirac delta functions at the collocation points as our test functions is mathematically equivalent to forcing the residual to be zero at the collocation points, which are the Gauss points here. In other words, in spectral collocation methods, we require that the PDE be satisfied at the collocation points (16).

Substituting the residual, Equation 2.27, and the test functions, Equation 2.31, into the MWR, Equation 2.28, we get

$$\int_0^1 \left[\sum_{i=0}^{N-1} \frac{\mathrm{d}\tilde{u}_{i+\frac{1}{2}}}{\mathrm{d}t}\, h_{i+\frac{1}{2}}(X)\,\delta(X - X_{j+\frac{1}{2}}) + \frac{1}{x_X}\frac{\partial \tilde{f}(X)}{\partial X}\delta(X - X_{j+\frac{1}{2}}) \right]\mathrm{d}X = 0. \tag{2.34}$$

Applying the definition of the Dirac delta function, Equation 2.34 becomes

$$\sum_{i=0}^{N-1} \frac{\mathrm{d}\tilde{u}_{i+\frac{1}{2}}}{\mathrm{d}t}\, h_{i+\frac{1}{2}}(X_{j+\frac{1}{2}}) + \frac{1}{x_X}\frac{\partial \tilde{f}(X_{j+\frac{1}{2}})}{\partial X} = 0. \tag{2.35}$$

Recalling that $h_{i+1/2}(X_{j+1/2}) = \delta_{ij}$ (Here, δ_{ij} is the Kronecker delta), Equation 2.35 reduces to the collocation approximation

$$\frac{\mathrm{d}\tilde{u}_{j+\frac{1}{2}}}{\mathrm{d}t} + \frac{1}{x_X} \frac{\partial F(X_{j+\frac{1}{2}})}{\partial X} = 0. \tag{2.36}$$

Equation 2.36 is the discretized version of the governing equation, Equation 2.16, and is used to calculate the solution unknowns at the Gauss points, $\tilde{u}_{j+\frac{1}{2}}$.

The first step to evaluate the fluxes is to interpolate the solution values from the Gauss grid to the Lobatto grid using

$$\tilde{u}_j = \sum_{i=0}^{N-1} \tilde{u}_{i+\frac{1}{2}} \, h_{i+\frac{1}{2}}(X_j), \quad 0 \leq j \leq N. \tag{2.37}$$

Then, the fluxes can be calculated directly on the Lobatto grid using their functional relation to the solution. On the element interface the values of the fluxes are most likely different from two sides. The mortar method is used to patch the fluxes on the interfaces and achieve C_0 continuity of the flux. The patching of the fluxes are described in details in section 3.1.5 of (10).

Next, the spatial derivative of the flux is calculated using

$$\frac{\partial F(X_{j+\frac{1}{2}})}{\partial X} = \sum_{i=0}^{N-1} F(X_i) \, \frac{\partial l_i(X_{j+\frac{1}{2}})}{\partial X}. \tag{2.38}$$

The governing partial differential equation (PDE) is now reduced to an ordinary differential equation (ODE). The ODE may be integrated in time using any desired time-stepping scheme. In DSEM, a low-storage fourth-order Runge-Kutta scheme is employed (Refer to section 3.2 of (10)).

2.2.2 3D Euler Equations

Assume the 3D Euler equations in conservative form,

$$\vec{q}_t + \vec{f}_x + \vec{g}_y + \vec{h}_z = 0, \tag{2.39}$$

where $\vec{q}$ is the solution vector, and $\vec{f}_x$, $\vec{g}_y$, and $\vec{h}_z$, are the flux vectors in the x-,y-, and z-directions, respectively. Under the isoparametric transformation of the elements to a unit cube, the governing equations become

$$\vec{Q}_t + \vec{F}_X + \vec{G}_Y + \vec{H}_Z = 0, \tag{2.40}$$

where

$$\vec{Q} = J\vec{q}, \tag{2.41}$$

and

$$\begin{cases} \vec{F} = X_x \vec{f} + X_y \vec{g} + X_z \vec{h} \\ \vec{G} = Y_x \vec{f} + Y_y \vec{g} + Y_z \vec{h} \\ \vec{H} = Z_x \vec{f} + Z_y \vec{g} + Z_z \vec{h} \end{cases} \cdot \tag{2.42}$$

In Equation 2.41, J is the Jacobian of the transformation and is defined by

$$J = x_X(y_Y z_Z - y_Z z_Y) - x_Y(y_X z_Z - y_Z z_X) + x_Z(y_X z_Y - y_Y z_X). \tag{2.43}$$

In 3D, the staggered grid is the tensor product of the 1D grid described in the previous section. The solution values are determined on the Gauss-Gauss-Gauss (GGG) points,

$$(X_{i+1/2}, Y_{j+1/2}, Z_{k+1/2}), \quad i, j, k = 0, 1, \ldots, N - 1, \tag{2.44}$$

which is the tensor product of the 1D grid defined by Equation 2.17. Assuming the approximation order is the same in every direction, the solution at any point within the element is approximated by the interpolant on the GGG points and is defined by

$$\vec{Q}(X, Y, Z) = \sum_{l=0}^{N-1}\sum_{m=0}^{N-1}\sum_{n=0}^{N-1} \vec{Q}_{l+\frac{1}{2},m+\frac{1}{2},n+\frac{1}{2}}\, h_{l+\frac{1}{2}}(X)\, h_{m+\frac{1}{2}}(Y)\, h_{n+\frac{1}{2}}(Z)\,, \tag{2.45}$$

where $\vec{Q}_{l+1/2,m+1/2,n+1/2}$ is the solution values on the GGG points, and the Lagrange interpolants are defined by Equation 2.21. The fluxes, $\vec{F}$, $\vec{G}$, and $\vec{H}$, are evaluated at the Lobatto-Gauss-Gauss (LGG) points,

$$(X_i, Y_{j+1/2}, Z_{k+1/2}), \quad i = 0, 1, \ldots, N, \quad j, k = 0, 1, \ldots, N - 1, \tag{2.46}$$

Gauss-Lobatto-Gauss (GLG) points,

$$(X_{i+1/2}, Y_j, Z_{k+1/2}), \quad j = 0, 1, \ldots, N \quad , i, k = 0, 1, \ldots, N-1, \tag{2.47}$$

and Gauss-Gauss-Lobatto (GGL) points,

$$(X_{i+1/2}, Y_{j+1/2}, Z_k), \quad k = 0, 1, \ldots, N, \quad i, j = 0, 1, \ldots, N-1. \tag{2.48}$$

The GGG points are usually called the Gauss grid, and the LGG, GLG, and GGL points form the Lobatto grid.

The procedure in 3D is similar to that of the 1D version described in the previous section. First, the solution values, $\vec{Q}$, are interpolated from the Gauss grid to the Lobatto grid in every dimension using the same interpolation as given in Equation 2.45. For example, the solution is interpolated to the LGG grid in the X-direction by

$$\vec{Q}(X_i, Y_{j+\frac{1}{2}}, Z_{k+\frac{1}{2}}) = \sum_{l=0}^{N-1} \sum_{m=0}^{N-1} \sum_{n=0}^{N-1} \vec{Q}_{l+\frac{1}{2}, m+\frac{1}{2}, n+\frac{1}{2}} \, h_{l+\frac{1}{2}}(X_i) \, h_{m+\frac{1}{2}}(Y_{j+\frac{1}{2}}) \, h_{n+\frac{1}{2}}(Z_{k+\frac{1}{2}}). \tag{2.49}$$

Recalling the property of the Lagrange polynomial, $h_{i+1/2}(X_{j+1/2}) = \delta_{ij}$ (Here, δ_{ij} is the Kronecker delta), Equation 2.49 reduces to a 1D operation,

$$\vec{Q}(X_i, Y_{j+\frac{1}{2}}, Z_{k+\frac{1}{2}}) = \sum_{l=0}^{N-1} \vec{Q}_{l+\frac{1}{2}, j+\frac{1}{2}, k+\frac{1}{2}} \, h_{l+\frac{1}{2}}(X_i). \tag{2.50}$$

The solution is similarly interpolated in the Y- and Z-directions by

$$\vec{Q}(X_{i+\frac{1}{2}}, Y_j, Z_{k+\frac{1}{2}}) = \sum_{m=0}^{N-1} \vec{Q}_{i+\frac{1}{2}, m+\frac{1}{2}, k+\frac{1}{2}} \; h_{m+\frac{1}{2}}(X_j). \tag{2.51}$$

and

$$\vec{Q}(X_{i+\frac{1}{2}}, Y_{j+\frac{1}{2}}, Z_k) = \sum_{n=0}^{N-1} \vec{Q}_{i+\frac{1}{2}, j+\frac{1}{2}, n+\frac{1}{2}} \; h_{n+\frac{1}{2}}(X_k). \tag{2.52}$$

The next step is to calculate the flux values on the Lobatto grid using their functional relation to the solution. Again, the mortar method is used to patch the fluxes from neighboring elements. Then, the mapped fluxes are constructed according to Equation 2.42 on the Lobatto grid.

Once the fluxes are constructed on the Lobbato grid, the spatial discretization of the fluxes can be made using the interpolants,

$$\vec{F}(X, Y, Z) = \sum_{l=0}^{N} \sum_{m=0}^{N-1} \sum_{n=0}^{N-1} \vec{F}_{l, m+\frac{1}{2}, n+\frac{1}{2}} \; l_l(X) \; h_{m+\frac{1}{2}}(Y) \; h_{n+\frac{1}{2}}(Z), \tag{2.53}$$

$$\vec{G}(X, Y, Z) = \sum_{l=0}^{N-1} \sum_{m=0}^{N} \sum_{n=0}^{N-1} \vec{G}_{l+\frac{1}{2}, m, n+\frac{1}{2}} \; h_{l+\frac{1}{2}}(X) \; l_m(Y) \; h_{n+\frac{1}{2}}(Z), \tag{2.54}$$

$$\vec{H}(X, Y, Z) = \sum_{l=0}^{N-1} \sum_{m=0}^{N-1} \sum_{n=0}^{N} \vec{H}_{l+\frac{1}{2}, m+\frac{1}{2}, n} \; h_{l+\frac{1}{2}}(X) \; h_{m+\frac{1}{2}}(Y) \; l_n(Z). \tag{2.55}$$

The spatial derivatives of the fluxes (Equation 2.53, Equation 2.54, and Equation 2.55), reduce to 1D operations due to the properties of the Lagrange polynomials (similar to the reduction of the solution interpolations to 1D operations) and follow the 1D approach (Equation 2.38),

$$\frac{\partial}{\partial X}\overrightarrow{F}(X_{i+\frac{1}{2}}, Y_{j+\frac{1}{2}}, Z_{k+\frac{1}{2}}) = \sum_{l=0}^{N} \overrightarrow{F}_{l,j+\frac{1}{2},k+\frac{1}{2}} \frac{\partial l_l(X_{i+\frac{1}{2}})}{\partial X}, \tag{2.56}$$

$$\frac{\partial}{\partial Y}\overrightarrow{G}(X_{i+\frac{1}{2}}, Y_{j+\frac{1}{2}}, Z_{k+\frac{1}{2}}) = \sum_{m=0}^{N} \overrightarrow{G}_{i+\frac{1}{2},m,k+\frac{1}{2}} \frac{\partial l_m(Y_{j+\frac{1}{2}})}{\partial Y}, \tag{2.57}$$

$$\frac{\partial}{\partial Z}\overrightarrow{H}(X_{i+\frac{1}{2}}, Y_{j+\frac{1}{2}}, Z_{k+\frac{1}{2}}) = \sum_{n=0}^{N} \overrightarrow{H}_{i+\frac{1}{2},j+\frac{1}{2},n} \frac{\partial l_n(Z_{k+\frac{1}{2}})}{\partial Z}. \tag{2.58}$$

The governing equations, Equation 2.40, can now be written in the discrete form,

$$\overrightarrow{Q}_t\big|_{i+\frac{1}{2},j+\frac{1}{2},k+\frac{1}{2}} + \left[\overrightarrow{F}_X + \overrightarrow{G}_Y + \overrightarrow{H}_Z\right]_{i+\frac{1}{2},j+\frac{1}{2},k+\frac{1}{2}} = 0, \tag{2.59}$$

which should be integrated in time.

2.2.3 3D Navier-Stokes Equations

The governing equations are the 3D compressible Navier-Stokes equations in conservative form,

$$\overrightarrow{q}_t + \overrightarrow{f}^a_x + \overrightarrow{g}^a_y + \overrightarrow{h}^a_z = \frac{1}{Re_f}\left(\overrightarrow{f}^v_x + \overrightarrow{g}^v_y + \overrightarrow{h}^v_z\right), \tag{2.60}$$

where superscripts a and v indicate advective and viscous fluxes, respectively. The calculation of the advective fluxes are similar to the procedure described earlier for the fluxes in the Euler equations.

To calculate the viscous fluxes, the spatial derivatives of the velocity components and temperature need to be constructed. In order to obtain a unique gradient of those variables, the interpolant of the solution on the Lobatto grid needs to be continuous at interfaces of the elements. This is achieved by using a Dirichlet type of patching (Refer to section 3.1.5 of (10)). Once the Lobatto interpolants are patched, their spatial derivatives are calculated the same manner as the flux derivatives are calculated for the Euler equations, i.e., Equation 2.56, Equation 2.57, and Equation 2.58.

CHAPTER 3

NEAR-WALL RESOLUTION REQUIREMENTS FOR DIRECT

NUMERICAL SIMULATION OF TURBULENT FLOWS

The material presented in this chapter is published as (17):
Ghiasi, Z., Li, D., Komperda, J., and Mashayek, F.: Near-Wall Resolution Requirement
for Direct Numerical Simulation of Turbulent Flow Using Multidomain Chebyshev Grid.
International Journal of Heat and Mass Transfer, 126, Part B: 746 760, 2018.
The coauthors, Dongru Li and Jonathan Komperda, helped me by reviewing the manuscript
and providing their feedback. My advisor and coauthor, Farzad Mashayek, supervised the
work presented in this chapter.

Direct numerical simulation (DNS) of turbulent flow in a 3D periodic channel is performed

to study the effect of the wall-normal spatial resolution near the wall on the calculations of

turbulence statistics using multidomain Chebyshev grids. The DSEM is employed to calculate

the first- and second-order statistics of the flow near the wall. The effect of the spectral approx-

imation order on the resolution requirement is also studied by considering three approximation

orders of $P = 2$, 5, and 7. The Reynolds number based on the bulk density, bulk velocity,

and channel half-height is $Re = 3{,}266$, which corresponds to a friction Reynolds number of

$Re_\tau \approx 204$ based on the wall friction velocity and the channel half-height.

3.1 Introduction

The accuracy of the predictions of turbulence statistics near the wall in DNS of turbulent

flows depends strongly on the grid resolution near the wall, especially in the wall-normal di-

rection. In DNS of near-wall turbulence, the resolution near the wall should be sufficient to

capture the behavior of the boundary layer in all three regions of the inner layer: the viscous (laminar) sublayer, the buffer layer, and the log-law (fully turbulent) region. It has been shown that an under-resolved grid in one or more directions negatively affects the prediction of the mean properties as well as higher-order statistics of the flow (18). Since the grid spacing criteria should be independent of the Reynolds number, the spatial spacing is usually calculated based on the non-dimensional wall unit, y^+ (See Appendix B for the definitions of non-dimensional wall variables). Previous grids used for DNS of wall-bounded turbulent flows usually satisfy two general conditions: (i) The nearest grid point to the wall is located below $y^+ = 1$, and (ii) there are at least 10 grid points within $y^+ = 10$ (hereinafter, called y_{10}^+). For most grids, these conditions can be satisfied by placing the first point below $y^+ = 1$ and gradually increasing the grid spacing (using a geometric progression for example) as moving away from the wall. However, in numerical schemes that use a Chebyshev distribution of grid points, satisfying the second condition would result in a minuscule grid spacing at the wall (usually, orders of magnitude smaller than $y^+ = 1$) due to the high non-uniformity of point distribution. Some types of spectral and spectral element methods are examples of the schemes that use Chebyshev grids, which have been increasingly used by researchers recently (19; 20; 21).

For example, in the DSEM, the Gauss quadrature points in the mapped space are placed in each direction using a symmetric Chebyshev distribution of the form

$$X_{i+\frac{1}{2}} = \frac{1}{2}\left[1 - \cos\left(\frac{i+\frac{1}{2}}{P+1}\,\pi\right)\right], \quad i = 0, \ldots, P, \tag{3.1}$$

over the interval of $[0, 1]$, where P is the spectral approximation order. For an approximation order of $P = 9$, such element has 10 Gauss quadrature points with the distribution shown in Figure 1. Note that the first point is located at $X_{1/2} = 6.16 \times 10^{-3}$. If the near-wall elements are distributed normal to the wall such that the first point off the wall is located at $y^+ = 1$, there would be only 2 points inside y_{10}^+. Even by placing the first point at $y^+ = 0.1$, there would be only 6 points within y_{10}^+. On the other hand, if the elements near the wall are placed such that the second condition is satisfied, i.e., there are 10 Gauss points within y_{10}^+, the first point near the wall would be located at $y^+ = 0.0616$. In this case, the extremely small grid size, which occurs both on the wall side and on the other end of the first element, severely restricts the time step size and makes the simulation computationally expensive if the numerical stability is conditional on the time step size. Therefore, for such schemes, it is challenging to determine the sufficient near-wall resolution, while minimizing the restriction of the time step size. To the best knowledge of the authors, this challenge has not been tackled so far.

The periodic channel flow is a well-studied benchmark for wall-bounded turbulent flows and is used as the test case here. In this chapter, a series of DNS of periodic turbulent channel flow are conducted using DSEM to study the requirement of the grid resolution normal to the wall for accurate prediction of turbulent statistics using multidomain Chebyshev grids (22). The effect of the spectral approximation order on the spatial resolution requirement is also studied by testing three different orders. The flow is simulated using nine grids (three grids with different resolutions for each approximation order) with different resolutions and approximation orders,

and their mean flow statistics, velocity fluctuations, and Reynolds shear stresses are compared.
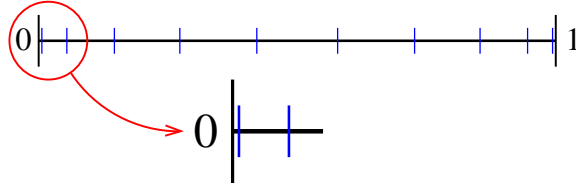
Figure 1. Distribution of Gauss quadrature points (blue ticks) in a Chebyshev grid of order $P = 9$.

3.1.1   Previous DNS of Channel Flow

The DNS of turbulent flow in a periodic channel has been intensively studied. Kim *et al.* (23) conducted DNS of an incompressible, turbulent channel flow using a spectral method. The simulations were performed at a friction Reynolds number of $Re_\tau = u_\tau \delta / \nu = 180$, where u_τ is the wall friction velocity, δ is the channel half-height, and ν is the fluid's kinematic viscosity. Their scheme featured a fully spectral method with Fourier series in the homogeneous directions, i.e., streamwise and spanwise directions, and a Chebychev polynomial expansion in the normal direction. The grid that they used had 12 points inside y_{10}^+, and the nearest grid point to the wall was located at $y^+ = 0.05$. Rai and Moin (24) presented a finite-difference (FD) solution to the incompressible fully developed turbulent channel flow at a friction Reynolds number of $Re_\tau = 180$ and provided a comparison between the results obtained using FD and spectral

methods. They used a geometric progression for the distribution of near-wall grid points normal to the wall. Lyons *et al.* (25) presented results from a DNS of fully developed incompressible turbulent flow in a channel. They also used Fourier series expansions in the periodic directions and Chebyshev polynomial expansions in the normal direction. The friction Reynolds number was $Re_\tau = 130$, and the nearest grid point to the wall was located at $y^+ = 0.18$. Crawford (26) employed a spectral element method and conducted a grid resolution study for an incompressible turbulent flow in a periodic channel at a friction Reynolds number of $Re_\tau \approx 207$. The grid that was concluded to be adequate to resolve the turbulent statistics had its first point near the wall at $y^+ = 0.29$. Moser *et al.* (27), as the continuation of the work of Kim *et al.* (23), used the same code later and reported detailed statistical data from DNS of incompressible fully developed turbulent channel flow at three friction Reynolds numbers of $Re_\tau = 180$, 395, and 590. In all three cases, they had 13 or more grid points within y_{10}^+. del Alamo and Jimenez (28) performed DNS of turbulent channel flow at Reynolds numbers of $Re_\tau = 180$ and 550 using the same numerical method as (23). Their focus was on the size and location of large scales of motion in the channel flow. Morinishi *et al.* (29) performed DNS of turbulent channel flows using an algorithm based on the Fourier Galerkin method in the periodic directions and the B-spline collocation method in the wall-normal direction. They considered both incompressible and compressible (Mach number of 1.5) cases at a Reynolds number of $Re_f = 3,000$ based on the bulk density, bulk velocity, and channel half-height. They used a hyperbolic-tangent function for the distribution of the wall-normal collocation points, and the nearest point to the wall was located at $y^+ = 0.045$ and ~ 0.35 for their incompressible and compressible cases,

respectively. Lee and Moser (30) performed DNS of incompressible channel flow at different Reynolds numbers ranging from $Re_\tau = 180$ to 5,186. They used a Fourier-Galerkin method in the periodic directions and a B-spline collocation method in the wall-normal direction. The grid they used for the highest Reynolds number had 15 points within y_{10}^+. The first points for the lowest and the highest Reynolds number cases were located at $y^+ = 0.074$ and $y^+ = 0.498$, respectively. A summary of the above-mentioned studies along with more details of their computational domains and grids are included in Table I.

Grötzbach (31) deduced three criteria for the prediction of grids for DNS of turbulent flow. Their second criterion, concerning the near-wall resolution, states that, for turbulent flows with a Prandtl number below unity, at least three grid points must be placed inside the viscous sublayer ($y^+ < 5$). Later, Moin and Mahesh (32) provided a review of DNS of turbulent flows. They pointed out that spectral schemes require less spatial resolution than other schemes; A second-order central difference scheme needs nearly double the spatial resolution (in each dimension) to reach the same level of accuracy as a DNS using a spectral method.

In the following section, the problem setup for the periodic channel flow and the grid generation procedures are discussed. Then, the results of the simulations and discussions are presented; first, it is shown that the statistics of interest are not affected by the compressibility, and the methodology is able to reproduce previous DNS results. Then, the mean velocity, temperature, and density profiles, as well as mean flow variables, are compared for different cases. Furthermore, the second-order statistics including the velocity fluctuations and Reynolds shear

TABLE I

PREVIOUS DNS STUDIES OF THE PERIODIC TURBULENT CHANNEL FLOW. THE
LENGTHS ARE SCALED BY THE CHANNEL HALF-HEIGHT (δ). THE DOMAIN SIZES
AND THE NUMBER OF GRID POINTS ARE PROVIDED IN THE ORDER: X, Y, Z. IN
CASE OF MULTIPLE REYNOLDS NUMBERS, THE GRID POINTS USED FOR THE
LOWEST REYNOLDS NUMBER IS PRESENTED.

Reference	Re_τ	Domain size	Grid points
Kim *et al.* (23)	180	$4\pi \times 2 \times 2\pi$	$192 \times 129 \times 160$
Rai and Moin (24)	180	$4\pi \times 2 \times 2\pi$	$64 \times 65 \times 64$
Lyons *et al.* (25)	$125 \sim 135$	$12.67 \times 2 \times 6.33$	$128 \times 65 \times 128$
Crawford (26)	≈ 207	$5.61 \times 2 \times 2$	$64 \times 120 \times 100$
Moser *et al.* (27)	180, 395, 590	$4\pi \times 2 \times 4\pi/3$	$128 \times 129 \times 128$
del Alamo and Jimenez (28)	180, 550	$12\pi \times 2 \times 4\pi$	$754 \times 76 \times 502$
Morinishi *et al.* (29)	$150 \sim 218$	$4\pi \times 2 \times 4\pi/3$	$128 \times 129 \times 128$
Lee and Moser (30)	182, 544, 1,000, 5,186	$8\pi \times 2 \times 3\pi$	$128 \times 192 \times 96$

stresses are presented and discussed for all cases. Next, the cases are compared based on their computational costs. Finally, conclusions are drawn.

3.2   Periodic Turbulent Channel Flow Simulations

In this work, DSEM is employed to conduct a series of DNS of a 3D, turbulent, periodic channel flow to investigate the near-wall grid resolution requirement. First- and second-order statistics of the flow are used to evaluate the accuracy of the calculations. Three different spectral approximation orders of $P = 2$, 5, and 7 are considered to also study the effect of the approximation order on the resolution requirement.

3.2.1   Computational Domain

A schematic of the computational domain is illustrated in Figure 2. The domain is periodic in the streamwise (x) and spanwise (z) directions. Stationary, isothermal walls with the wall

temperature of $T_w = 1$ are placed at the boundaries of the normal (y) direction. The isothermal wall boundary condition is applied using a weak formulation. In this method, which was introduced by Jacobs *et al.* (33), a slightly manipulated version of an Osher solver (34) is used to compute the boundary fluxes. The boundary condition implementation falls into the category of *Weak-Riemann-A1* described in Mengaldo *et al.* (35). The lengths of the domain are $L_x = 5.61$, $L_y = 2$, and $L_z = 2$ in the streamwise, normal, and spanwise directions, respectively. All lengths are scaled by the channel half-height, $\delta = L_y/2$. The lengths in wall units are $L_x^+ \approx 1170$ and $L_y^+ = L_z^+ \approx 420$. The dimensions are the same as those used in Crawford (26) and are chosen such that the domain encompasses the largest eddy of the flow. This configuration of the domain allows the comparison with previous work.
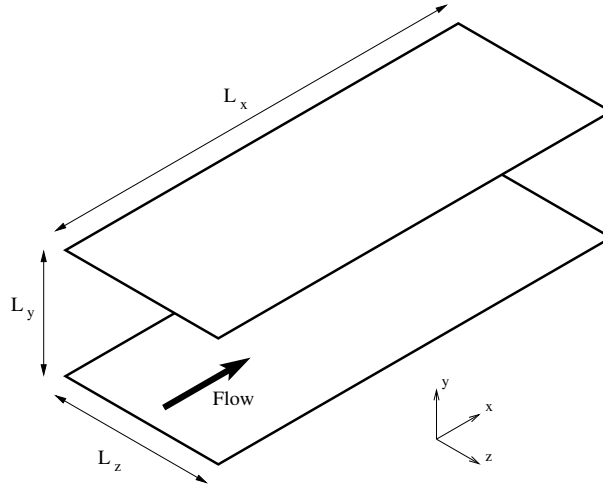
Figure 2. Schematic of the computational domain.

3.2.2 Flow Conditions

The bulk velocity $(\overline{U})$, the bulk density $(\overline{\rho})$, the channel half-height (δ), and the wall temperature (T_w) are chosen as the reference velocity, density, length, and temperature, respectively. All simulations in this work are performed at a reference Reynolds number of $Re_f = 3{,}266$ based on the reference velocity, length, and density. This Reynolds number corresponds to a friction Reynolds number of $Re_\tau \approx 204$ (The exact value of the friction Reynolds number ranges between 204.0 and 208.8 for different cases). The reference Mach number based on the reference velocity and temperature is $M_f = 0.4$. The reference Prandtl number is fixed at $Pr_f = 0.72$, and the heat capacity ratio is assumed to have a constant value of $\gamma = 1.4$.

In a physical channel flow, the flow is maintained by a negative pressure gradient in the streamwise direction $(\mathrm{d}p/\mathrm{d}x)$. Here, a dynamically adjusted force term is applied to maintain a constant mass flow rate. The same forcing algorithm as Lenormand *et al.* (36) is employed in the present work.

3.2.3 Initialization and Transition to Turbulence

The streamwise velocity is initialized with a laminar parabolic profile with a mean value of $\overline{U}_0 = 1$, with the addition of a uniformly distributed random disturbance, as

$$u(y) = -6\left[\left(\frac{y}{2}\right)^2 - \left(\frac{y}{2}\right)\right](1 + \epsilon). \tag{3.2}$$

In Equation 3.2, ϵ is a random disturbance uniformly distributed between 0 and 0.1, which is introduced to expedite the transition to turbulence. The initial spanwise and normal velocities are zero. The temperature is initialized with a laminar Poiseuille profile (See Appendix C) as

$$T(y) = T_w + \frac{3(\gamma - 1)}{4} Pr_f M_f \left[1 - (y - 1)^4\right].$$

(3.3)

The initial density is constant at $\rho_0 = 1$. The initial pressure is calculated through the equation of state.

The preliminary simulations of our base case with $P = 7$ revealed that the initial disturbance that is introduced in Equation 3.2 gradually decays after the simulation runs for a few flow-through times at the base Reynolds number of $Re_f = 3{,}266$, and the transition to turbulence is not achieved. The flow-through time is defined as $t_{ft} = L_x/\overline{U}$. Neither raising the magnitude of the initial disturbance (ϵ) nor a temporary 100% increase in the Reynolds number helped to maintain the disturbance. Increasing the Reynolds number further is not desirable due to the computational cost. As an alternative solution, the flow is initially simulated at a much lower resolution, i.e., using an approximation order of $P = 2$ instead of $P = 7$. The hypothesis is that the truncation error, which is introduced by the deficiency of the spatial resolution, is sufficiently large to provide the required disturbance for a transition to turbulence (10). As the flow undergoes the transition to turbulence, the grid resolution is enhanced by gradually increasing the approximation order ($P = 2$, $P = 3$, $P = 5$, $P = 7$). The flow is simulated at each phase for $3 \sim 4$ flow-through times to ensure a smooth transition. Then, the simulation

is continued at the desired approximation order $(P = 7)$ until a statistically stationary state is reached. The skin friction coefficient, which is defined by

$$c_f = \frac{\tau_w^*}{\frac{1}{2} \, \rho^* \, \overline{U}^{*2}} = \frac{\nu \, \frac{\partial u}{\partial y}|_w}{\frac{1}{2} \, Re_f \, \overline{U}^2} \qquad (3.4)$$

is used to detect the statistically stationary state condition. In Equation 3.4, τ_w^* is the wall shear stress. The value of c_f during the transition is shown in Figure 3. It is observed that during the first two flow-through times of the simulation, c_f remains at the laminar value of $c_f = 6/Re_f = 1.84 \times 10^{-3}$. Then, the value increases rapidly, which indicates the transition of the flow regime from laminar to turbulent. Finally, at $t_{ft} \approx 25$, the value of the skin friction coefficient levels off at a time-averaged constant value, which denotes the statistically stationary flow. In order to keep the computational cost low, this approach is carried out once. Then, the solution of the fully developed turbulent flow is spectrally interpolated to the other grids that are used for different cases considered in this work.

3.2.4   Grid Resolution

In this work, nine grids with different near-wall resolutions and spectral approximation orders are examined. The flow statistics obtained from all grids are compared. It is worth mentioning that the DSEM allows for two levels of control over the grid resolution: (i) h-refinement, in which the number of elements is adjusted, and (ii) p-refinement, in which the elements remain unchanged, and the order of approximation inside each element is changed. In this work, three spectral approximation orders of $P = 2$, 5, and 7 are considered to study the effect of the
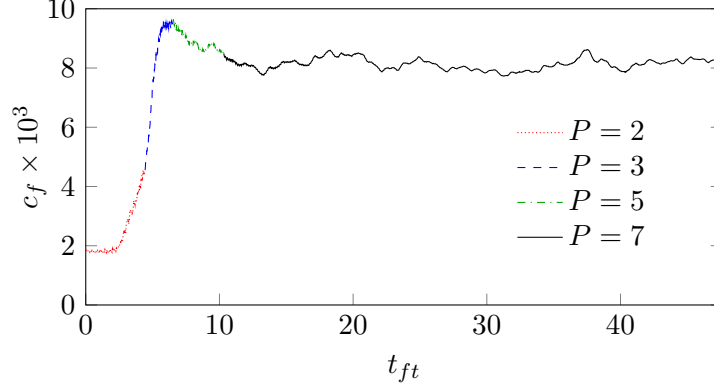
Figure 3. Changes of the skin friction coefficient (c_f) in time (scaled with the flow-through time) during the initial phases of the simulation.

approximation order on the near-wall resolution requirement. For each approximation order, three grids with different near-wall resolutions are generated using h-refinement. The highest resolution grids are in accordance with the second recommended condition for the near-wall resolution and have 11 points within y_{10}^{+}. While, the moderate and low resolution grids have 8 and 5 grid points inside y_{10}^{+}, respectively. In all cases, the elements are uniformly distributed in the periodic directions (x and z). The number of elements in the periodic directions are determined such that the number of grid points are the same for all cases in those directions. The details of all grids are included in Table II. Each case is named based on the grid used for that case as P-Q, where P is the approximation order, and Q is the number of grid points within y_{10}^{+}. The resolution of the base grid (case 7-11) is obtained from the resolution study of Ghiasi *et al.* (22). They showed that this resolution is sufficient for the accurate computation of the first- and second-order statistics of the flow. The resolutions of cases 2-11 and 5-11 in the

normal direction are determined such that they have about the same number of grid points as case 7-11 in that direction. In the normal direction (y) the elements are distributed following a hyperbolic-tangent function of the form

$$\frac{y_n}{L_y} = \frac{1}{2}\left(1 - \frac{\tanh\left[\lambda(\frac{1}{2} - \frac{n}{N_y})\right]}{\tanh\left[\lambda/2\right]}\right), \quad 0 < n < N_y\,, \tag{3.5}$$

where y_n is the y-position of the interfaces of the elements, N_y is the number of elements in the y-direction, and λ is a tunable coefficient that adjusts the compactness of the elements near the wall. The number of elements in the normal direction and the value of λ are determined for each case based on two criteria: (i) The compactness of the elements near the wall is adjusted to achieve the desired number of grid points within y_{10}^+ for each case; (ii) Since here we are interested in the near-wall resolution only, the resolution of the grids at the center of the channel is maintained for all cases. The values of λ for all grids are given in Table II. The distribution of the elements in the normal direction for all nine cases are depicted in Figure 4. Note that only the elements are shown in this figure.

As mentioned earlier, the resolution near the wall should be sufficient to capture the behavior of the boundary layer in all three regions of the inner layer. The locations of solution (Gauss) points near the wall, superimposed on the plot of the friction velocity based on the law of the wall, are shown in Figure 5 for all presented cases in order to visualize the position of the grid points with respect to the regions of the inner layer of the boundary layer. In this figure, only the points up to $y^+ \approx 50$ are shown. It is seen that high resolution cases 2-11, 5-11, and

7-11 have 7, 7, and 6 grid points, respectively, inside the laminar sublayer $(y^+ < 5)$, while the low resolution cases 2-5, 5-5, and 7-5 have only 2, 3, and 3 points within the same region, respectively.

Case: 2-5 2-8 2-11   5-5 5-8 5-11   7-5 7-8 7-11
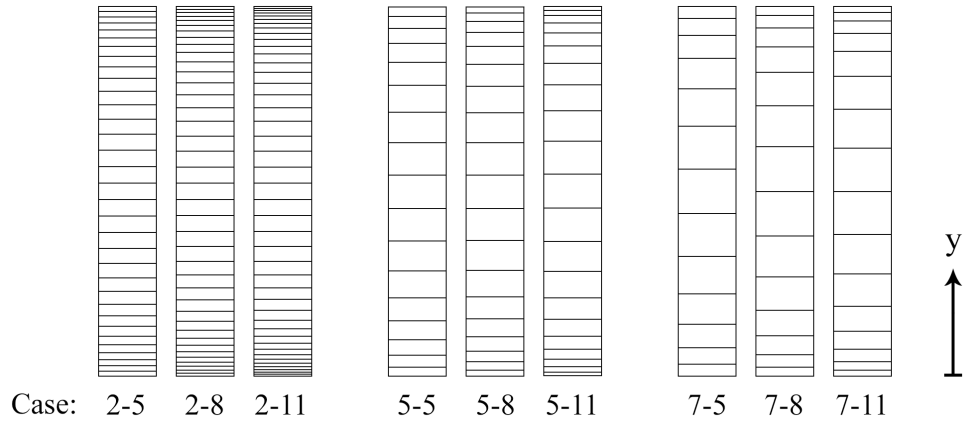
Figure 4. Distribution of elements in the wall-normal direction.

3.3   Results and Discussions

In this section, the results from the DNS of the periodic channel flow are presented to verify the reliability of the method and to study the near-wall resolution requirements for turbulent flows at two different approximation orders.
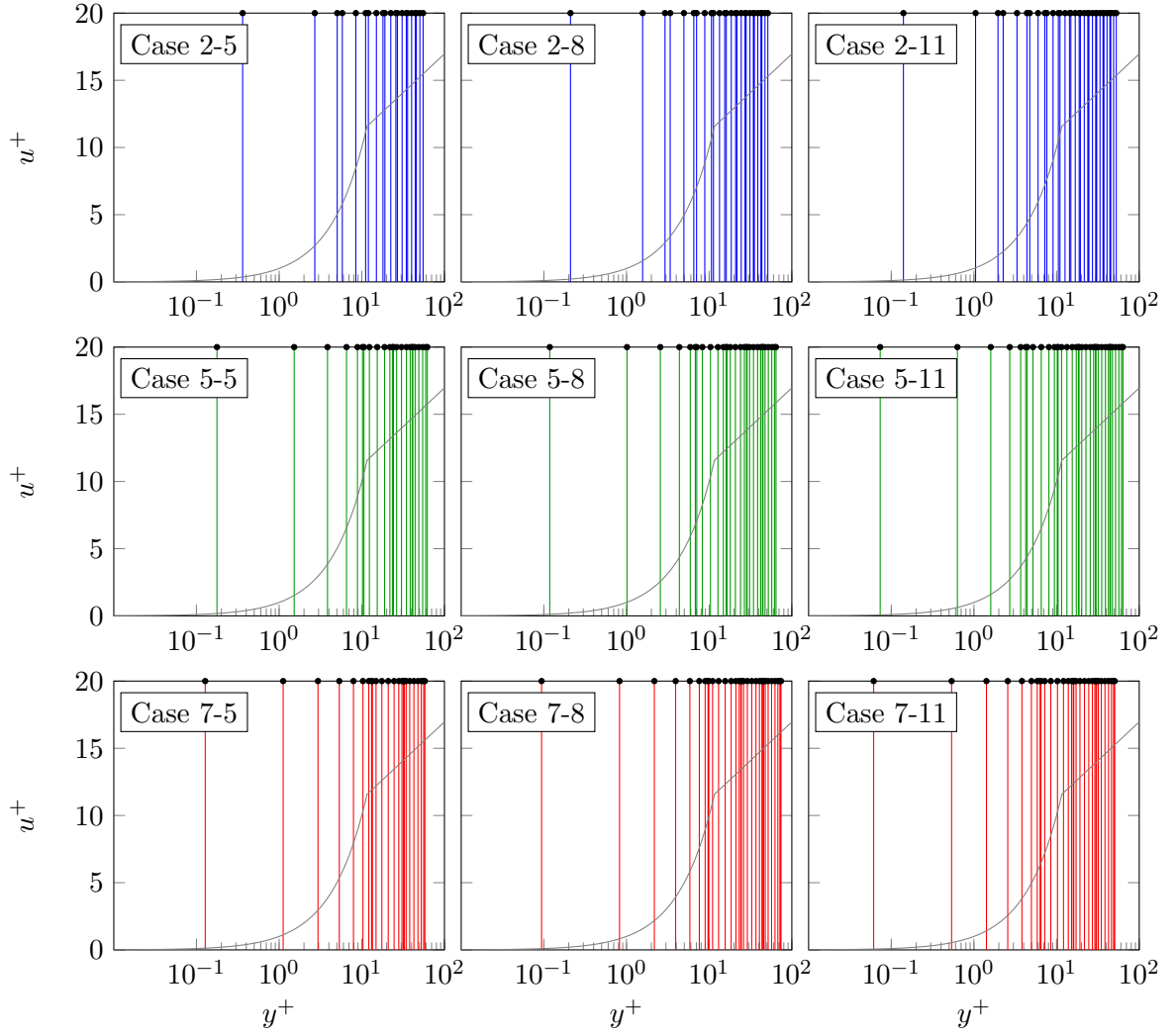
Figure 5. Location of grid points normal to the wall (vertical lines) up to $y^+ \approx 50$ for all presented cases. The friction velocity profile based on the law of the wall (gray curve) is superimposed on the plots.

TABLE II

DETAILS OF THE GRIDS USED FOR THE NINE RESOLUTION STUDY CASES. Y_{MIN}^{+} IS THE WALL-NORMAL LOCATION OF THE NEAREST GRID POINT TO THE WALL, AND λ IS THE COMPACTNESS COEFFICIENT USED IN Equation 3.5. NUMBER OF ELEMENTS AND GRID POINTS APPEAR IN THE ORDER: X, Y, Z.

P	Case	Number of elements	Number of grid points	Total grid points	y_{min}^{+}	Points in y_{10}^{+}	λ	Linestyle
	2-5	$48 \times 33 \times 37$	$144 \times 99 \times 111$	1,582,416	0.37	5	2.55	
2	2-8	$48 \times 39 \times 37$	$144 \times 117 \times 111$	1,870,128	0.21	8	3.14	
	2-11	$48 \times 43 \times 37$	$144 \times 129 \times 111$	2,061,936	0.14	11	3.58	
	5-5	$24 \times 17 \times 19$	$144 \times 102 \times 114$	1,674,432	0.17	5	2.68	
5	5-8	$24 \times 19 \times 19$	$144 \times 114 \times 114$	1,871,424	0.12	8	3.15	
	5-11	$24 \times 21 \times 19$	$144 \times 126 \times 114$	2,068,416	0.072	11	3.70	
	7-5	$18 \times 13 \times 14$	$144 \times 104 \times 112$	1,677,312	0.13	5	2.80	
7	7-8	$18 \times 14 \times 14$	$144 \times 112 \times 112$	1,806,336	0.093	8	3.18	
	7-11	$18 \times 16 \times 14$	$144 \times 128 \times 112$	2,064,384	0.061	11	3.60	

3.3.1 Validation

To validate the adequacy of the size of the computational domain, examples of two-point correlations of the velocity fluctuations for case 7-11 are shown in Figure 6 for two periodic directions, i.e. streamwise and spanwise directions. The samples are taken from two different wall-normal locations of $y/\delta = 0.031$ and 0.824, which translate to wall units of $y^{+} \approx 6$ and 175, respectively, to confirm that the decorrelation is achieved both near the wall and at the core of the channel. The two-point correlation of the velocity fluctuation in i-direction is defined as

$$R_{ii}(r) = \frac{\langle u_i'(x)\, u_i'(x+r) \rangle}{\langle u_i'(x)^2 \rangle},$$

(3.6)

where x is the location of the probe, and r is the separation. Throughout the chapter, $\langle\rangle$ denotes the ensemble (Reynolds) average, and $\{\}$ is the Favre average defined as $\{f\} = \langle\rho f\rangle/\langle\rho\rangle$. Also, the single prime, $'$, and double prime, $''$, refer to the turbulent fluctuations with respect to the ensemble and Favre averages, respectively. The correlations are plotted for the largest separation, which is half the domain size in each periodic direction. The figure shows that at the largest separation, the values of the two-point correlations fall off within the range of $R_{ii} < 5\%$ for all components of the velocity, at both distances from the wall, and at both periodic directions. With this, we conclude that the values of velocity are independent at the largest separation, and the computational box is sufficiently large to encompass the largest eddy of the flow.

In order to ensure that the statistics of interest are not affected by the compressibility, a low Mach number case at $M_f = 0.1$ is also simulated using the grid of case 7-5. The average streamwise velocity profiles are compared for the base Mach number of $M_f = 0.4$ (case 7-5) and the low Mach number case in Figure 7 (a). For each point of the plot, samples are taken from vertical planes parallel to the walls at every time step. The average of all samples is calculated. Then, due to the symmetry of the problem, the average of two sides of the channel centerline is plotted. This procedure is carried out for all presented plots that are drawn versus distance from the wall for half the channel height. In Figure 7(a) the velocity ($u^+ = u/u_\tau$) and the distance from the wall (y^+) are given in wall units. It can be seen that the velocity profiles are similar for the two Mach numbers. The root-mean-square (rms) velocity fluctuation in the i-direction is defined as $u''_{i.rms} = \{u''_i u''_i\}^{1/2}$. The rms velocity fluctuations scaled by the
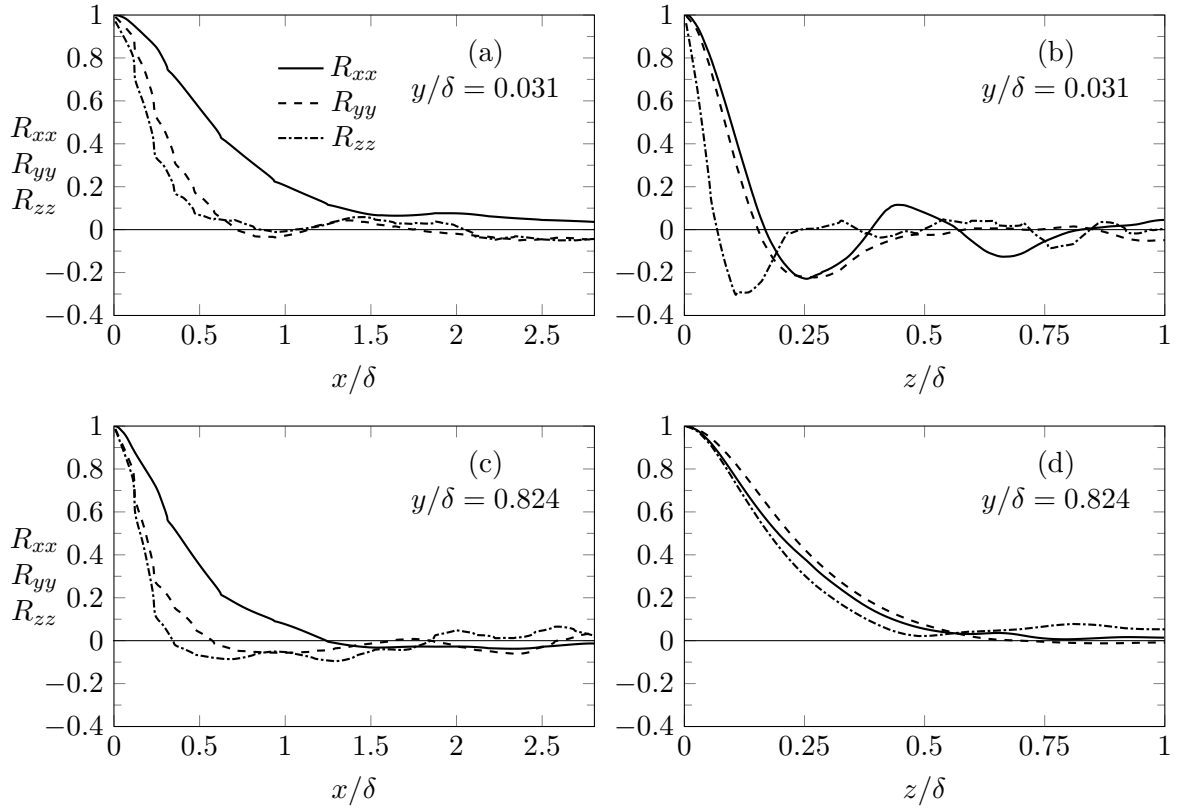
Figure 6. Two-point correlations of the velocity components for case 7-11: (a) near the wall in streamwise direction, (b) near the wall in spanwise direction (c) away from the wall in streamwise direction (d) away from the wall in spanwise direction.
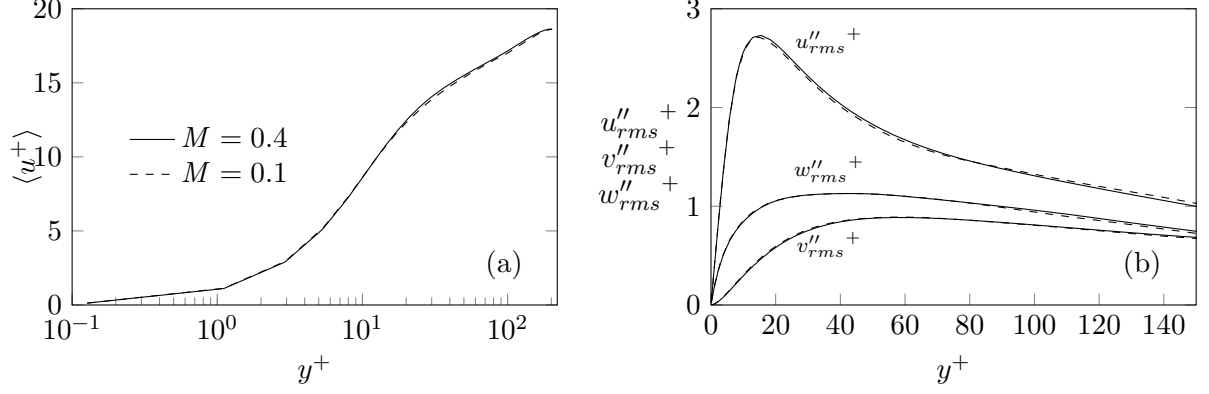
Figure 7. Comparison of (a) the mean streamwise velocity and (b) rms velocity fluctuations for the base Mach number ($M_f = 0.4$) and the low Much number ($M_f = 0.1$), using the grid of case 7-5.

friction velocity, $u''_{i.rms}{}^+ = u''_{i.rms}/u_\tau$, are compared for the two Mach numbers in Figure 7(b) in wall coordinates. It is shown that the rms profiles agree for both Mach numbers. Therefore, it is concluded that the first- and second-order statistics of the flow are not affected by the compressibility for the range of Mach number considered here. This conclusion is consistent with the results of Lenormand *et al.* (36). Wang *et al.* (37) also showed that a channel flow at $M = 0.5$ and $Re = 3,000$ has the same mean streamwise velocity, velocity fluctuations and Reynolds shear stress as the incompressible channel flow of Kim *et al.* (23).

Among the cases considered in this work, case 7-11 is supposed to provide the most accurate results. Firstly, it has the highest resolution near the wall (11 points within y_{10}^+); secondly, it features a higher order spectral approximation of $P = 7$. Therefore, to validate the method, the results from this case are compared with the DNS of Crawford (26). Figure 8(a) and (b)
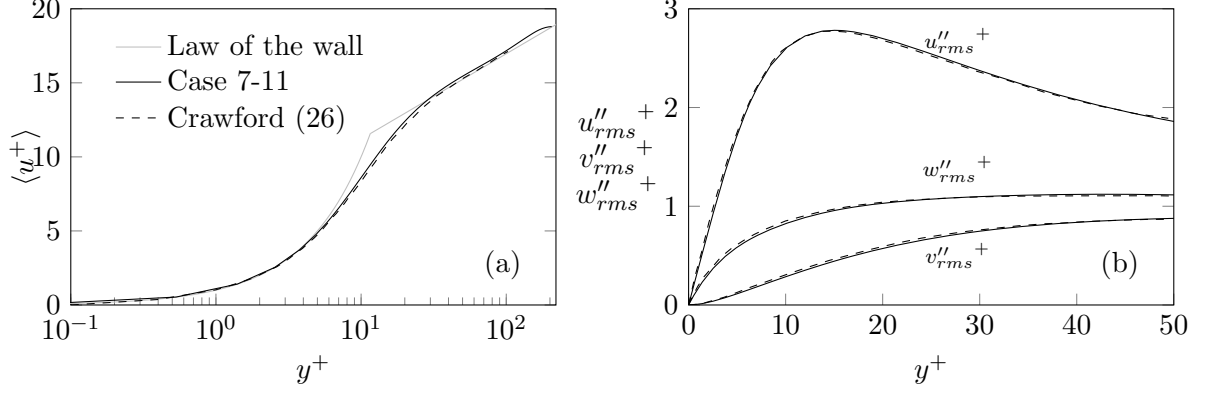
Figure 8. Comparison of (a) mean streamwise velocity and (b) rms velocity fluctuation profiles for case 7-11 and the previous DNS of Crawford (26).

compares the profiles of the streamwise velocity and rms velocity fluctuations of case 7-11 and those of Crawford in wall units, respectively. It is observed that the mean velocity profile follows the law of the wall, and both the mean and fluctuation profiles of case 7-11 agree with the previous work.

The relative temperature scaled by the wall friction temperature (T_τ) is defined as

$$\theta^+ = \frac{T - T_w}{T_\tau}. \tag{3.7}$$

The wall friction temperature is given by

$$T_\tau^* = \frac{q_w^*}{\rho^* c_p^* u_\tau^*} = \frac{k^* \left.\frac{\partial T^*}{\partial y^*}\right|_w}{\rho^* c_p^* u_\tau^*}, \tag{3.8}$$

and in non-dimensional form becomes

$$T_\tau = \frac{\left.\frac{\partial T}{\partial y}\right|_w}{\rho u_\tau Re_f Pr_f}.$$

(3.9)

Figure 9 presents the relative temperature scaled by the Prandtl number for the present low Mach number simulation ($M_f = 0.1$) using the grid of case 7-5. The temperature profile is compared with the incompressible DNS of Kawamura *et al.* (38) and the empirical relation suggested by Kader (See Eq. (9) of (39)). In the immediate vicinity of the wall the molecular conduction dominates the heat transfer, and the temperature linearely changes according to $\langle \theta^+ \rangle = Pr\, y^+$ (39). Figure 9 shows that the mean temperature of the present simulation agrees with both previous simulation and the suggested empirical relation.

Figure 10 illustrates the instantaneous streamwise velocity of case 7-11 on three perpendicular planes. The plane parallel to the walls is located at $y^+ \approx 10$. The wall layer structures are observed on the xz-plane. The so-called streaks are related to bands of low momentum fluid near the wall. The spanwise distance between the streaks are found to be of the order of $d^+ \approx 100$, which is in agreement with previous simulations (36). It can be seen in the xy-plane of Figure 10 that the streaks lift away from the wall at a shallow angle.

3.3.2 Mean Statistics

Each case is simulated for 20 flow-through times to obtain the mean flow statistics. The flow-through time is defined as $t_{ft} = L_x/\overline{U}$. The mean streamwise velocity within the viscous (laminar) sublayer, i.e., $y^+ < 5$, is shown in Figure 11 for all presented cases. Note that the
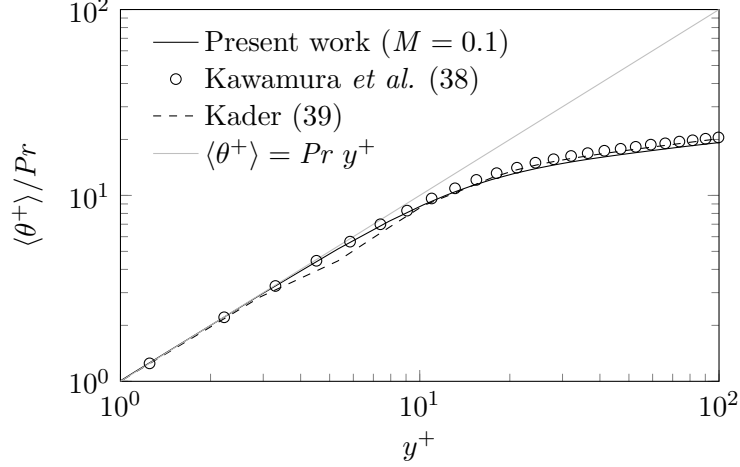
Figure 9. The mean relative temperature scaled by the friction temperature and the Prandtl number for the low Mach number simulation ($M_f = 0.1$) as compared with the DNS of Kawamura *et al.* (38) and the empirical relation of Kader (39).

values are plotted only at the solution (Gauss) points. All cases correctly predict the one-to-one variation of u^+ to y^+ in this region, which is suggested by the law of the wall as $u^+ = y^+$.

The mean streamwise velocity for all nine cases, scaled by the friction velocity, are presented in Figure 12. In all the plots in this work, points are plotted and connected by a straight line. The small difference between the profile of case 2-5 with other cases in Figure 12(a) in the range of $0.4 < y^+ < 3$ is related to this plotting method, and the fact that case 2-5 has the fewest grid points within $y^+ < 3$. The three cases with $P = 5$ (hereinafter, called $P5$ cases), as well as the three cases with $P = 7$ (hereinafter, called $P7$ cases), have the same profiles throughout the half-height of the channel. All nine cases predict the same velocity profiles up to $y^+ = 10$. Above $y^+ = 10$, the profiles of cases with $P = 2$ (hereinafter, called $P2$ cases) are generally
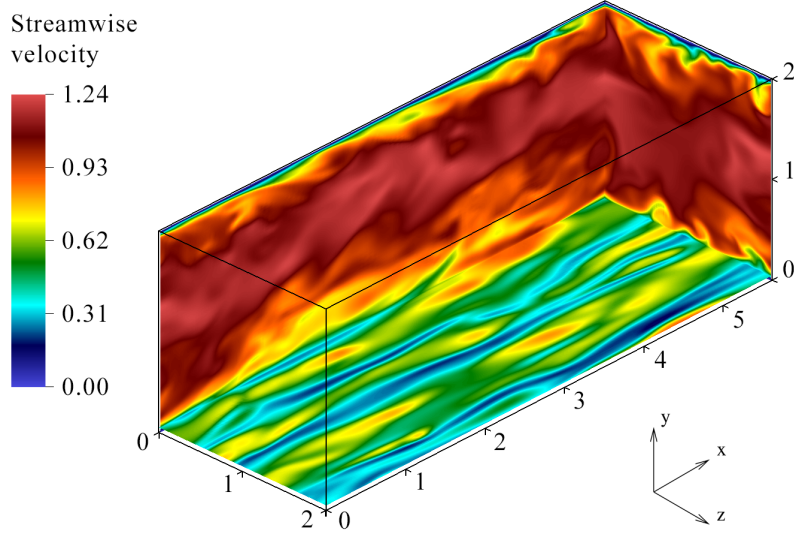
Figure 10. Instantaneous streamwise velocity from case 7-11.

lower than those of $P5$ and $P7$ cases. After a closer look at this region (see Figure 12(b)), it is revealed that the profile of case 2-11 separates from the other $P2$ cases at $y^+ \approx 30$ and matches those of $P5$ and $P7$ cases at $y^+ \approx 140$. The same behavior is observed for the profile of case 2-8, but at different locations: It deviates from that of case 2-5 at $y^+ \approx 100$ and joins those of $P5$ and $P7$ cases at $y^+ \approx 200$. It is concluded that $P2$ cases slightly underpredict the mean streamwise velocity for $y^+ > 10$. This underprediction happens in a shorter range for the cases with higher near-wall resolution.

The profiles of the mean temperature scaled by the wall temperature (T_w) and the mean density scaled by the bulk density for all cases are presented in Figure 13(a) and (b), respectively. The bulk density is calculated by averaging the density over space (whole domain) and time. The
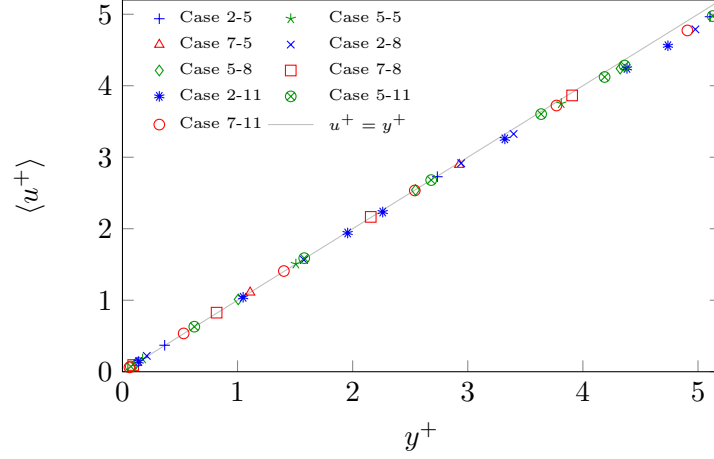
Figure 11. Mean streamwise velocity at solution (Gauss) points, in wall coordinates, within the viscous sublayer for all nine cases.
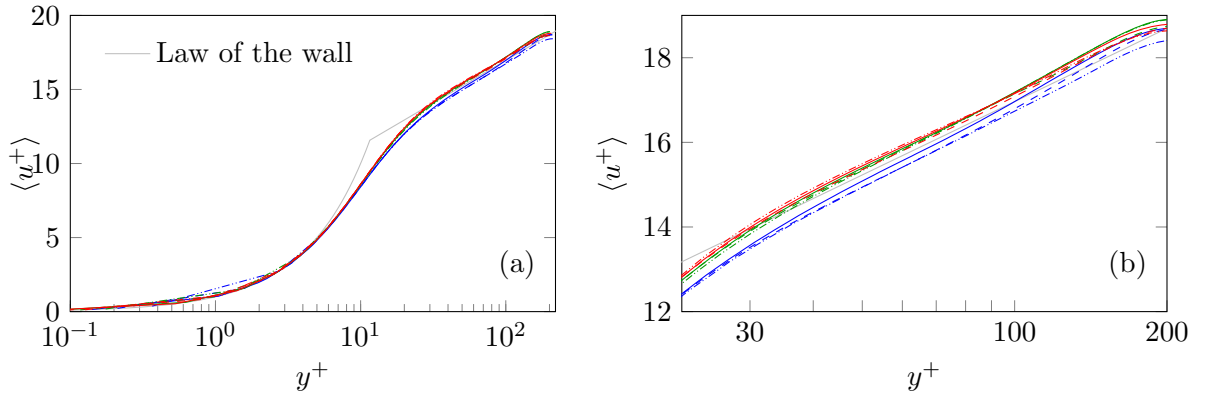
Figure 12. (a) Mean streamwise velocity plotted in wall coordinates for all cases. (b) Same as (a), but magnified at the log-law region. The linestyle for the presented cases are provided in Table II.
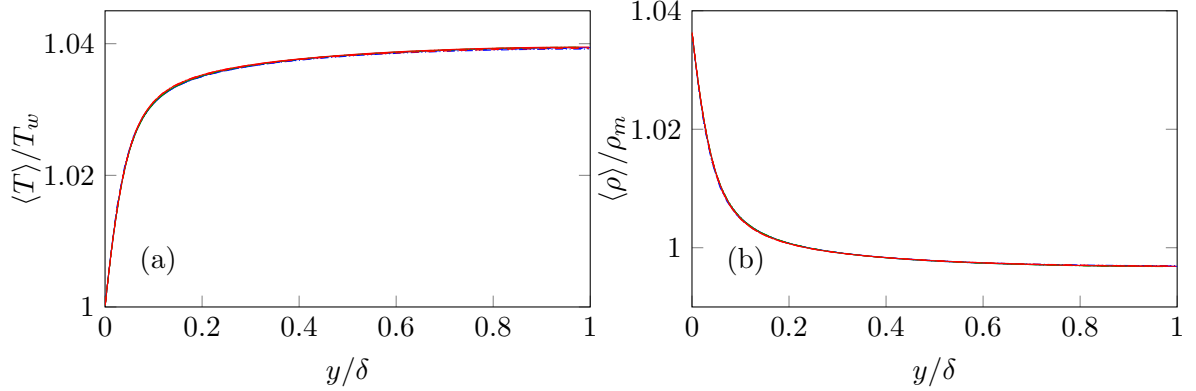
Figure 13. Mean profiles of (a) temperature and (b) density. The linestyles are provided in Table II.

maximum temperature and the minimum density occur on the centerline of the channel, while the walls have the lowest temperature, which is due to the fact that the heat that is caused by dissipation exits the channel through the isothermal walls. It is observed that the temperature and density profiles are not affected by the grid resolution, and the centerline temperature and density have values nearly equal to 1.039 and 0.997, respectively. This demonstrates that temperature and density are not significant variables for studying the effect of the grid resolution in low Mach number flows considered here.

The mean relative temperature scaled by the friction temperature and the Prandtl number (θ^+/Pr) is presented in Figure 14 for all cases. This figure shows that all cases, with the exception of case 2-5, perfectly follow the linear near-wall behavior $(\langle\theta^+\rangle = Pr\,y^+)$. Case 2-5, however, slightly overpredicts the quantity, possibly due to the inaccurate calculation of the slope of the temperature at the wall.
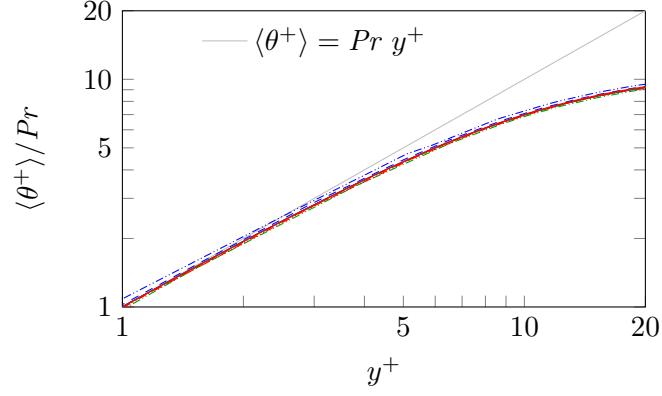
Figure 14. The mean relative temperature scaled by the friction temperature and the Prandtl number near the wall. The linestyle for the presented cases are provided in Table II.

Table III summerizes the mean flow variables for all presented cases. The second column provides the mean centerline velocity, $\langle u_c \rangle$, scaled by the bulk velocity. All centerline velocities are within 2% of the value of 1.156 calculated by Dean's (40) empirical relation, given by

$$\langle u_c \rangle = 1.28 \, Re_h^{-0.0116}, \tag{3.10}$$

where $Re_h = \overline{U}h/\nu$ is the Reynolds number based on the channel height ($h = 2\delta$) and the bulk velocity. Dean also suggested a correlation for the skin friction coefficient of the channel flow as

$$c_f = 0.073 \, Re_h^{-0.25}. \tag{3.11}$$

All skin friction coefficients of presented cases (given in Table III) are within 4% of the value of 8.12×10^{-3} calculated by Dean's relation. Also shown in Table III is the friction Reynolds

number. The friction Reynolds numbers of cases 7-8 and 7-5 do not significantly differ from that of case 7-11 (0.2% and 0.4% differences, respectively). The predicted friction Reynolds number of $P5$ cases are also close to that of case 7-11, with 0.8%, 0.3%, and 0.3% errors, from the lowest to the highest resolution cases, respectively. However, $P2$ cases have higher friction Reynolds numbers, and the difference with that of case 7-11 is 2.3%, 1.7%, and 1.1% for cases 2-5, 2-8, and 2-11, respectively. The value of the friction Reynolds number is calculated by the relation

$$Re_\tau = \sqrt{\frac{Re_f}{\nu} \left\langle \frac{\partial u}{\partial y} \right\rangle \Big|_w} \, , \tag{3.12}$$

where $\langle \partial u/\partial y \rangle|_w$ is the mean slope of velocity evaluated at the wall for each case. An error in the prediction of the friction Reynolds number is directly related to an inaccurate calculation of the behavior of the velocity adjacent to the wall. This shows that $P2$ cases are unable to accurately capture the slope of the velocity at the wall.

3.3.3   Second-Order Statistics

A comprehensive grid resolution study should include the second-order statistics of the flow. It is reported that under-resolved grid in one or more directions damages the prediction of the mean properties of the flow as well as higher-order statistics (18). We do not include the second-order statistics of temperature and density in this discussion since, as seen by previous analysis of their mean values, these variables are not significant for this analysis. The rms of velocity fluctuations over the full height of the channel for case 7-11 are plotted in Figure 15(a). The symmetry of the profiles about the channel centerline indicates the adequacy of the number of samples taken to average the profiles. In order to make sure that a sufficient number of

TABLE III

MEAN FLOW VARIABLES AND THE SIMULATION TIMES REQUIRED BY EACH
CASE (IN FLOW-THROUGH TIME UNIT) TO REACH RMS PROFILE SYMMETRY.

P	Case	$\langle u_c \rangle$	$c_f \times 10^3$	Re_τ	t_{ft}
	2-5	1.166	8.16	208.8	80
2	2-8	1.176	8.07	207.5	145
	2-11	1.170	7.98	206.4	150
	5-5	1.171	7.93	205.7	100
5	5-8	1.164	7.85	204.7	140
	5-11	1.170	7.81	204.1	160
	7-5	1.155	7.87	204.9	120
7	7-8	1.162	7.83	204.4	150
	7-11	1.162	7.80	204.0	160

samples is taken, the simulation is continued until the symmetry of the rms profiles is reached
and the profiles do not change in time. The evolutions of the maxima of the streamwise velocity
fluctuations on both sides of the channel in time (scaled by the flow-through time) are shown
in Figure 15(b) for case 7-11. The plot reveals that 160 flow-through times is needed to reach
the symmetry. The last column of Table III provides the simulation time required by each
case (in flow-through time unit) to reach the symmetry of the rms profiles. It is observed that
cases with lower P generally require less time to achieve the symmetry than their corresponding
cases with higher P with the same near-wall resolution. This could be attributed to the higher
numerical dissipation caused by lower-order discretization of low-P cases compared to high-P
cases. It is also observed that, for each polynomial order, the low resolution cases require
significantly less time to achieve the symmetry than the moderate and high resolution cases.
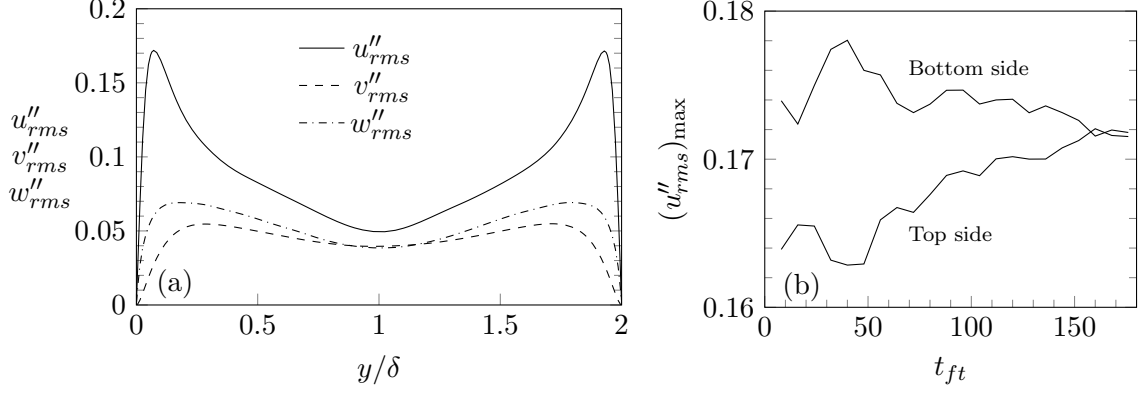
Figure 15. (a) Profiles of rms velocity fluctuations for case 7-11. (b) Evolutions of maxima of streamwise rms velocity fluctuations in time (normalized by flow-through time) on both sides of the channel for case 7-11.

This observation could be attributed to the lower number of samples (in time) for calculation of the rms profiles for the low resolution cases; low resolution cases have smaller number of time steps per flow-through time due to their larger time step sizes.

The rms of streamwise velocity fluctuation in wall units ($u''_{i.rms}{}^+ = u''_{i.rms}/u_\tau$) for all presented cases are shown in Figure 16(a). The rms values are generally lower for $P2$ cases within $8 < y^+ < 70$. Figure 16(b) shows a magnified view of the same plot for $P2$ cases near the peaks as compared with the results from DNS of Crawford (26). All three $P2$ cases significantly underpredict the value of the streamwise velocity fluctuation. The error of the maximum of the quantity is 7%, 5%, and 4% for cases 2-5, 2-8, and 2-11, respectively. Figure 16(c) and (d) are the same as Figure 16(b), but for $P5$ and $P7$ cases, respectively. $P5$ cases are in good agreement with the reference DNS, as shown in Figure 16(c); cases 5-5 and 5-8 slightly under-
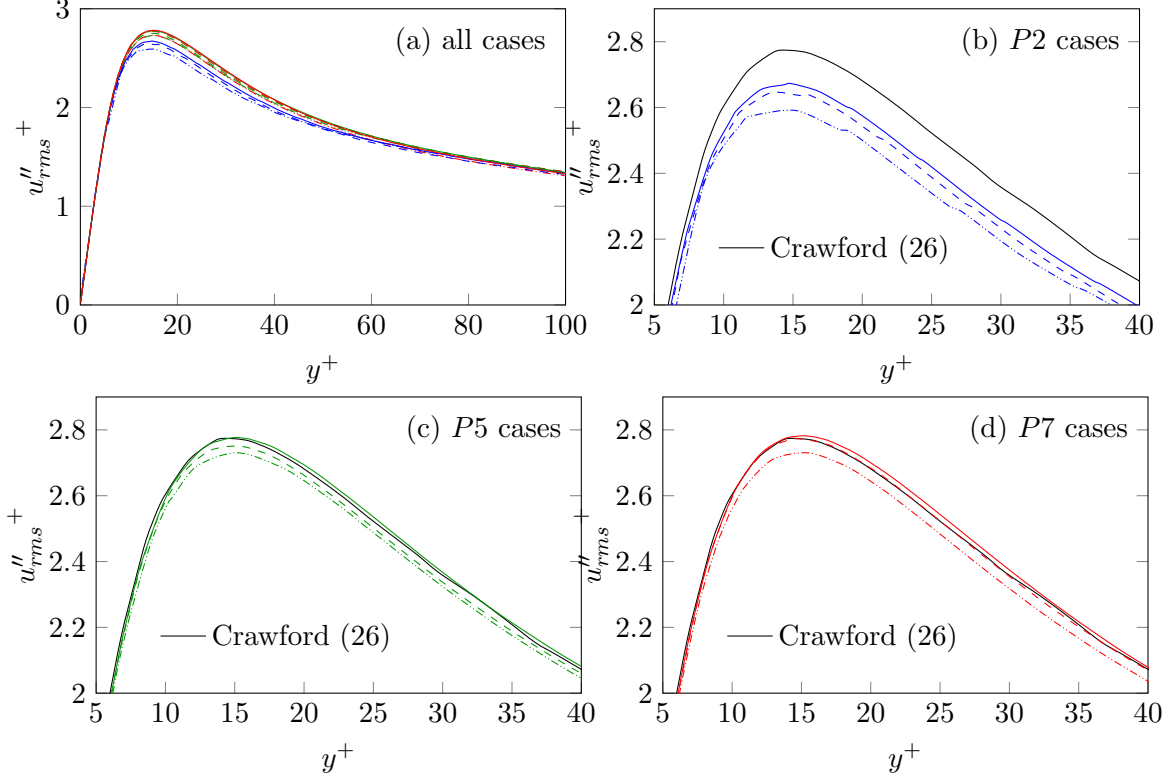
Figure 16. (a) The rms of streamwise velocity fluctuations for all cases. (b)-(d) Same as (a), but magnified near the peaks, as compared with the DNS of Crawford (26) for $P2$, $P5$, and $P7$ cases, respectively. The linestyle for the presented cases are provided in Table II.

predict the quantity (1.5% and 0.8% maximum error, respectively). Among $P7$ cases, only case 7-5 slightly underpredicts the rms of streamwise fluctuations (1.5% maximum error), and both cases 7-8 and 7-11 agree with the previous work. Regardless of the approximation order (P), higher-resolution cases have more accurate predictions of the streamwise fluctuations, and the profiles of the moderate-resolution cases are closer to those of higher-resolution cases than the lower-resolution cases.
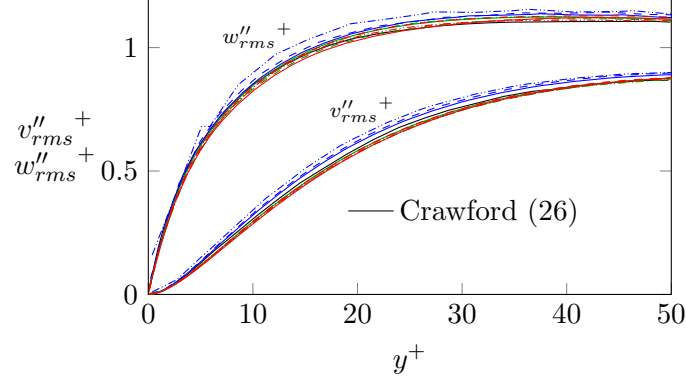
Figure 17. The rms of normal ($v''_{rms}{}^+$) and spanwise ($w''_{rms}{}^+$) velocity fluctuations for all cases, along with DNS of Crawford (26). The linestyle for the presented cases are provided in Table II.

The rms of normal and spanwise velocity fluctuations in wall units for all cases are shown in Figure 17 as compared with the DNS of Crawford (26). The discrepancies of the normal fluctuations ($v''_{rms}{}^+$) are not significant for $P5$ and $P7$ cases. However, $P2$ cases provide slightly higher values. Case 2-5 significantly overpredicts the spanwise velocity fluctuation.

Profiles of rms of velocity fluctuations near the wall scaled by the local streamwise velocity ($u''_{rmsi}/\langle u \rangle$) are shown in Figure 18(a)-(c) for all cases. The values are compared with the results reported by Rai and Moin (24) at a slightly lower friction Reynolds number of $Re_\tau = 180$. All presented cases provide similar profiles outside the viscous sublayer ($y^+ > 5$). Inside the viscous sublayer, however, oscillations appear in some cases. The only cases with completely smooth values adjacent to the wall are cases 5-11 and 7-11. Cases with higher near-wall resolution have smoother values near the wall. $P2$ cases, especially case 2-5, 2-8, and 5-5, show significantly stronger oscillations comparing with $P7$ cases.
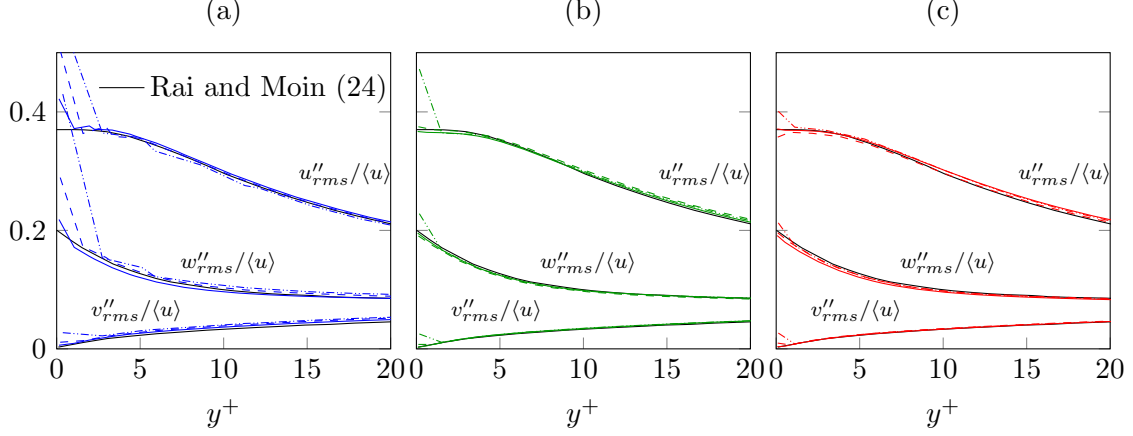
Figure 18. Profiles of rms velocity fluctuations near the wall normalized by the local mean velocity for (a) $P2$ cases, (b) $P5$ cases, and (c) $P7$ cases, compared with results of Rai and Moin (24). The linestyle for the presented cases are provided in Table II.

The Reynolds shear stress profiles, $-\{u''v''\}$, for all presented cases along with that of Crawford (26) are shown in Figure 19 (a). The results from the nine cases are in good agreement with the previous result. The discrepancy between the current work and Crawford's work could be due to the insufficient number of samples in the previous work. Figure 19(b) shows a magnified view of the same plot near the peaks. $P2$ cases calculate a higher peak for the quantity comparing with $P5$ and $P7$ cases. The difference between the peaks of the low and high resolution cases is more evident for $P = 2$ than for higher-P cases.

The mean total shear stress, $\langle \tau_T \rangle$, in a fully developed, compressible, periodic, force-driven channel flow can be theoretically calculated in wall units by the equation (Huang et $al.$ (41)):

$$\langle \tau_T^+ \rangle = \frac{\langle \tau_T \rangle}{\tau_w} = \frac{\langle \mu \rangle}{\mu_w} \frac{\partial \langle u^+ \rangle}{\partial y^+} + \left\langle \frac{\mu'}{\mu_w} \frac{\partial u'^+}{\partial y^+} \right\rangle - \frac{\langle \rho \rangle \{u''v''\}}{\rho_w u_\tau^2} = 1 - \frac{1}{\delta} \int_0^y \frac{\langle \rho \rangle}{\bar{\rho}} \, \mathrm{d}y. \tag{3.13}$$

Applying $\delta = 1$ (δ is the channel half-height) and assuming constant viscosity, which is the case

here, Equation 3.13 is reduced to

$$\frac{\partial \langle u^+ \rangle}{\partial y^+} - \frac{\langle \rho \rangle \{u''v''\}}{\rho_w u_\tau^2} = 1 - \int_0^y \frac{\langle \rho \rangle}{\bar{\rho}} \, \mathrm{d}y. \tag{3.14}$$

Since the flow considered here is at a low Mach number, and the changes of density are small, the

right-hand side of Equation 3.14 fall on a straight line $(1-y)$ for all cases, as shown in Figure 20.

The profiles of the mean total shear stress ($\langle \tau_T^+ \rangle$), i.e., the left-hand side of Equation 3.14, are

shown in Figure 21(a). For a fully developed channel flow in a statistical equilibrium state,

Equation 3.14 should be satisfied, i.e., the mean total shear stress should follow a straight line.

Figure 21(a) validates that this is the case here. A magnified view of the same plot near the

wall is shown in Figure 21(b). Strong oscillations appear in lower resolution cases, especially

case 2-5. The oscillations are stronger for $P2$ cases than $P5$ and $P7$ cases. The deviation of

the higher resolution cases (see cases 5-11 and 7-11) from the straight line is possibly due to

the insufficient number of samples.

From the discussed results, it is observed that the approximation order plays a major role

in the near-wall resolution requirement; $P7$ and $P5$ cases produce more accurate solutions than

$P2$ cases with the same number of grid points. This is due to the exponential convergence of

the solution with the order of approximation, that is inherent in spectral methods (16). Case

7-8 provides nearly the same fidelity as case 7-11, despite featuring only 8 points within y_{10}^+.
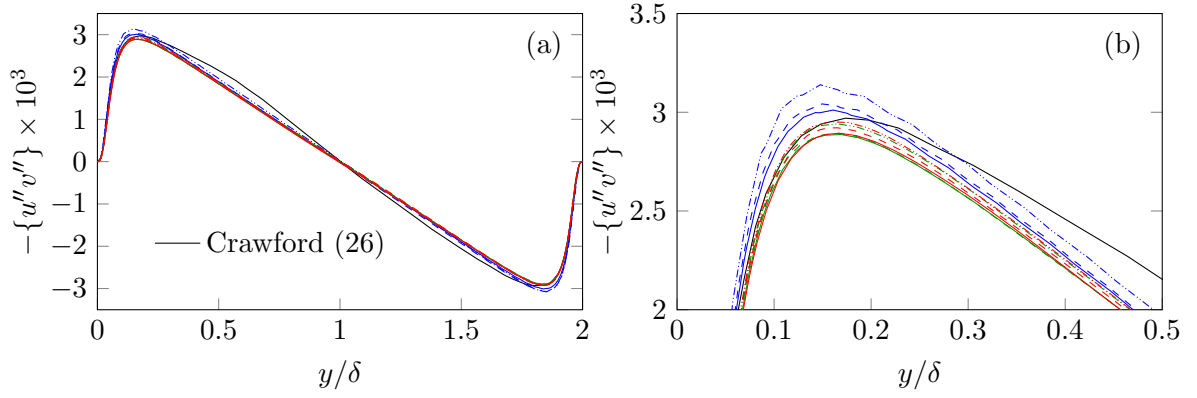
Figure 19. (a) Reynolds shear stress for all presented cases and Crawford (26). (b) Same as (a), but magnified near the peaks. The linestyle for the presented cases are provided in Table II.
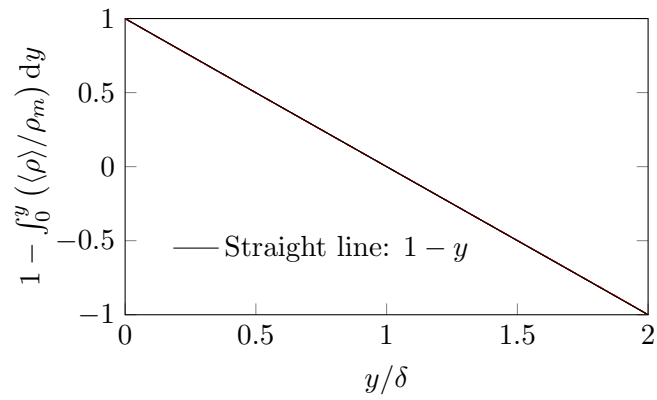
Figure 20. The right-hand side of Eq. (Equation 3.14) for all presented cases as compared with a straight line. The linestyle for the presented cases are provided in Table II.
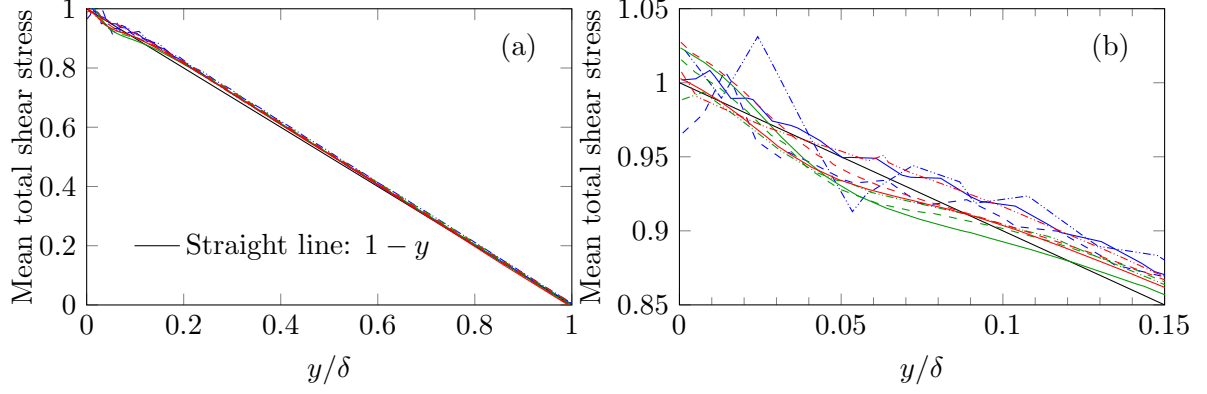
Figure 21. (a) Mean total shear stress, $\partial\langle u^+\rangle/\partial y^+ - \langle\rho\rangle\{u''v''\}/(\rho_w u_\tau^2)$, for all presented cases. (b) Same as (a), but magnified near the wall. The linestyle for the presented cases are provided in Table II.

Even case 7-5 (with only 3 points inside the laminar sublayer, as shown in Figure 5) is more accurate than case 2-11 (with 7 points inside the laminar sublayer).

It is also observed that, up to $y^+ \approx 10$, all cases predict the same mean velocity and almost the same rms of velocity fluctuation. The major differences between the cases are observed in (i) more outer regions of the boundary layer, i.e., $10 < y^+ < 50$, and (ii) the wall friction characteristics of the flow, such as the friction velocity, the non-dimensional wall coordinate (y^+), and the friction Reynolds number. The error in the calculation of the wall friction characteristics results in wrong representation of the variables scaled by the wall units (y^+ and u^+).

3.3.4   Computational Cost

As mentioned earlier, the extremely small grid size near the wall in numerical methods using highly non-uniform grids results in a severe time step size restriction and increases the computational cost of the simulation. The objective here is to determine the sufficient grid resolution to capture the accurate flow statistics while minimizing the computational cost. The computational costs of all considered cases are provided in Table IV. All timing tests are performed on a single processor so that they are not affected by the parallel efficiency of the code. The simulations are conducted using Intel Xeon E5-2670 (2.60 GHz) processors. The minimum grid sizes and the time step sizes of all cases are also included in Table IV. The Kolmogorov time scale of the present problem is $t_\eta \approx 1.7 \times 10^{-2}$ (See Appendix D for the definitions of Kolmogorov scales). The time step sizes of different cases determined by the CFL condition is shown to be in the range of $6.1 \times 10^{-4} < \Delta t < 2.5 \times 10^{-3}$. Therefore, the time step size for the present Reynolds number is not limited by the Kolmogorov time scale.

The sixth column provides the computation time in CPU hours per flow-through time of the simulation. It can be seen that the time step size, and consequently the flow-through hours, are highly affected by the near-wall resolution, such that, for $P = 7$ for example, the cost of the high resolution case is twice that of the low resolution one. The flow-through hours for each case is influenced by two factors: (i) with higher resolution, the minimum grid size is smaller, and the time step size is more restricted, therefore, more steps are needed to complete one flow-through time of simulation; (ii) for grids with higher resolution, there are more solution

points throughout the domain, which need to be updated every time step, and this adds to the computational cost of each time step.

The last column of Table IV provides the CPU hours of the whole simulation for each case. As mentioned before (see Table III), the required number of flow-through times to reach the symmetry of the rms velocity fluctuation profiles are different for different cases. Note that the numbers provided are not the actual simulation times, rather they are CPU hours if the simulations were performed on a single processor. The difference in the computational cost of the low and high resolution cases are more apparent when looking at this quantity. The CPU hours of the high resolution case is more than four times that of the low resolution case for $P = 2$, and more than three times and about 2.5 times for $P = 5$ and $P = 7$, respectively. This is due to the fact that, as discussed before, higher resolution cases require more flow-through times to reach the symmetry of the rms profiles.

The CPU hours per flow-through time of the simulation for all cases are visualized in Figure 22. It is observed that using higher approximation order (P) is generally more computationally expensive for two cases with the same resolution. However, this increase in cost comes with a significant improvement in the accuracy of the calculations. In fact, all $P7$ cases provide higher accuracy than any $P2$ case. Case 7-8 resolves all statistics of interest (as demonstrated before) with a lower computational cost than case 2-11. Therefore, we conclude that case 7-8 is the most efficient case with sufficient resolution to resolve the flow statistics.

TABLE IV

COMPUTATIONAL COSTS IN CPU HOURS ON A SINGLE PROCESSOR. FLOW-THROUGH HOURS IS THE CPU HOURS REQUIRED TO COMPLETE ONE FLOW-THROUGH TIME, WHILE SIMULATION HOURS IS THE CPU HOURS FOR THE WHOLE SIMULATION. Y_{MIN} IS THE NORMAL LOCATION OF THE NEAREST POINT TO THE WALL, AND ΔT IS THE TIME STEP SIZE.

P	Case	y_{min}^+	$y_{min} \times 10^4$	$\Delta t \times 10^4$	Flow-through hours	Simulation hours
	2-5	0.37	17.4	25.5	24.3	2,429
2	2-8	0.21	10.1	18.5	37.4	6,167
	2-11	0.14	6.74	13.9	58.2	9,886
	5-5	0.17	8.50	13.1	31.6	3,796
5	5-8	0.12	5.66	10.3	45.0	7,194
	5-11	0.072	3.53	7.46	68.7	12,368
	7-5	0.13	6.13	9.70	38.1	5,327
7	7-8	0.093	4.51	8.09	49.8	8,474
	7-11	0.061	2.94	6.07	76.2	13,710

3.4   Summary and Conclusions

The near-wall resolution requirement for DNS of turbulent flows using multidomain Chebyshev grids is studied through a series of DNS of turbulent periodic channel flow at a friction Reynolds number of $Re_\tau = 204$. A discontinuous spectral element method is employed, which features non-overlapping elements. Inside each element, the solution is approximated on a grid with a Chebyshev distribution of points. In such a method, due to the strong non-uniformity of the grid point distribution, satisfying the near-wall resolution conditions recommended by previous work (placing at least 10 grid points within y_{10}^+) results in an excessively small time
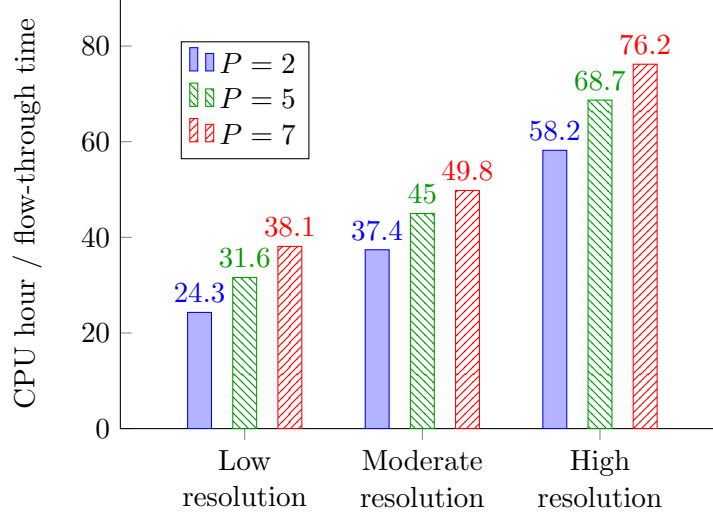
Figure 22. Computational cost for all presented cases in CPU hours per flow-through time of simulation. Low, moderate, and high resolution correspond to 5, 8, and 11 points below y_{10}^+, respectively.

step size, and adds to the computational cost. It is important to determine a resolution that is sufficient to resolve the turbulent statistics while minimizing the computational cost.

Three different approximation orders of $P = 2$, 5, and 7 are considered here to examine the effect of the approximation order on the resolution requirement. For each approximation order, three grids with different near-wall resolutions are tested. The high resolution grids feature 11 grid points inside y_{10}^+, and the moderate and low resolution grids have 8 and 5 points within y_{10}^+, respectively. The same flow is simulated using the nine grids, and first- and second-order statistics of the flow are compared. It is shown that the solution is not affected by the compressibility effects. The results obtained from the case with the highest resolution (case 7-11) agrees with previous work and serves as our base case. The observations are as follows:

1. All cases predict the same normalized mean streamwise velocity inside the laminar sub-layer ($y^+ < 5$), and those profiles agree with the law of the wall ($u^+ = y^+$).

2. All $P7$ and $P5$ cases have the same mean streamwise velocity profiles throughout the channel height. However, $P2$ cases predict lower values for $y^+ > 10$. This underprediction happens in different ranges for different cases, and the range is shorter for higher resolution cases.

3. The calculated friction Reynolds numbers for $P7$ cases are within 0.44% of each other. $P5$ cases also have close predictions of the quantity (0.8% maximum difference with case 7-11). However, $P2$ cases predict higher values (1.1% to 2.3% difference with case 7-11).

4. Cases 5-11, 7-8, and 7-11 predict the same rms of streamwise velocity fluctuations, while cases 5-5, 5-8, and 7-5 slightly underpredict the quantity. $P2$ cases, however, calculate significantly lower streamwise fluctuations. Regardless of the approximation order, lower resolution cases have smaller fluctuations. The difference of the streamwise velocity fluctuation prediction between the lowest and the highest cases is larger for $P = 2$ than other cases.

5. Lower resolution cases, especially with $P = 2$, have oscillations in their velocity fluctuations scaled by the local mean streamwise velocity near the wall.

6. $P2$ cases have higher Reynolds shear stress than other cases. Lower resolution generally results in overprediction of the Reynolds shear stress, and this overprediction is more evident for the lower approximation order.

7. The total shear stress for all cases fall on a straight line, which shows: (i) the total shear stress is not affected by the compressibility, and (ii) a statistical equilibrium state is reached. However, lower resolution cases of $P = 2$ show strong oscillations near the wall.

8. Higher-P cases are generally more computationally expensive than lower-P cases, with the same total grid points. However, they provide significantly more accurate results. Higher resolution cases require more computational time to complete one flow-through time of simulation as well as more number of flow-through times to achieve symmetry of rms profiles. It is concluded that case 7-8 is the most efficient case with the sufficient resolution for accurate calculations of the flow statistics.

It is concluded that the near-wall resolution requirement for accurate prediction of turbulence statistics of the flow strongly depends on the spectral approximation within the elements. Higher approximation order produces more accurate solution than lower approximation order with the same number of grid points within y_{10}^{+}. For the higher approximation order of $P = 7$, the near-wall resolution that places 8 grid points within y_{10}^{+} is sufficient for accurate calculations of the first- and second-order turbulence statistics near the wall. An approximation order of $P = 5$ requires 11 points within the same region for accurate flow statistics. However, for the lower approximation order of $P = 2$, even having 11 grid points within y_{10}^{+} results in slight underprediction of the mean streamwise velocity, significant underprediction of the rms of the streamwise velocity fluctuations, overprediction of the Reynolds shear stress, and oscillations of the total shear stress and velocity fluctuation scaled by the mean streamwise velocity near the wall. It is also observed that the number of grid points within y_{10}^{+} has a stronger effect on

the quality of the solution in cases with lower approximation order than in those with higher approximation order. Note that the conclusions hold true for the low Reynolds number flows, and further investigation is desired for a broader range of Reynolds number.

CHAPTER 4

MODAL EXPLICIT FILTERING FOR LARGE EDDY SIMULATION

The material presented in this chapter is a collaborative work, which is not published yet. It will be submitted to the Journal of Computational Physics as:

Ghiasi, Z., Komperda, J., Li, D., Nicholls, D., and Mashayek, F.: Modal Explicit Filtering for Large Eddy Simulation in Discontinuous Spectral Element Method.

The coauthors, Dongru Li, Jonathan Komperda, and David Nicholls, helped me by reviewing the manuscript and providing their feedback. My advisor and coauthor, Farzad Mashayek, supervised the work presented in this chapter.

Developing a turbulence model that is computationally inexpensive and compatible with the nature of the numerical scheme is a crucial step in expanding the application of spectral element methods for large eddy simulation (LES) in complex geometries. In this work, an element-level modal low-pass explicit filtering procedure, which operates in the spectral space, is implemented in the discontinuous spectral element method (DSEM). The application of the modal filter is studied for LES without a subgrid-scale (SGS) model. The method is tested for a configuration featuring 3D isotropic turbulence, and its performance is compared with a previously used method—a spectral interpolation-based nodal filter. The filtering procedure is also applied to a 3D turbulent channel flow at a friction Reynolds number of $Re_\tau = 544$, and the results are compared with a previous direct numerical simulation (DNS). The effects of both h and P resolutions on the best choice of the filter strength are also studied. An anisotropic version of the modal filter, which damps high-frequency modes in a specific direction, is also introduced and tested for the channel flow.

4.1   Introduction

In large eddy simulation (LES) of turbulent flows, the motions with larger scales are directly
calculated, while the effects of the small-scale motions are modeled (42). The governing equa-
tions of the large-scale motions of the flow are obtained by applying a spatial low-pass filter to
the Navier-Stokes equations (42). The filter divides the flow scales into two parts: resolved and
subfilter-scale (SFS) motions (43). These regions are shown in Figure 23. The most widely used
approach for LES is to consider the coarse computational mesh as the spatial low-pass filter.
This type of filter is called an implicit filter since no explicit filtering operation is applied in the
procedure (42). For the case of the implicit filter, SFS would be equivalent to the scales smaller
than the grid size, the so-called subgrid-scales (SGS); see Figure 23. Even though the implicit
filtering approach takes full advantage of the grid resolution, the shape of the low-pass filter is
not known (43). Another drawback of the implicit filtering approach is that there is no direct
control on the energy spectra in the high-wavenumber motions (42). To address the issues at-
tributed to implicit filtering, explicit filtering is often introduced; a low-pass filter, with a filter
width larger than the grid size, is explicitly applied to the flow variables. The explicit filtering
approach provides a well-defined filter shape at the cost of reducing the effective resolution of
the simulation compared with the grid resolution (42; 44). Since the filter width is larger than
the grid size, the SFS motions are divided into resolved subfilter-scale and unresolved subfilter-
scale motions. The latter is equivalent to the SGS motions. The use of an explicit filter is
practiced in LES studies and is shown to reduce the numerical error (44; 45) as well as aliasing
and SGS modeling errors (44) and improve the accuracy of LES results (43; 44; 46). Gullbrand

and Chow (43) performed LES of turbulent channel flow using a finite difference (FD) code. They showed that using explicit filtering potentially limits the effects of the numerical errors in dynamic Smagorinsky (47) and dynamic reconstruction models and significantly improves the accuracy of the mean velocity and turbulence intensities. In both cases of LES with implicit and explicit filtering, the effects of the motions of the unresolved scales should be taken into account. Those effects, which appear as the SGS stress tensor in the governing equations, are commonly modeled by a SGS model, such as an eddy-viscosity model (48; 49; 47) or a similarity model (50).
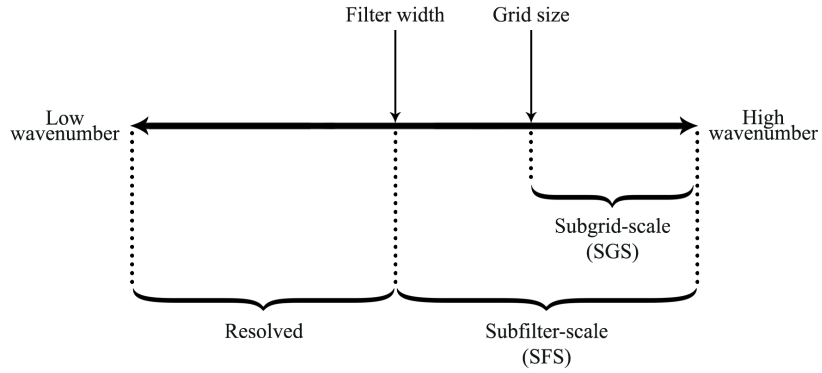
Figure 23. The division of turbulence motions by the filter and the grid based on their wavenumbers.

An alternative approach that is gaining more attention recently is a form of LES known as implicit LES (ILES). In this approach, the dissipation of the numerical scheme is assumed

to mimic the effects of the viscous dissipation of the SGS motions and dampen the turbulent energy. Even though, ILES has shown successful results (51; 52; 53; 54), the damping effects on the resolved scales remain questionable. This method is also not suitable for high-order schemes that introduce minimal or no numerical dissipation. In the absence of sufficient dissipation, the accumulation of the energy at the grid cutoff wavenumber results in numerical errors and could lead to instabilities (42). To alleviate this problem, an explicit low-pass filter can be applied to the solution variables to remove the small-scale components of the solution. In this approach, the explicit filtering serves as a drain for the energy cascade and prevents the instabilities (42). This approach reduces the computational cost as well as implementation complexity compared to methods that use a SGS model. Using an explicit filter without any SGS model has been practiced for LES studies. Bogey and Baily (55) conducted high-order finite difference simulation of compressible jets using an explicit filter without any SGS model. They applied the filter to the density, velocities, and pressure every two time steps, sequentially in x-, $y-$, and z-directions. Mathew *et al.* (56) applied an explicit filter on the solution variables at every time step for LES of compressible channel flows. However, they mention that a finite number of time steps can be taken without applying the filter. Fischer and Mullen (57) applied an explicit interpolation-based nodal filter to stabilize their spectral element method and used it for LES of complex flows (58). Later, Sengupta (59) used the same filtering approach without a SGS model for LES of isotropic turbulence and compared the results with the dynamic Smagorinsky model (49). Sengupta *et al.* (60) used the same procedure for the LES of flow over a backward-facing step.

The benefit of explicit filtering is realized especially in high-order methods such as discontinuous spectral element methods (DSEM). The negligible numerical dissipation in these methods demands a drain for the energy cascade to avoid numerical instabilities in under-resolved simulations. The basis functions in spectral methods form a hierarchical set, i.e., they represent progressively higher spatial frequencies. Therefore, a sharp cutoff of the higher modes in the modal space (a modal filter) represents a low-pass spatial filter of the solution in the nodal space. Boyd (61; 62) applied a modal filter in his spectral method to reduce Gibbs oscillations that are produced by shocks. Levin *et al.* (63) used a two-step modal filter to suppress the instabilities in an eddy resolving spectral element ocean model. Blackburn and Schmidt (64) used a modal filter in their spectral element method as the test filter of the Germano-Lilly (49; 47) dynamic procedure and applied the method for a turbulent channel flow. Bouffanais *et al.* (65) also applied the modal filtering technique in conjunction with the dynamic model in their spectral element method for simulation of a lid-driven cubic cavity flow. Chaudhuri *et al.* (66) applied an adaptive low-pass modal filter to the solution variables to eliminate its high-frequency components and prevent instabilities around the shock.

To the best of our knowledge, the use of a modal filter, with no SGS model, for LES has not been studied in spectral element methods. In this work, the application of a modal filter in DSEM, without any SGS model, is investigated for LES of isotropic and wall-bounded turbulent flows. A low-pass filter is applied to the primitive variables of the Navier-Stokes equations in the modal space. The performance of such an explicit filter is studied for both decaying isotropic turbulence and a turbulent flow in a periodic channel. Since the filters are applied locally within

the elements, the filtering operation is performed on a single processor for each element. This makes the method computationally inexpensive with nearly no impact on the parallelization of the code. Global filters are expensive in spectral element methods (67) due to the necessity for communication between the processors. Since the filtering procedure does not consider any special treatment for the walls, the method can be used for more complex flows.

The remainder of the chapter is organized as follows. In section 4.2, the filtering procedures and formulations are explained. Next, in section 4.3, the modal filtering is tested for a problem exhibiting isotropic decaying turbulence, and its performance is compared with two spectral interpolation-based nodal filters as well as a dynamic Smagorinsly model. The study continues with the application of the modal filter to LES of a periodic turbulent channel flow, in section 4.4. A grid resolution study is performed to ensure grid independence of the method. Furthermore, the ideal choice of the filter strength is investigated by performing simulations using multiple grids with different h and P resolutions. For the channel flow case, an anisotropic version of the modal filter is also introduced and tested. The present methods are also compared in terms of their computational cost. Conclusions are drawn in the last section.

4.2   Filtering Procedures

Two filtering procedures are presented in this work. A filtering procedure in a spectral element method can be constructed using either a modal low-pass filter in the modal space or an interpolant-projection in the nodal space (64). For the case of modal filtering, the solution needs to be transformed from the nodal representation to the modal representation within each element. Then, the modes with the highest frequencies are set to zero. Finally, the modes

are transformed back to the nodal space. For the case of a nodal filter, the solution, which is constructed as a sum of basis functions of order P in each element, is interpolated to a basis function of order P', where $P' < P$. Then, the solution is projected back to the original basis function of order P. Though the two filters introduced here are designed to remove high-frequency motions of the flow, they are different than conventional filters in terms of their operating mechanism to achieve the same goal; they may be considered as projection operators instead. The two filtering approaches are explained in detail in the following sections.

4.2.1 Modal Filter

A solution function in a spectral element method can be expressed in either nodal or modal representation. In the nodal representation, the function is expressed through the values of the function on a set of specific points in space. In the modal representation, the function is expressed through the coefficients of a set of orthogonal expansion functions, or modes. The two representations are mathematically equivalent, but each has their own computational properties (68). A local solution function, $\tilde{u}(X, t)$, inside a 1D element with a polynomial order of P in the mapped space can be expressed at a specific time via its modal expansion as

$$\tilde{u}(X) = \sum_{k=0}^{P} \hat{u}_k \, \psi_k(X), \tag{4.1}$$

where $\psi_k(X)$ are the basis functions, and $\hat{u}_k$ are the expansion coefficients. The basis functions form a hierarchical set, i.e., each successive mode represents motions with higher spatial frequencies. In the modal filtering approach, the solution variables are transformed from the

nodal to the modal representation, and the expansion coefficients that correspond to the highest frequencies are set to zero. The transformation mechanism between the nodal representation, $\tilde{u}(X)$, and the modal representation, $\hat{u}_k$, of the solution is a discrete Chebyshev transform (DChT) and an inverse discrete Chebyshev transform (iDChT) (69) (Refer to Appendix A for detailed explanations). The formulations for DChT and iDChT are given by Equation A.4 and Equation A.5, respectively. Both transformations are implemented in DSEM using the library *Fastest Fourier Transform in the West* (FFTW) (70). More details of the transformations are included in A.

The expansion functions in multiple space dimensions are the tensor-products of the 1D functions, and the filtering procedure in three dimensions is applied using the matrix tensor product properties. Assume $\tilde{u}(X, Y, Z)$ is the solution in the mapped nodal space within a 3D element with a polynomial order of P. The solution function can be expressed via its modal expansion as

$$\tilde{u}(X, Y, Z) = \sum_{k=0}^{P}\sum_{l=0}^{P}\sum_{m=0}^{P} \hat{u}_{klm}\,\psi_k(X)\psi_l(Y)\psi_m(Z), \tag{4.2}$$

where $\hat{u}_{klm}$ are the 3D expansion coefficients, which represent the modes of the function in the 3D space; therefore, we call it the modal matrix. An example of such a 3D matrix is shown in Figure 24(a) for a polynomial order of $P = 8$. Each small cube represents an entry of the modal matrix, i.e., an expansion coefficient. After transforming the solution to the modal space, we can modify the modes as desired, and then return the solution to the nodal space using an iDChT. The component $\hat{u}_{000}$ of the modal matrix represents the bulk value of the function within the element (Figure 24(b)), while components $\hat{u}_{k00}$, $\hat{u}_{0l0}$, and $\hat{u}_{00m}$ represent the modes

purely in the x-, y-, and z-directions, respectively (Figure 24(c)). Consequently, components with combinatory subscript represent the combinatory modes in the 3D space. Also, the components with lower subscript represent the low-frequency modes, and the components with higher subscript represent the high-frequency modes. Therefore, lowering the values of the components with higher subscript is equivalent to damping the high-frequency motions, which is the aim here. For example, if we set all the components $\hat{u}_{klm}$, where $\max\{k, l, m\} = P$, to zero, it is equivalent to removing all the motions with contributions from the highest-frequency modes from at least one direction. There are $3P^2 + 3P + 1$ such components, and they are shown in Figure 24(d) for $P = 8$. Therefore, applying a modal low-pass filter with modal strength N_f means (i) transforming the solution from the nodal to the modal space via DChT, given by Equation A.4, (ii) removing all combinatory modes that have contributions from the N_f highest-frequency spatial modes in any direction, i.e.,

$$\hat{u}_{klm} = 0 \quad \forall \quad \{k, l, m\} \quad \text{where} \quad \max\{k, l, m\} > P - N_f, \tag{4.3}$$

and (iii) transforming the solution back to the nodal space via iDChT, given by Equation A.5. For example, for $N_f = 2$, the entries that are removed, i.e., set to zero, are those shown in Figure 24(e). We call this filtering operation isotropic modal filtering since the higher-frequency modes are removed from all three directions.

Alternatively, setting components $\hat{u}_{klm}$, where for example $k = P$, to zero is equivalent to removing all motions with any contribution from the highest-frequency modes in the x-direction.

There are $(P+1)^2$ such components, and they are shown in Figure 24(f) for $P = 8$. Therefore, applying a modal low-pass filter with strength N_f in the ith direction means (i) transforming the solution from the nodal to the modal space by applying the DChT, given by Equation A.4, (ii) removing all combinatory modes that have contributions from the N_f highest-frequency modes in the i-direction, i.e.,

$$\hat{u}_{klm} = 0 \quad \forall \quad \{k, l, m\} \quad \text{where} \begin{cases} k > P - N_f & (x\text{-direction}) \\ l > P - N_f & (y\text{-direction}) \,, \\ m > P - N_f & (z\text{-direction}) \end{cases} \tag{4.4}$$

for removing the high-frequency modes in the x-, y-, or z-directions, respectively, and (iii) transforming the solution back to the nodal space via the iDChT, given by Equation A.5. We call this filtering operation anisotropic modal filtering since the higher-frequency motions are removed only from specific directions. The anisotropic version of the modal filter is tested for the non-isotropic case, i.e. the turbulent channel flow.

4.2.2 Nodal Filter

The second filtering method is called nodal filtering (65; 67). In the nodal filter, the filtered values of a variable in an element with a polynomial order of P are obtained by interpolating the variable to a grid with a lower polynomial order of $P' < P$, then projecting the solution back onto the original grid with the polynomial order of P (65). The nodal filter is also called an interpolant-projection filter (64; 59) or interpolation-based filter (57; 71). The nodal filtering
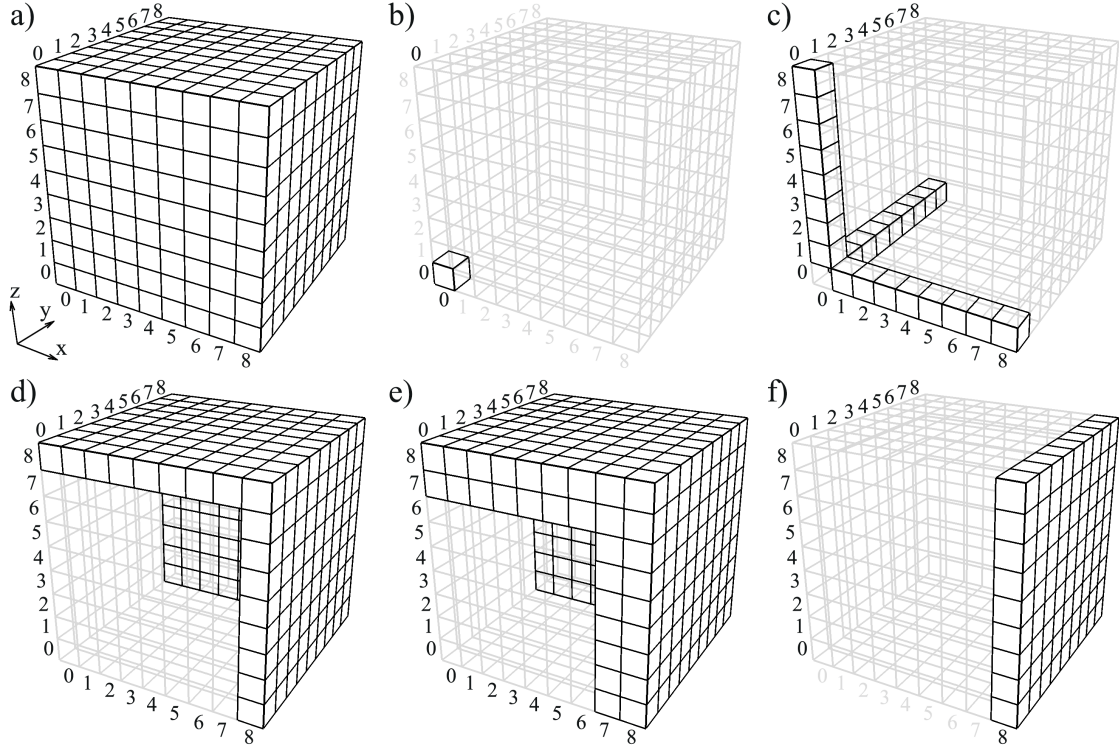
Figure 24. Modal matrix for an element with polynomial order of $P = 8$: (a) the complete matrix; (b) the zeroth mode, $\hat{u}_{000}$; (c) modes purely in the x-, y-, or z-directions, $\hat{u}_{k00}$, $\hat{u}_{0l0}$, and $\hat{u}_{00m}$; (d) highest-frequency modes in all three directions; (e) two highest-frequency modes in all three directions; (f) highest-frequency modes in the x-direction.

procedure is expected to dampen high-frequency oscillations that have contributions from the N'_f highest-frequency modes in three directions, where $N'_f = P - P'$ is the filter strength (65). This is due to the fact that the basis with the lower order, P', does not have the capacity to capture the spatial modes corresponding to the N'_f highest-frequency modes. Note that for the modal filter, N_f is defined as the number of high-frequency modes that are explicitly removed from the modal space, while for the nodal filter, N'_f is defined as the difference between the order

of the two polynomial space $(P - P')$. Both variables indicate the number of high-frequency modes intended to be removed and represent the strength of the filters.

To formulate the nodal filter, first, we look at the procedure for a 1D element. The interpolation and projection may be applied to either nodal sets, Gauss grid or Lobatto grid. In this work, the filter is applied on the Lobatto grid since the endpoint values of the original function are preserved. The first step is to interpolate the original function from a polynomial of degree P to a polynomial of lower degree P' by

$$\widetilde{Q}'\left(X_i'\right) = \sum_{j=0}^{P} h_j\left(X_i'\right)\,\widetilde{Q}(X_j). \tag{4.5}$$

where X_j and $\widetilde{Q}$ are the grid points and the solution values on the original (P) polynomial space, respectively, while primed variables are the same entities on the secondary (P') polynomial spaces. The interpolation can be expressed as matrix-vector product by (59)

$$\widetilde{Q}_i' = I_{ij}^{\text{int}}\,\widetilde{Q}_j, \tag{4.6}$$

where

$$I_{ij}^{\text{int}} = \prod_{k=0,k\neq j}^{P} \frac{X_i' - X_k}{X_j - X_k}, \quad i = 0,\ldots,P', \quad j = 0,\ldots,P, \tag{4.7}$$

is the interpolation matrix. The second step is projecting the function $\widetilde{Q}'(X')$ back to the polynomial space P, resulting the filtered function,

$$\widetilde{Q}^{\text{filt}}(X_j) = \sum_{i=0}^{P'} h_i(X_j) \; Q'(X_i'). \tag{4.8}$$

Similarly, the second operation can be expressed as a matrix-vector form by (59)

$$\widetilde{Q}_j^{\text{filt}} = I_{ji}^{\text{pro}} \; \widetilde{Q}_i', \tag{4.9}$$

with the projection matrix, I_{ji}^{pro} defined by

$$I_{ij}^{\text{pro}} = \prod_{k=0, k \neq i}^{P'} \frac{X_j - X_k'}{X_i' - X_k'}, \quad j = 0, \ldots, P, \quad i = 0, \ldots, P'. \tag{4.10}$$

There are two approaches to extend the 1D interpolation and projection procedures described in Equation 4.5 and Equation 4.8 to 3D space. The first approach is to apply the 1D procedure to all 1D arrays in the x-direction, then in the y-direction, and then in the z-direction. We call this approach, which is used in previous work (55; 59), a series nodal filter. The alternative approach is to generalize Equation 4.5 and Equation 4.8 for 3D space as

$$\widetilde{Q}'(X_l', Y_m', Z_n') = \sum_{i=0}^{P} \sum_{j=0}^{P} \sum_{k=0}^{P} h_i(X_l') h_j(Y_m') h_k(Z_n') \; Q(X_i, Y_j, Z_k) \tag{4.11}$$

and

$$\widetilde{Q}^{\text{filt}}(X_i, Y_j, Z_k) = \sum_{l=0}^{P'} \sum_{m=0}^{P'} \sum_{n=0}^{P'} h_l(X_i) h_m(Y_j) h_n(Z_k) \, \widetilde{Q}'(X_l', Y_m', Z_n'). \tag{4.12}$$

In this approach, which we call a 3D nodal filter, the interpolation and projection defined in Equation 4.11 and Equation 4.12 are sequentially applied to the variables in all 3D elements.

4.3   Isotropic Decaying Turbulence

The results for LES of a 3D isotropic decaying turbulence are presented in this section. The aim is to assess the performance of the modal filter for an isotropic turbulence condition. Different turbulence models, including the modal filter, nodal filter, and a dynamic Smagorinsky model, are tested, and the results are compared with DNS and no-model coarse DNS.

4.3.1   Problem Setup

The problem setup is similar to the isotropic turbulence of Blaisdell *et al.* (72). The simulation is performed in a cube with periodic boundary conditions in three directions. The length of the cube is 2π units in each direction. The domain is divided into six uniformly distributed elements in each direction, resulting in a total of 216 elements. A polynomial order of $P = 8$ is used for the basis functions within each of the elements. The total number of solution (Gauss) points is $N_p = 6^3 \times (8+1)^3 = 157{,}464$.

An initial condition should be specified such that it generates an isotropic and periodic field for the velocity and thermodynamic variables. The procedure outlined by Blaisdell *et al.* (72) for the case "idc96" is followed here to initialize the solution domain. The domain is initialized by a correlated turbulent flow field using specified initial energy spectra. The

spectra follow a top-hat distribution that has non-zero contributions in the wavenumber range of $8 \leq k \leq 16$. In this work, a divergence-free initial field is considered for the thermodynamic variables; therefore, only the mean values of density, pressure, and temperature are specified. The initial velocity fluctuations are purely solenoidal and exist in all three directions. The initial field is first determined from the Fourier coefficients on a uniform grid via a fast Fourier transform (FFT). Then, the field is interpolated from the Fourier grid to the Gauss grid points.

The bulk rms velocity at a fixed time instant is defined as

$$u_{\mathrm{rms}} = \sqrt{\frac{\overline{u_i u_i}}{3}}, \tag{4.13}$$

where the overline denotes a spatial average over the whole domain. Turbulence kinetic energy (TKE) is defined as the integral of the energy spectrum function, $E(k)$, over all wavenumbers,

$$\mathrm{TKE} = \int_0^\infty E(k) \, dk = \frac{1}{2} \, \overline{u_i u_i}. \tag{4.14}$$

4.3.2   Results

The results of applying different filtering procedures on the isotropic turbulence are presented in this section. First, the filters are applied once to the initial field before running the simulation to study the direct effect of the filters on a turbulence field (a priori analysis). Then, the decaying isotropic turbulence is simulated using different filtering approaches, and the performance of the filters in the prediction of the flow statistics are compared (a posteriori analysis).

4.3.2.1   A Priori Analysis

In this section, the effects of the isotropic modal filter and both series and 3D nodal filters on an isotropic turbulence field are considered. The filters are applied one time to the initial field of the 3D isotropic turbulence described above, and the solution fields before and after applying the filter are compared.

First, we apply the filters on the initial 3D field and examine the solution values on a 1D sample line across the domain. Figure 25(a)-(c) shows the u-velocity along a 1D sample line across the domain from the original field and filtered fields obtained from different filtering procedures with different strengths. By applying a stronger filter (larger N_f and N_f') at each step, the solution is expected to become smoother, and the high-frequency features of the signal are expected to weaken. With the modal filtering (Figure 25(a)), it is observed that the solution becomes smoother with each consecutive step, where more high-frequency modes are removed. With the nodal filters, however, this behavior is observed only for weaker filters ($N_f' < 3$). Applying stronger nodal filters appears to introduce inconsistent contributions to the motions, and change the general shape of the function. Such behavior can be seen for both nodal filters in $1.5 < x < 3$ for $N_f' = 5$ and in $4.25 < x < 5.25$ for both $N_f' = 4$ and 5. This means that by applying stronger nodal filters to the flow variables, non-physical effects are superimposed on the lower-frequency motions that could result in incorrect turbulence statistics. This low-frequency effect appears to be stronger for the series nodal filter than the 3D nodal filter. Note that a nodal filter with $N_f' = 4$ or 5 might be too strong for a practical case of LES; however,

visualizing their results help magnify the effects to better understand their differences with modal filtering.

Following the results obtained from a 1D sample signal across the domain, further investigation of the effect of the nodal filter on the modes of the solution is performed. This time, the nodal filter is applied once to all variables in all elements at time $t = 0$, and the average properties among all elements before and after applying the filter are compared (shown later). The amplitude of modes with wavenumber n in element q before applying the filter is defined by

$$A_q(n) = \langle \hat{u}_{klm} \rangle \quad \forall \quad \{k, l, m\} \quad \text{where} \quad \max\{k, l, m\} = n, \quad n = 0, \ldots, P, \qquad (4.15)$$

where $\langle \rangle$ means the average of the set. Examples of these sets are shown in Figure 26 for $n = 6$, 7, and 8. Similarly, the amplitude of modes with wavenumber n in an element after applying the filter is called $A_q^{\text{filt}}(n)$.

The procedure used to study the effects of filters on the modes is as follows. First, we transform the solutions from nodal representation to modal representation via DChT, given by Equation A.4, and store the amplitudes of the modes (Equation 4.15). Then, we apply the filter of interest on the variables of interest and transform the filtered solutions from nodal representation to modal representation. Finally, we compare the amplitude of the filtered modes $(A_q^{\text{filt}}(n))$ with the previously stored original modes $(A_q(n))$. This procedure is used for the nodal filters. The effect of the modal filter on the modes is trivial.

After calculating $A_q(n)$ and $A_q^{\text{filt}}(n)$ for all the elements, the amplitude of each wavenumber is averaged for all the elements throughout the domain to obtain $\langle A(n) \rangle$ and $\langle A^{\text{filt}}(n) \rangle$.
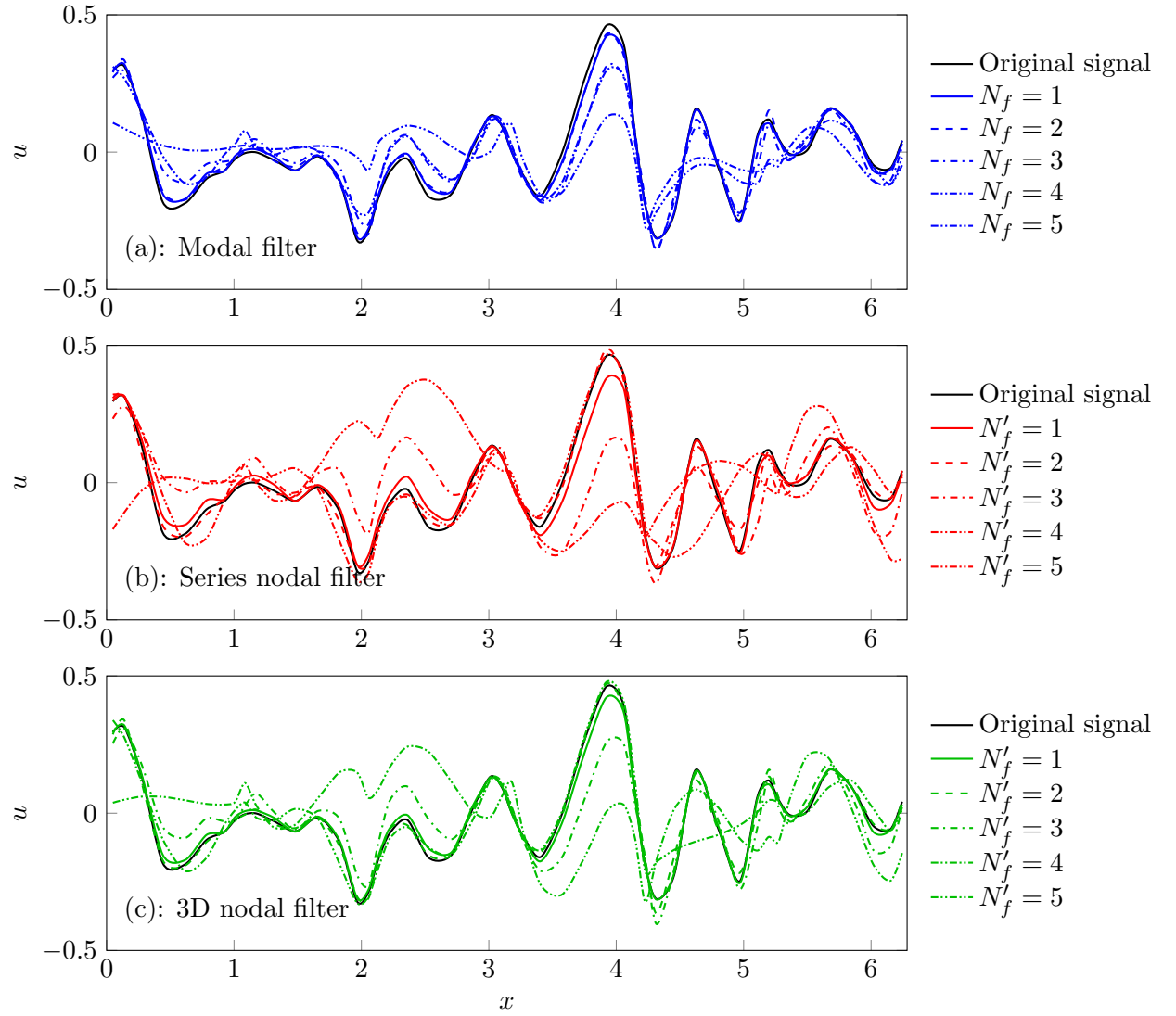
Figure 25. The effect of (a) the modal filtering, (b) series nodal filtering, and (c) 3D nodal filtering on a 1D signal. The signal is the u-velocity on a sample line through the isotropic turbulence field.
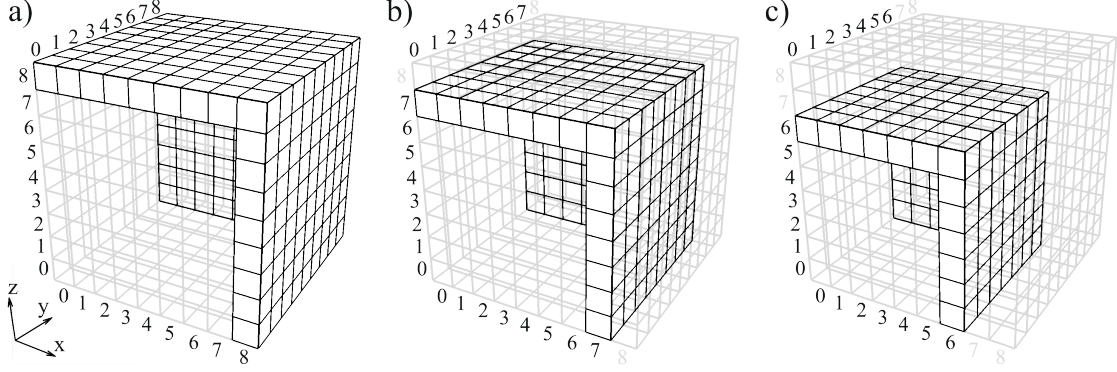
Figure 26. The entries of the modal matrix that contribute to motions with wavenumber n for (a) $n = 8$, (b) $n = 7$, and (c) $n = 6$.

Here, we are interested in the effect of the nodal filter on the amplitudes of modes at different wavenumbers. Therefore, for each wavenumber, we look at the amplitude of each wavenumber after applying the filter, relative to the amplitude of the same wavenumber before applying the filter: $\widetilde{A}(n) = \langle A^{\text{filt}}(n)\rangle / \langle A(n)\rangle$. This study identifies the statistical effect of the filters on the amplitude of each wavenumber. An ideal filter would remove the high wavenumbers, and at the same time will not affect the low wavenumbers.

Figure 27(a) shows the relative amplitudes of modes $(\widetilde{A}(n))$ at each wavenumber (n) after applying the modal filter with different strengths (N_f). The motions are calculated based on u-velocity. Note that even though some adjacent points are connected with a sloped line, they do not represent smooth transitions, but a sharp cutoff, i.e., the relative amplitudes of the modes are one and zero for two adjacent wavenumbers. Not surprisingly, it is observed that by applying a modal filter, the last N_f modes with the highest frequencies are completely

removed, and the relative amplitude of the lower-frequency modes remain as one, which means those modes are not affected by the filtering procedure.

Figure 27(b) and (c) show the effect of series and 3D nodal filters on the u-velocity modes, respectively. By interpolating the solutions back and forth to a lower polynomial order, $P' = P - N'_f$, the motions associated with the N'_f modes with highest frequencies are expected to be completely removed with no effect on the other modes with lower frequencies. From Figure 27(b) it is observed that by applying the series nodal filter with $N'_f = 1$, the mode with the highest frequency ($n = 8$) is completely removed. However, the process has some weak effects on the lower-frequency modes as well—two adjacent modes, i.e., $n = 6$ and 7, are slightly weakened. It is also observed that the filter weakens the motions at $n = 6$ more than it does at $n = 7$. This behavior is not expected from a low-pass filter, where the effectiveness of the filter should change smoothly or sharply from high-frequency to low-frequency wavenumbers. For $N'_f = 2$, the two modes with the highest frequencies ($n = 7$ and 8) are completely removed. However, again, some of the lower-frequency modes are also affected. This time, three adjacent modes ($n = 4$, 5, and 6) are weakened. Similarly, for $N'_f = 3$, four adjacent modes are affected. This low-frequency effect dramatically escalates for $N'_f > 3$ such that the filtering process significantly changes the lowest-frequency modes. The value of $\widetilde{A}(n)$ at three low-frequency end of the spectra, i.e., $n = \{0, 1, 2\}$, fall outside the plot frame and are given by $\widetilde{A}(n) = \{1.81, 2.66, 2.04\}$ and $\{-1.28, -2.76, -1.97\}$ for $N'_f = 4$ and 5, respectively. This observation conveys that the series nodal filter, especially at higher strengths, provokes significant contributions to the low-frequency motions and is consistent with the observation in Figure 25(b), where the general

shape of the function changes for $N_f' > 3$. This unintended contamination of the low-frequency motions may remove more turbulent motions than what is intended and severely affect the first-, as well as second-order statistics.

A less severe version of the above-mentioned low-frequency effect is also observed in the 3D nodal filter, shown in Figure 27(c). The 3D nodal filter acts similar to the modal filter, i.e., the filtering procedure does not affect the lower-frequency modes, only for $N_f' = 1$. For higher values of N_f', the low-frequency effect is present, but, compared with the series nodal filter, fewer adjacent modes are changed at a lower rate. Also, for $N_f' = 2$ and 3, the amplitudes of the modes adjacent to the filter cutoff, i.e., $n = 6$ and 5, respectively, are increased by the filtering procedure, which could increase the motions at unintended scales and contaminate the flow statistics. The low-frequency effect becomes severe for $N_f' = 5$; the point $\widetilde{A}(1) = -0.73$ for $N_f' = 5$ falls outside the plot frame. This is a new observation and shows that the nodal filter accomplishes one of the two expected goals: It does remove the motions within a certain frequency range, but it does not leave the lower-frequency motions unaffected.

4.3.2.2 A Posteriori Analysis

LES of the isotropic decaying turbulence case is conducted using different filtering procedures to compare their performance. A DNS of the same flow is also simulated as the benchmark. Turbulence statistics such as the decay of the TKE, the energy spectra, and the dissipation spectra are used for comparison. The filters are applied to density, three components of velocity, and pressure at each time step. The initial turbulent Mach number based on u_{rms} is $M_{T,0} = 0.3$,
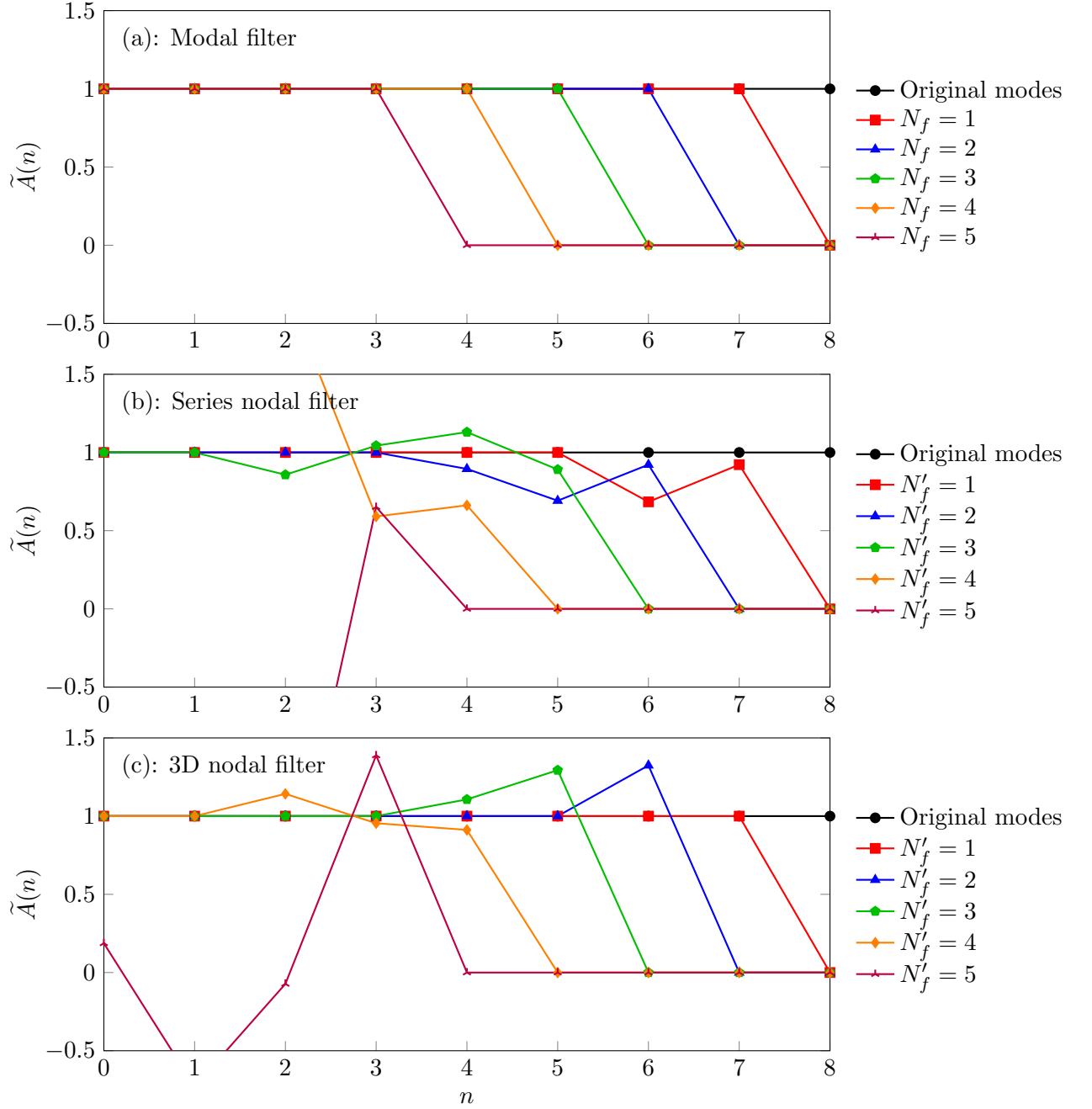
Figure 27. The effect of (a) the modal filtering, (b) series nodal filtering, and (c) 3D nodal filtering on the magnitude of motions corresponding to different modes. The motions are u-velocity throughout the domain.

and the initial Taylor Reynolds number is $Re_\lambda = 40$. More details of the problem setup are given in Sengupta (59).

The grid used for DNS consists of $6^3 = 216$ elements, uniformly distributed in three directions. The polynomial order used for DNS is $P = 15$. This grid has been shown to be sufficiently resolved for DNS of the described isotropic turbulence case (59). The elements of the grid used for LES are the same as those used for DNS; however, the polynomial order for LES is $P = 8$ as opposed to $P = 15$.

A coarse DNS case is also simulated using the coarse mesh of LES without applying a turbulence model. Also, a dynamic Smagorinsky model (49) is implemented and tested for comparison. A nodal filter with $N_f' = 1$ is used as the test filter in the dynamic model.

Figure 28(a) and (b) show the energy spectra and the dissipation spectra, respectively, of the isotropic decaying turbulence simulation at time $t = 3.2$ for the DNS and coarse DNS cases. The energy spectrum is compared with previously published data of Blaisdell *et al.* (73). A good agreement with previous data is observed for the DNS case. The sharp drop-off in the spectrum at high wavenumbers indicates a resolved DNS. The work of Blaisdell *et al.* (73) used a Fourier-spectral method with $96^3 = 884{,}736$ grid points. The present DNS grid has the same number of degrees of freedom as the previous work with $216 \times 16^3 = 884{,}736$ Gauss grid points. This conclusion is consistent with the validation study of Jacobs *et al.* (74). On the other hand, the coarse DNS case is unable to capture the expected drop-off in both energy and dissipation spectra for $k > 13$.
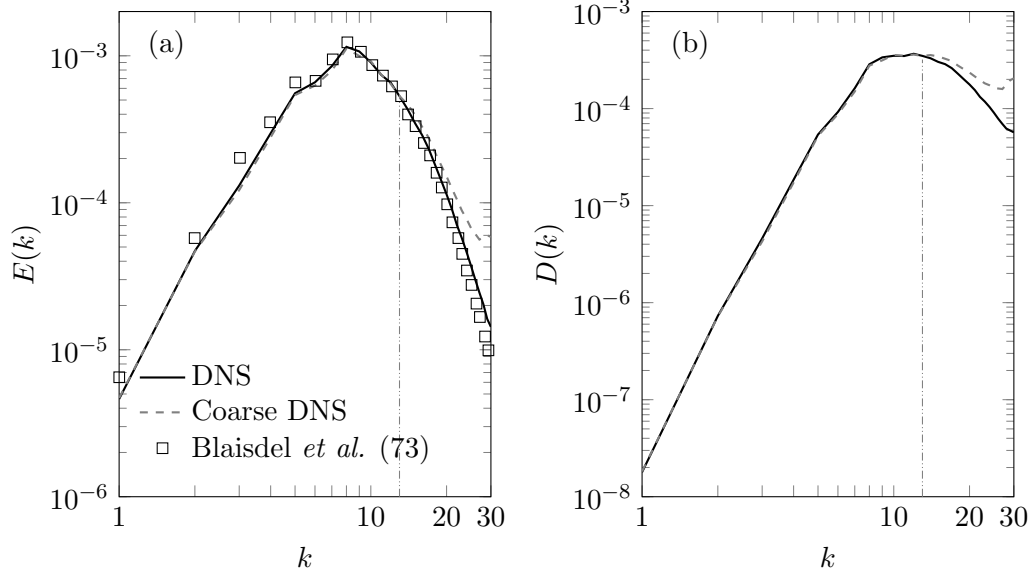
Figure 28. (a) The energy spectra and (b) dissipation spectra for the isotropic decaying turbulence at time $t = 3.2$.

Figure 29(a)-(c) shows the energy spectra of the isotropic decaying turbulence using the three different filtering approaches. The spectra are compared with DNS, coarse DNS, and the results obtained from the dynamic Smagorinsky model. All three methods provide steeper drop-off than the coarse DNS case at high wavenumbers, which is expected. It means that the filters are serving as a drain for the turbulence energy cascade. Except for the 3D nodal filter, removing two modes results in a steeper drop-off than removing one mode; a stronger filter damps more energy from the high wavenumber portion of the spectrum. For the nodal filters, the spectra are affected at midrange wavenumbers (for both nodal filters) and low wavenumbers (for series nodal filter). This undesired side effect could induce non-physical contributions to
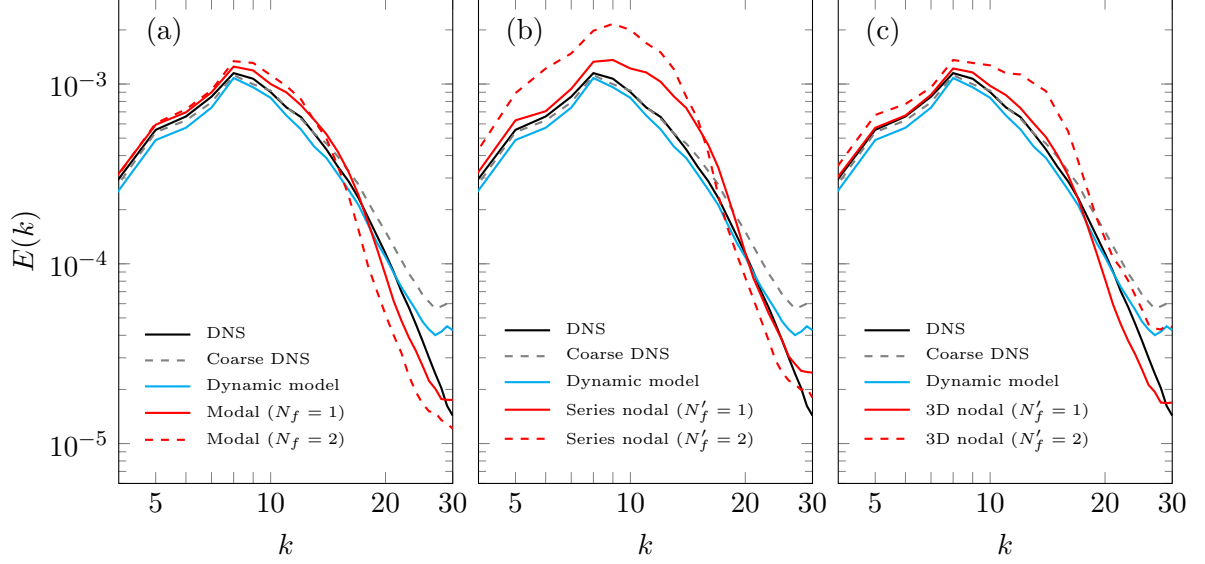
Figure 29. The energy spectra of the isotropic decaying turbulence at time $t = 3.2$ for (a) the modal filter, (b) series nodal filter, and (c) 3D nodal filter as compared with DNS, coarse DNS, and dynamic model.

the larger-scale motions of the turbulence and result in incorrect turbulence statistics. This behavior is not expected since a low-pass filter ideally acts on the high wavenumbers only. The best agreement with DNS is obtained by removing one mode using the modal filter. This method provides a better prediction of the energy spectra than the dynamic model, which could be due to the lack of enough eddy viscosity introduced by the dynamic model.

The decay of the TKE, defined by Equation 4.14, for the isotropic decaying turbulence is shown in Figure 30(a)-(c) for the modal filtering, the series nodal filtering, and the 3D nodal filtering procedures, respectively. The results are compared with DNS and the dynamic model cases. It is observed that the TKE has a noticeable deviation from DNS for the series nodal

filter, with $N_f' = 1$ and 2, for $t > 1$. The 3D nodal filter, with $N_f' = 2$, also overpredicts the TKE from the beginning of the simulation ($t = 0$). The nodal filters generally predict a lower rate of decay of the TKE compared to the DNS case. The modal filtering, for both filter strengths $N_f = 1$ and 2, as well as the dynamic model, provides good agreement with the DNS.

It is observed from the simulations of the isotropic turbulence that the nodal filtering not only drastically alters the low-frequency content but amplifies the lower modes due to $|\widetilde{A}(n)| > 1$ and introduces large phase shifts due to negative values of $\widetilde{A}(n)$. The consequence of this observation is clearly demonstrated in Figure 29, where the energy of LES cases are considerably higher than DNS, which in reality should be the opposite. This phenomenon is due to the aliasing inherent in the interpolation-based operations, Equation 4.11 and Equation 4.12, which causes the redistribution of energy between modes. Based on the above-mentioned observations, it is strongly recommended to avoid using the explicit nodal filter for LES. Therefore, the modal filter is used for further LES of turbulent channel flow in this work.

4.4   Channel Flow

The periodic turbulent channel flow between two parallel plates is a well-studied benchmark for turbulence models (43; 44; 56; 64; 75). It provides a simple flow that assesses the performance of turbulence models near the wall. The tests with isotropic decaying turbulence, presented in the previous section, demonstrated the superior performance of the modal filter over the nodal filters. Therefore, for further simulations of channel flow, only the modal filtering procedure is employed.
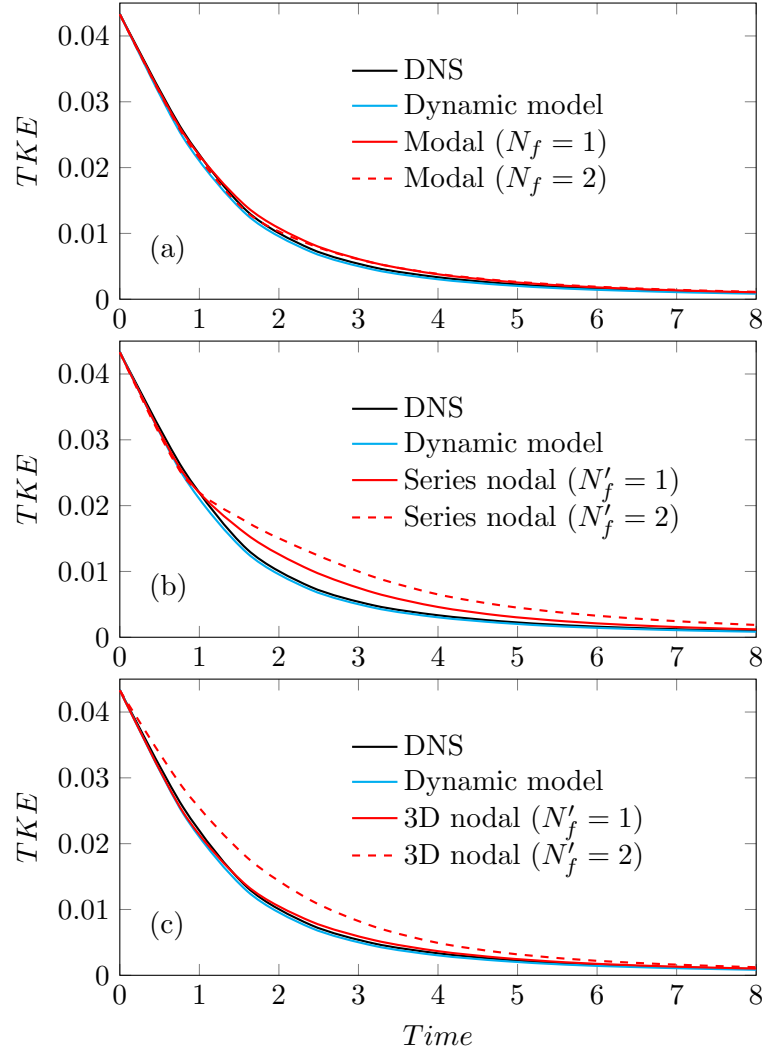
Figure 30. Evolution of the turbulent kinetic energy (TKE) for (a) the modal filter, (b) series nodal filter, and (c) 3D nodal filter, compared with DNS and the dynamic Smagorinsky model.

4.4.1   Problem Setup

In the present work, we perform LES of a 3D periodic turbulent channel flow to study the performance of the modal filtering procedure in the case of wall-bounded turbulence. First- and second-order turbulent statistics are used to assess the accuracy of the calculations. The DNS of Lee and Moser (30) at the friction Reynolds number of $Re_\tau = 544$ is used as the reference.

4.4.1.1   Computational Domain

The channel flow configuration is shown in Figure 31. The flow runs between two parallel no-slip isothermal walls with a temperature of $T_w = 1$, which are placed in the xz-plane. The boundaries of the domain in the streamwise (x) and spanwise (z) directions are periodic. The dimensions of the computational domain are $L_x = 4\pi$, $L_y = 2$, and $L_z = 2\pi$ in the streamwise, wall-normal, and spanwise directions, respectively. The domain dimensions in terms of the wall unit are $L_x^+ \approx 6{,}800$, $L_y^+ \approx 1{,}100$, and $L_z^+ \approx 3{,}400$. Throughout the chapter, variables with the superscript $^+$ are scaled by wall units. These channel dimensions are used in previous DNS (24), and are shown to be sufficiently large to encompass the largest scale of turbulence by demonstrating two-point correlations in the periodic directions (23).

4.4.1.2   Flow Conditions

The bulk velocity of the flow ($\overline{U}$), the channel half-height (δ), the bulk density ($\bar{\rho}$), and the wall temperature (T_w) are taken as the reference velocity, reference length, reference density, and
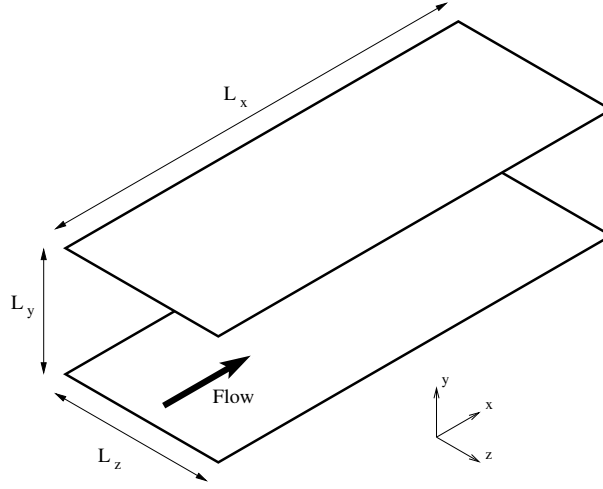
Figure 31. Schematic of the computational domain of the channel flow.

reference temperature, respectively. The friction Reynolds number is defined by $Re_\tau = u_\tau \delta / \nu$, where ν is the fluid's kinematic viscosity and

$$u_\tau = \sqrt{\frac{\nu \left.\frac{\partial u}{\partial y}\right|_{\text{wall}}}{Re_f}} \tag{4.16}$$

is the friction velocity. All present channel flow simulations are performed at $Re_\tau \approx 544$. The exact value of the friction Reynolds number varies for each case based on the calculated slope of the streamwise velocity adjacent to the wall. This friction Reynolds number corresponds to a reference Reynolds number of $Re_f = 10{,}000$ based on the reference scales. The reference Mach number, based on the reference temperature and velocity, is $M_f = 0.4$. The heat capacity ratio is assumed fixed at $\gamma = 1.4$ for air, and the reference Prandtl number is $Pr = 0.72$.

The flow in a physical channel is normally driven by a negative pressure gradient in the streamwise direction $(\mathrm{d}p/\mathrm{d}x)$. Here, a force term, which is dynamically adjusted, is applied to retain a constant mass flow rate. The forcing algorithm employed in the present work was introduced by Lenormand *et al.* (36).

4.4.1.3 Grid Resolution

The grid used for the LES of the periodic channel flow (shown in Figure 32) has 20, 12, and 30 elements in the streamwise, wall-normal, and spanwise directions, respectively. The polynomial order of the basis functions within the elements is $P = 6$. This results in a total of 2,469,600 Gauss collocation points. The elements are uniformly distributed in the periodic directions (x and z). A hyperbolic tangent function of the form

$$\frac{y_n}{L_y} = \frac{1}{2}\left(1 - \frac{\tanh\left[\lambda(\frac{1}{2} - \frac{n}{N_y})\right]}{\tanh\left[\lambda/2\right]}\right), \quad n = 0, \ldots, N_y, \tag{4.17}$$

is used for the distribution of the elements in wall-normal direction. In Equation 4.17, y_n is the location of the interfaces of the elements in the y-direction, N_y is the number of elements in the y-direction, and λ is an adjustable coefficient that determines the compactness of the elements adjacent to the walls. The average grid (Gauss points) spacings in the periodic directions in wall units are $\overline{\Delta x^+} \approx 49$ and $\overline{\Delta z^+} \approx 16$, and the wall-normal grid spacing ranges in $0.17 < \Delta y^+ < 43$. The details of the grid is included in Table V; the grid used in this section is labeled as *P6-B*.
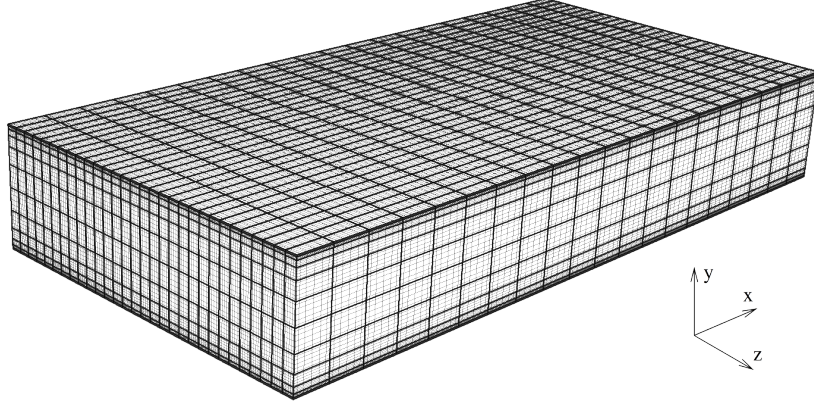
Figure 32. The grid used for LES of the channel flow (grid P6-B). The element interfaces are shown with black lines, while the intersections of the gray lines indicate the locations of the Gauss grid points.

4.4.1.4   Initialization and Transition to Turbulence

The streamwise velocity is initialized with a laminar parabolic profile with a mean value of $\overline{U_0}$ as

$$u_0(y) = -6\left[\left(\frac{y}{2}\right)^2 - \left(\frac{y}{2}\right)\right](1 + \epsilon), \tag{4.18}$$

where ϵ is a 10% random disturbance intended to help accelerate the transition to turbulence. The spanwise and wall-normal velocities are initialized as zero. The initial temperature follows a laminar Poiseuille profile (See Appendix C) as

$$T(y) = T_w + \frac{3(\gamma - 1)}{4}Pr_f M_f\left[1 - (y - 1)^4\right]. \tag{4.19}$$

TABLE V

DETAILS OF THE GRIDS USED FOR DIFFERENT CASES OF LES OF THE CHANNEL FLOW. POINTS IN Y_{10}^+ IS THE NUMBER OF GRID POINTS BELOW $Y^+ = 10$ NEAR THE WALL, AND ΔT IS THE AVERAGE TIME STEP SIZE REQUIRED FOR EACH GRID.

Case	P	Number of elements	Number of grid points	Total grid points	y_{min}^+	Points in y_{10}^+	λ	$\Delta t \times 10^4$
P6-B	6	$20 \times 12 \times 30$	$140 \times 84 \times 210$	2,469,600	0.167	5	4.5	6.81
P6-H	6	$28 \times 17 \times 42$	$196 \times 119 \times 294$	6,857,256	0.121	8	4.3	5.07
P10-B	10	$13 \times 7 \times 19$	$143 \times 77 \times 209$	2,301,299	0.157	4	4.5	5.96
P10-H	10	$20 \times 12 \times 30$	$220 \times 132 \times 330$	9,583,200	0.068	7	4.5	2.84

The density is initialized at $\rho_0 = 1$, and the initial pressure is calculated from the equation of state.

Our preliminary tests showed that the initial disturbance that is introduced to expedite the transition to turbulence gradually decays, and the transition does not occur. Neither an increase in the magnitude of the initial disturbance nor a temporary increase in the Reynolds number resulted in a transition to turbulence. Instead, the simulation is started using a significantly coarse grid with a polynomial order of $P = 2$ compared to the original order of $P = 7$. The truncation error caused by the low resolution is sufficiently large to provide the necessary disturbance for the transition to turbulence. Once the transition completes, the solution is spectrally interpolated to a new grid with higher resolution ($P = 3$), and the simulation is continued at the new resolution for a few flow-through times. To ensure stability, the solution is interpolated gradually to higher resolution grids using the same approach until reaching the

desired resolution of $P = 6$. More details of the transition procedure is provided in Jacobs (10) and Ghiasi *et al.* (22).

4.4.2   <u>Results</u>

LES of the periodic channel flow has been performed using the modal filtering procedure. Different tests have been conducted, and the results are compared with the DNS of Lee and Moser (30), which is used as the reference in this study.

The rms velocity fluctuation in the x_i-direction is defined as $u''_{i,rms} = \{u''_i u''_i\}^{1/2}$, and the scaled rms velocity fluctuation is $u''_{i,rms}{}^+ = u''_{i,rms}/u_\tau$. Here, $\{\}$ is the Favre average, which is defined by $\{f\} = \langle \rho f \rangle / \langle \rho \rangle$, where $\langle \rangle$ is the Reynolds (ensemble) average. Also, the single prime, $'$, and double prime, $''$, denote the turbulent fluctuations with respect to the Reynolds and Favre averages, respectively.

A case using the dynamic Smagorinsky model is also simulated for comparison. The value of the dynamic Smagorinsky coefficient, C_s, is averaged within each element in the periodic directions to ensure stability (59).

Before performing the LES of the channel flow using the modal filter, we examined the amplitudes of the modes for the coarse DNS (no-model) case. The amplitude of the nth mode in element m, is denoted by $A_m(n)$ and is defined by Equation 4.15 (See Figure 26). We expect this quantity to be statistically only a function of the distance of the element from the wall. Hence, we categorize the elements into three levels: Level 1: elements adjacent to the wall, level 2: elements that are one element away from the wall, until level 6: elements nearest to the
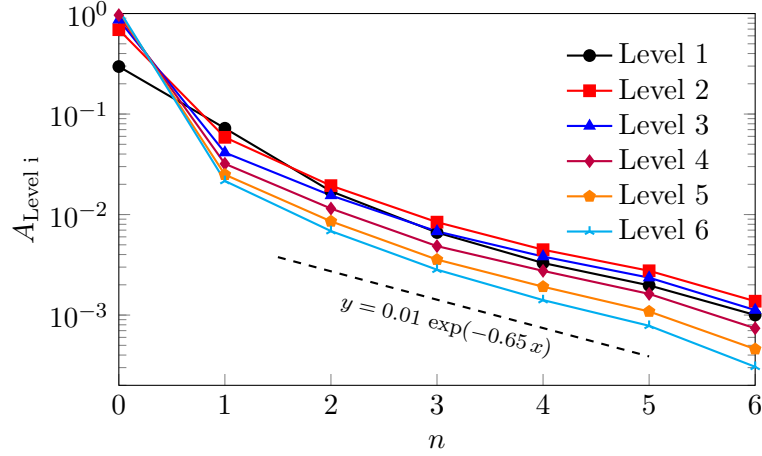
Figure 33. The magnitude of the modes of the streamwise velocity in the coarse DNS of the channel flow. Lower level number indicates elements closer to the walls.

core of the channel. Then, we average the amplitudes of each mode over all elements within the same level to obtain $A_{\text{Level}\_l}(n)$, where $l = 1, \ldots, 6$.

Figure 33 presents the amplitudes of the modes of the streamwise velocity at different levels. The zeroth mode represents the bulk value of the quantity (streamwise velocity). The amplitude of this mode is greater for the higher levels (see $n = 0$) because the magnitude of the streamwise velocity is higher away from the wall. In contrast, the higher modes ($n > 0$) represent the spatial change of the quantity (streamwise velocity). The amplitudes of these modes are lower for the higher levels because the spatial changes of the streamwise velocity decrease as we get closer to the core of the channel. It is also observed that regardless of the distance from the wall, the amplitudes of the modes decrease exponentially for successive modes.

4.4.2.1   Filtering Strategy

As mentioned before, the filters were applied at every time step to the density, all three components of velocity, and pressure in the simulations of the isotropic turbulence. Our preliminary tests with the channel flow revealed that applying the filter at every time step results in excessively dissipated turbulence and incorrect statistics (not shown). Further tests showed that applying the filter every 100 time steps (equivalent to approximately 0.07 time units) provides good agreement with DNS (shown in the next section).

Then, we studied the effect of applying a weaker filter, by blending the filtered values with the unfiltered values, more frequently. Here, we apply the isotropic modal filter with $N_f = 1$ at different frequencies: $f = 1, 0.1, 0.02,$ and 0.01 (the unit of the frequency is 1/time step), which correspond to filtering every 1, 10, 50, and 100 time steps, respectively. In order to maintain the overall strength of the filter in all these cases, a function is used to update the solution values with a combination of the filtered values and the original values (57). The solution values are updated to the effective value of

$$Q_{\text{eff}} = \alpha \, Q_{\text{filt}} + (1 - \alpha) \, Q_{\text{orig}}, \tag{4.20}$$

where Q_{filt} and Q_{orig} are the filtered and original values, respectively. By choosing the combination coefficient to be $\alpha = 1$, we can disable the effect of the combination function, which was the case for previous simulations. Here, the value of α is chosen to be 0.01, 0.1, 0.5, and 1 for
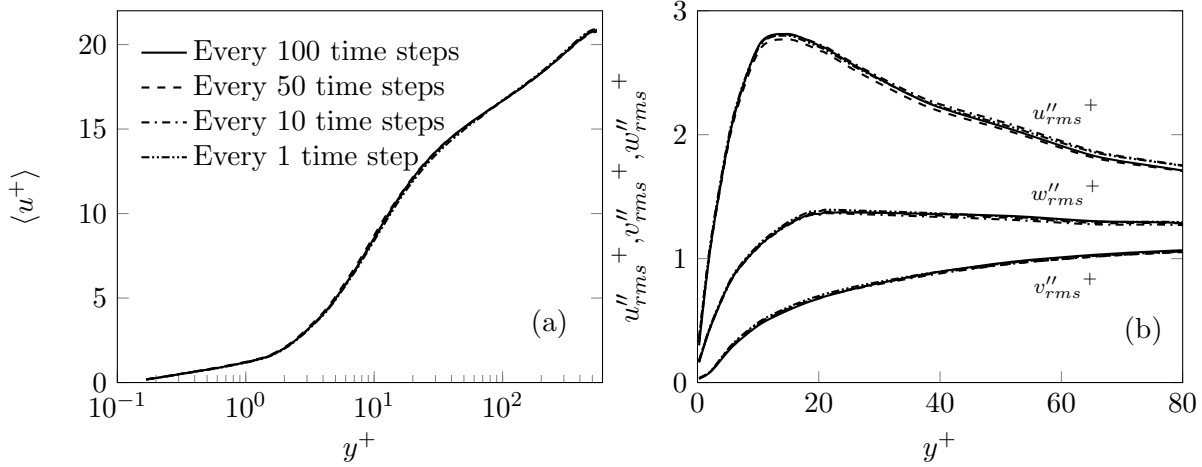
Figure 34. (a) Mean streamwise velocity and (b) rms velocity fluctuations of LES of the channel flow using modal filter with $N_f = 1$ applied at different frequencies.

the cases with $f = 1$, 0.1, 0.02, and 0.01, respectively. Therefore, the cumulative strength of the filter, which is defined by $f \times \alpha$, remains the same for all cases.

Figure 34 depicts the scaled mean streamwise velocity and rms velocity fluctuations for the four different frequencies of the modal filter. It is observed that the frequency of the filter has nearly no effect on the first- and second-order statistics of the flow, while the cumulative strength of the filter is maintained. Therefore, for all present simulations of the channel flow using the modal filter, the filter is applied to density, all three components of velocity, and pressure every 100 time steps, without blending ($\alpha = 1$).

4.4.2.2   Isotropic Modal Filter

The isotropic modal filtering is applied for $N_f = 1$ and 2, which correspond to removing one and two modes with highest frequencies, respectively. Since this filter, according to
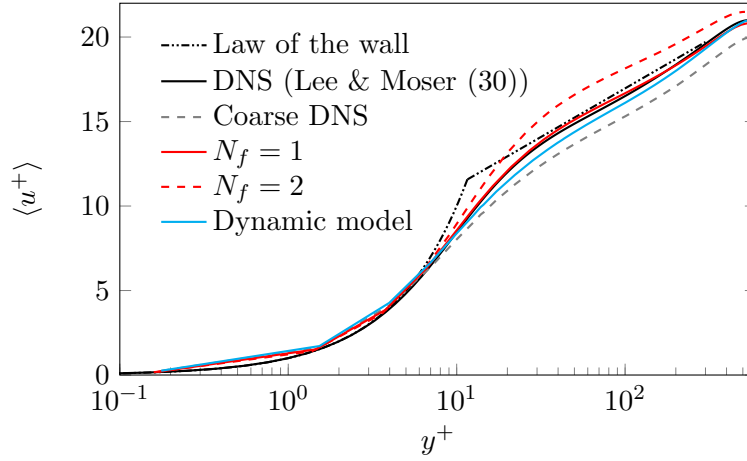
Figure 35. Mean streamwise velocity for the LES of the channel flow using the modal filtering with different strengths. The DNS of Lee and Moser (30) is used as the reference.

Equation 4.3, removes the high-frequency modes in all three directions, it is called an isotropic modal filter. Figure 35 shows the scaled mean streamwise velocity, $\langle u^+ \rangle$, as a function of the distance from the wall in wall units, y^+. The profiles are compared with those from DNS, Coarse DNS, and the dynamic model. The difference between the DNS results and other cases in $0.1 < y^+ < 4$ are related to the plotting method; other cases have fewer solution points near the wall than DNS, and the solution values are connected by straight lines. It is observed that all cases predict the same velocity profile up to $y^+ \approx 8$. Further away from the wall, the case with no model (coarse DNS) underpredicts the mean velocity profile, the modal filtering with $N_f = 2$ overpredicts the profile, the dynamic model predicts close values to DNS, and the modal filtering with $N_f = 1$ provides excellent agreement with DNS. In fact, it shows slightly better velocity prediction than the dynamic model.

The friction Reynolds numbers for all cases are provided in Table VI. The simulations in this section appear under the *base resolution* in the table. The closest prediction of the friction Reynolds number relative to the DNS value is provided by the modal filter with $N_f = 1$ with only 1.43% error. The modal filter with $N_f = 2$ and the case with no model significantly underpredict and overpredict the quantity, respectively. A large error in calculation of the friction Reynolds number indicates the inability to accurately calculate the slope of the mean velocity at the wall.

The rms of velocity fluctuations are shown in Figure 36. The modal filter with $N_f = 1$, as well as the dynamic model, give good predictions of the streamwise component (Figure 36(a)) as compared with DNS. With $N_f = 2$, however, the streamwise rms is significantly overpredicted for $y^+ > 7$. The coarse DNS also overpredicts the quantity near the wall ($y^+ < 10$). A closer look at the near-wall region reveals that the modal filtering provides better streamwise rms than the dynamic model, regardless of the filter strength (N_f). The reason the profiles do not meet at the axis origin ($\{0, 0\}$) is that the solutions are calculated on the Gauss grid points, and these collocation points, according to Equation 3.1, do not exist on the element interfaces. The modal filtering with $N_f = 1$ as well as the dynamic model predict close values of wall-normal rms as shown in Figure 36(b). The modal filter with $N_f = 2$ and the coarse DNS case underpredict and overpredict the profile, respectively. All present turbulence models do improve the prediction of the rms of velocity in the spanwise direction (Figure 36(c)), compared to the coarse DNS case. It is observed that modal filtering, with $N_f = 2$, has excellent agreement with DNS near the wall ($y^+ < 30$), while $N_f = 1$ gives better prediction at regions away from the wall ($y^+ > 40$).

This implies that stronger modal filtering is desired more near the wall than it is away from the wall.

4.4.2.3   Grid Independence Study

The simulation of the periodic channel flow with the base resolution (grid P6-B) that is presented in section 4.4.2.2 is performed using a grid with higher resolution to ensure the grid independency. The case that provides the closest results to DNS, i.e., $N_f = 1$, is chosen for the grid resolution study. A new grid with a higher number of elements in all three directions that features the same polynomial order of $P = 6$ is considered. The high-resolution grid has 28, 17, and 42 elements in the streamwise, wall-normal, and spanwise directions, respectively. The details of this grid is included in Table V under case *P6-H*.

Figure 37 compares the mean streamwise velocity and rms velocity fluctuations based on the base and high-resolution grids. It is observed that the mean and fluctuations of the velocity do not significantly change by increasing the resolution.

4.4.2.4   Filter Strength (N_f)

In the simulations presented in the previous sections, it was observed that the best agreement with DNS is obtained by the choice of $N_f = 1$. One may ask the questions: Is $N_f = 1$ always the best choice? What factors determine the correct choice of the filter strength (N_f)? To answer these questions, we perform some tests and study the effect of the polynomial order and h-resolution on the best choice of N_f. We consider two polynomial orders of $P = 6$ and 10, and for each P, we consider two grids with different h-resolutions. The details of the four grids
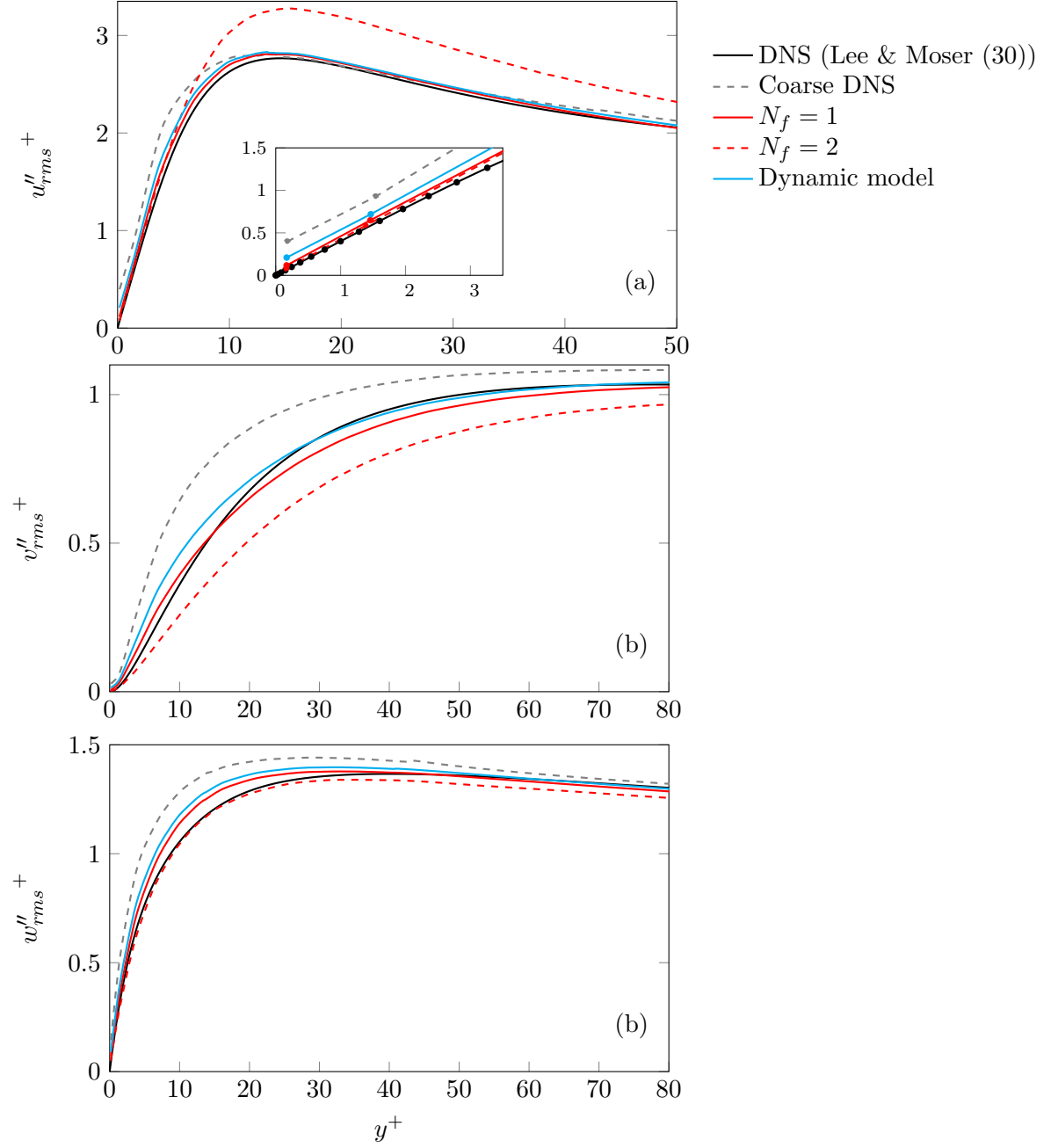
Figure 36. Rms velocity fluctuations for the channel flow in the (a) streamwise (with magnified near-wall region), (b) wall-normal, and (c) spanwise directions using the modal filtering. The profiles are compared with DNS of Lee and Moser (30), coarse DNS, and the dynamic model.
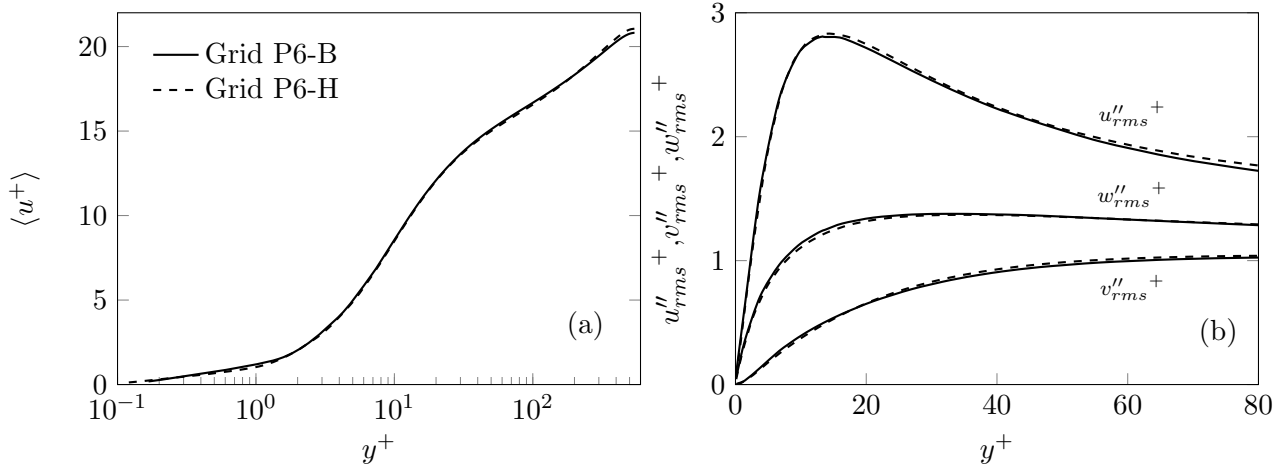
Figure 37. Comparison of (a) mean streamwise velocity and (b) rms velocity fluctuations of LES of the channel flow with modal filter with $N_f = 1$ using the base (grid P6-B) and high resolution (grid P6-H) grids.

are included in Table V. For each of the four grids, we perform the LES using different modal filter strengths (N_f) and compare the results.

Table VI presents the friction Reynolds numbers for all cases with $P = 6$. It is observed that for both resolutions, the friction Reynolds number decreases by increasing the filter strength. The important observation here is that regardless of the h-resolution, the smallest error with respect to the DNS case is obtained by $N_f = 1$. Table VII presents the same quantity for cases with $P = 10$. The decrease in the friction Reynolds number by increasing the filter strength is again observed for $P = 10$. It is also shown that the best agreement with DNS is achieved using $N_f = 3$, again regardless of the h-resolution.

TABLE VI

THE FRICTION REYNOLDS NUMBERS PREDICTED BY $P6$ CASES AS COMPARED
WITH DNS VALUE OF $RE_\tau = 544$. NOTE THAT $N_F = 0$ MEANS A COARSE DNS
WITH NO MODAL FILTER.

N_f	Base resolution		High resolution	
	Re_τ	Error	Re_τ	Error
0	575.5	5.79 %	558.6	2.68 %
1	545.4	0.26 %	543.2	-0.15 %
2	517.1	-4.95 %	527.9	-2.96 %

Figure 38(a) compares the mean velocity profiles of the channel flow for the cases of the modal filter with different strengths (N_f) that are performed on the base resolution grid with $P = 6$ (grid P6-B). It is observed that the best comparison with DNS is obtained by $N_f = 1$. Figure 38(b) presents the same velocity profile for the high resolution grid (P6-H). The closest profile to that of the DNS case is again obtained by $N_f = 1$. The results for $P = 10$ are presented in Figure 38(a) and (b). It is observed that, for both resolutions, the best agreement with DNS is provided by $N_f = 3$. The important observation here is that the same value of N_f is the best choice for both h-resolutions as long as the polynomial order is the same. Therefore, the choice of N_f is dependent on only the polynomial order, and not on the h-resolution. However, regardless of P and N_f, increasing the h-resolution improves the predictions of friction Reynolds number and mean velocity.
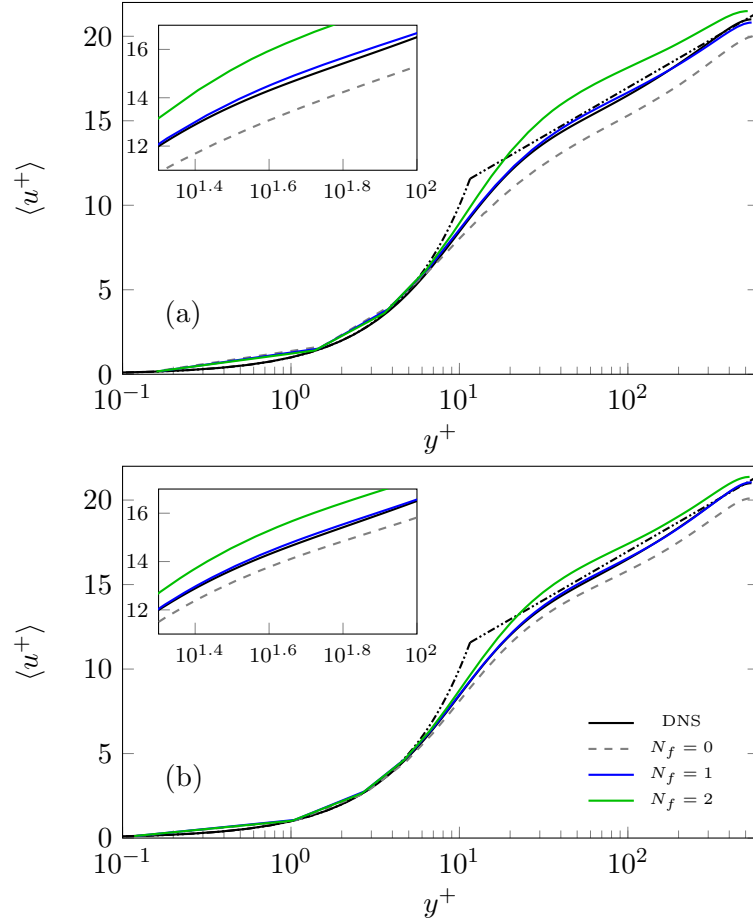
Figure 38. Mean streamwise velocity for the LES of the channel flow with $P = 6$ using the modal filter with different strengths (N_f) based on (a) the base resolution grid (P6-B) and (b) the high resolution grid (P6-H). The DNS of Lee and Moser (30) is used as the reference. The boxes inside the plots show magnified versions.
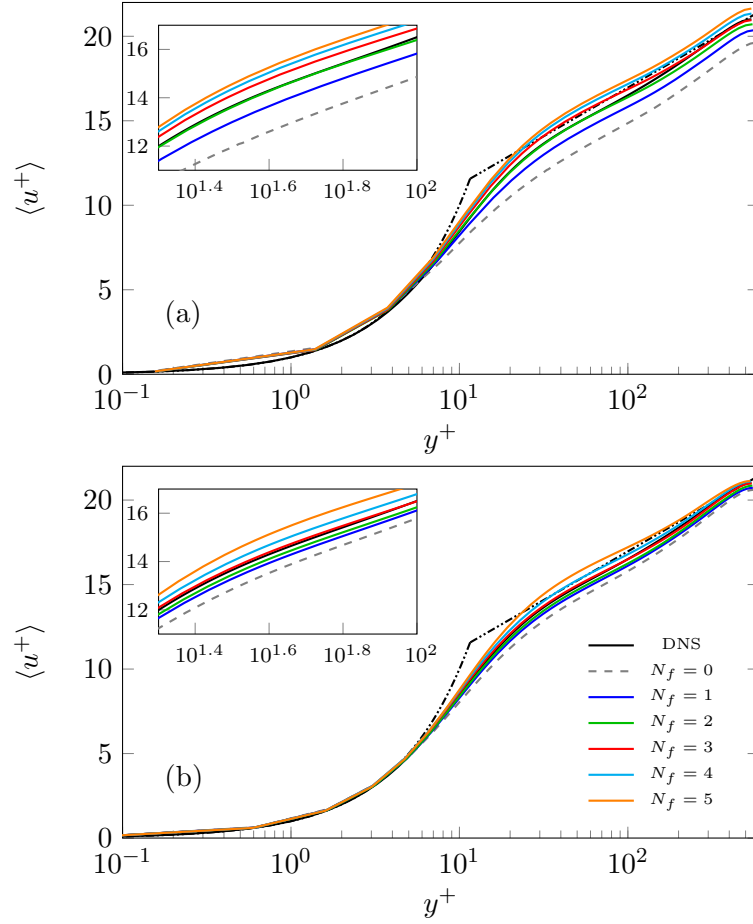
Figure 39. Mean streamwise velocity for the LES of the channel flow with $P = 10$ using the modal filter with different strengths (N_f) based on (a) the base resolution grid (P10-B) and (b) the high resolution grid (P10-H). The DNS of Lee and Moser (30) is used as the reference. The boxes inside the plots show magnified versions.

TABLE VII

THE FRICTION REYNOLDS NUMBERS PREDICTED BY $P10$ CASES AS COMPARED WITH DNS VALUE OF $RE_\tau = 544$. NOTE THAT $N_F = 0$ MEANS A COARSE DNS WITH NO MODAL FILTER.

N_f	Base resolution		High resolution	
	Re_τ	Error	Re_τ	Error
0	587.0	7.90 %	559.2	2.79 %
1	563.0	3.50 %	553.0	1.65 %
2	551.7	1.41 %	549.7	1.05 %
3	543.0	-0.18 %	544.7	0.13 %
4	533.3	-1.97 %	539.2	-0.89 %
5	525.9	-3.33 %	533.6	-1.92 %

4.4.2.5 Anisotropic Modal Filter

In the previous sections, the modal filter formulated by Equation 4.3 was applied to the solution variables in the channel flow. This filter is the same as that applied to the isotropic turbulence case in section 4.3 and removes high-frequency modes from all three directions equally. Since the channel flow is not an isotropic flow, we applied an anisotropic version of the modal filter to determine the sensitivity of the results to the direction of the filter. The anisotropic modal filter, given by Equation 4.4, removes the motions with contributions from the highest-frequency modes in only one direction. In this section, the anisotropic modal filter, with $N_f = 1$, is applied in three different directions for LES of the channel flow, and the results are compared with the isotropic filter as well as DNS and coarse DNS cases. The choice of $N_f = 1$ is due to its superior performance with the isotropic modal filter for the channel flow.
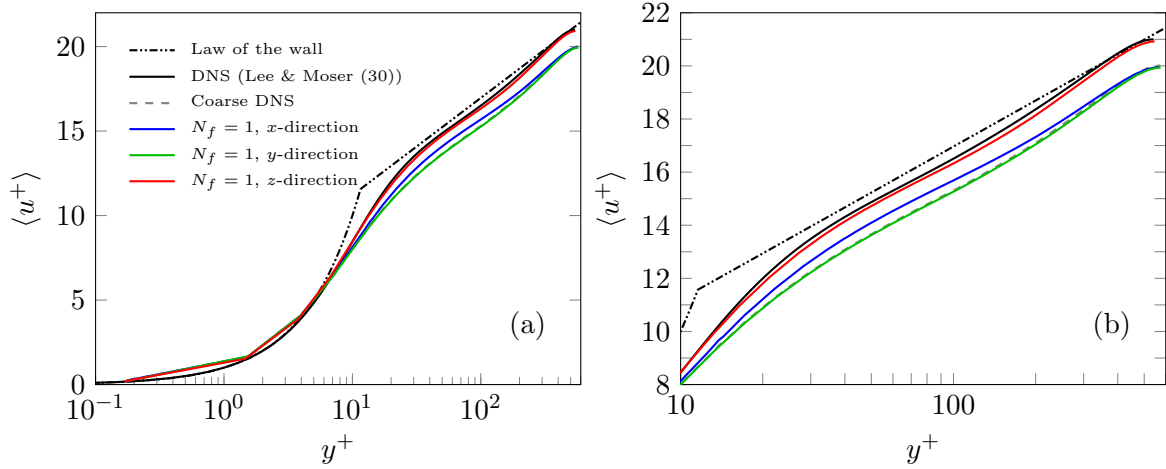
Figure 40. (a) Mean streamwise velocity for the LES of the channel flow using the modal filtering applied in different directions. (b) Same as (a), but magnified at the log-law region. The DNS of Lee and Moser (30) is used as the reference.

Figure 40 shows the mean streamwise velocity profiles of the LES of channel flow using the anisotropic modal filtering with $N_f = 1$ applied in the three directions. It is observed that applying the modal filter in the spanwise (z) direction provides the closest profile to DNS. Applying the filter in the streamwise (x) direction has a slight effect on the profile, and applying it in the wall-normal (y) direction has nearly no effect on the profile, i.e., the mean velocity is the same as the coarse DNS case.

The values of the friction Reynolds numbers for cases with the anisotropic modal filter are presented in Table VIII. Again, the prediction of the friction Reynolds number closest to the DNS result is provided by the anisotropic filter applied in the spanwise direction.

TABLE VIII

THE FRICTION REYNOLDS NUMBERS FOR THE NON-ISOTROPIC MODAL
FILTERING CASES AS COMPARED WITH DNS.

Case	Re_τ	Error
DNS	544	-
Anisotropic modal (x-direction)	571.0	4.95 %
Anisotropic modal (y-direction)	577.1	6.08 %
Anisotropic modal (z-direction)	547.9	0.72 %

The rms velocity fluctuations are shown in Figure 41. It is observed that applying the filter in the y-direction has nearly no effects on the velocity fluctuations in any direction. Applying the filter in the x-direction slightly improves the predictions of the spanwise and wall-normal fluctuations. However, applying the filter in the z-direction, i.e., removing one mode in the spanwise direction, noticeably improves the rms profiles in all three directions.

We also observed previously that the modal filtering in LES of the channel flow is most effective in accurate prediction of the mean velocity and the friction Reynolds number when one mode is removed from the spanwise direction. These observations are consistent with the fact that the motions in the spanwise direction contain more energy than the motions in the streamwise direction as demonstrated in Figure 42(a)-(c). This figure shows the one-dimensional energy spectra along two periodic directions based on the three components of the velocity. The 1D enegy spectra are defined as

$$E(k) = \frac{1}{\pi} \int_{-\infty}^{\infty} R(x)\, e^{-ikx}\, \mathrm{d}x, \tag{4.21}$$
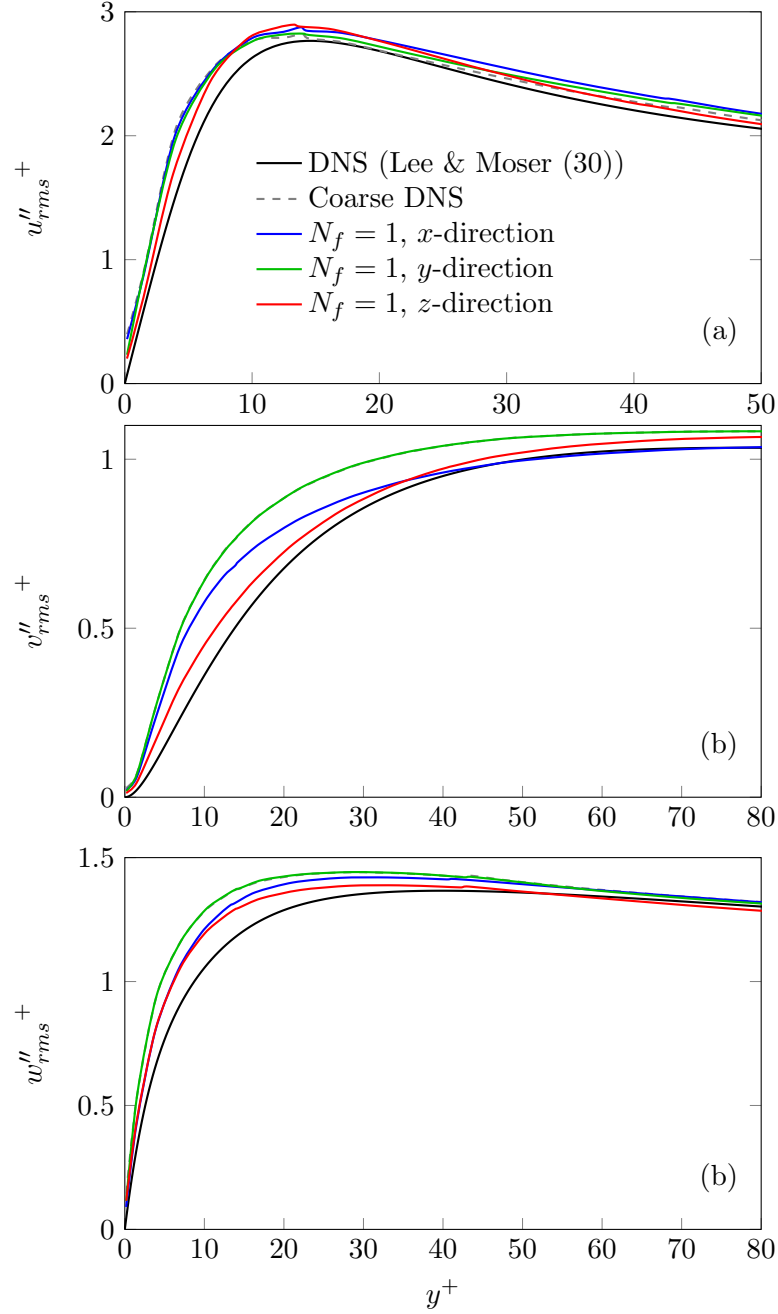
Figure 41. Rms fluctuations of the (a) streamwise, (b) wall-normal, and (c) spanwise velocity components for the LES of channel flow using the modal filtering applied in different directions, as compared with DNS and coarse DNS.

where $R(x)$ is the two-point correlation defined by

$$R(x) = \langle u(x_0, t)\, u(x_0 + x, t)\rangle. \tag{4.22}$$

The spectra in Figure 42 are measured at three different distances from the wall: near-wall region ($y^+ \approx 6$), midrange ($y^+ \approx 15$), and the core of the channel ($y^+ \approx 170$). It is observed that the spectra in the spanwise direction (solid curves) are higher than those in the streamwise direction (dashed curves), regardless of the distance from the wall or the component of the velocity. Therefore, there is a greater amount of energy in the spanwise direction that cascades to the higher-frequency motions and needs to be dissipated by the turbulence model at the cutoff wavenumber. This could contribute to the fact that removing the highest-frequency mode in the spanwise direction is more effective than it is in the streamwise direction. Note that the conclusion that filtering in the spanwise direction is the most effective among three directions is drawn merely for the periodic channel flow. Further investigation is needed to generalize this behavior for various near-wall flows.

We also examined and compared the amplitude of the highest-frequency modes in each direction. These quantities are defined by

$$\begin{cases} A_{q,x}(p) = \langle \hat{u}_{plm}\rangle & , \quad l = 0, \ldots, P\,, \quad m = 0, \ldots, P \\[2mm] A_{q,y}(p) = \langle \hat{u}_{kpm}\rangle & , \quad k = 0, \ldots, P\,, \quad m = 0, \ldots, P \\[2mm] A_{q,z}(p) = \langle \hat{u}_{klp}\rangle & , \quad k = 0, \ldots, P\,, \quad l = 0, \ldots, P \end{cases} \tag{4.23}$$
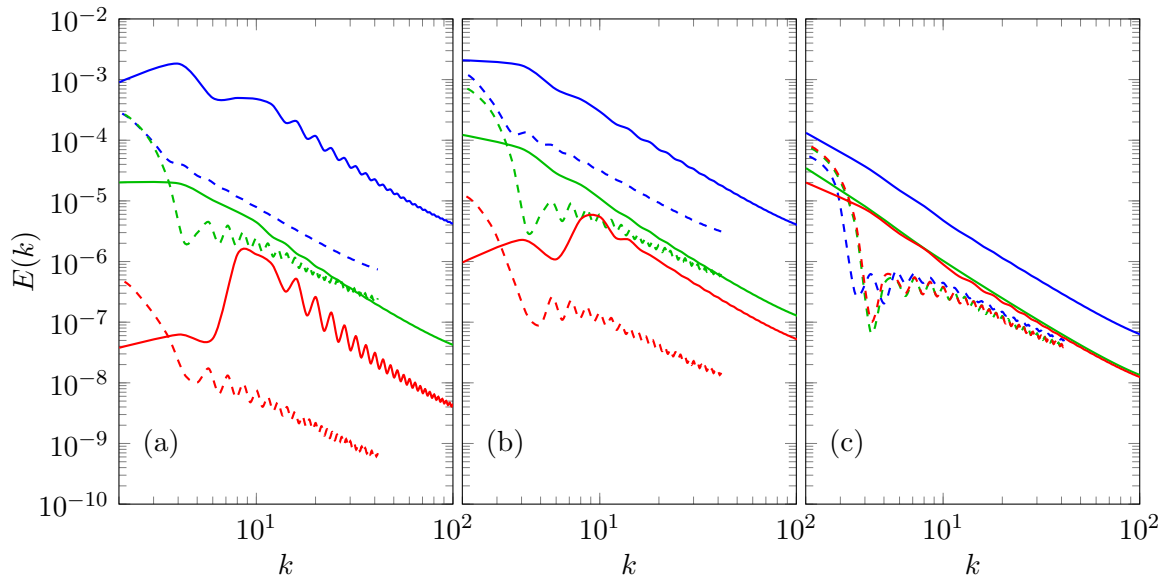
Figure 42. One-dimensional energy spectra for the coarse DNS of the channel flow based on the streamwise (blue), wall-normal (green), and spanwise (red) components of the velocity, along the periodic directions: streamwise (dashed) and spanwise (solid), at three distances from the wall: (a) $y^+ \approx 6$, (b) $y^+ \approx 15$, and (c) $y^+ \approx 170$.
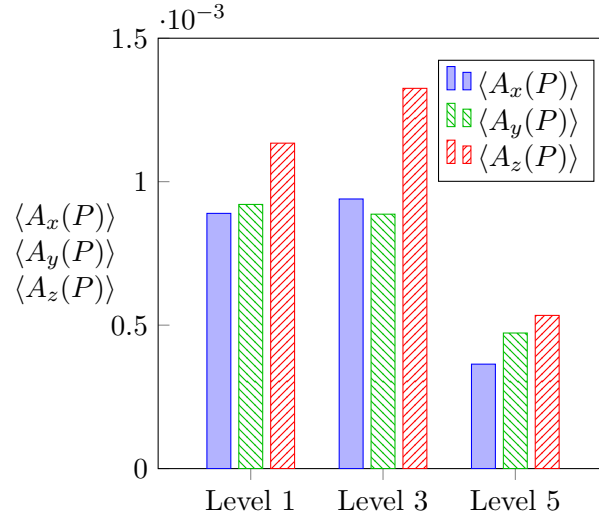
Figure 43. Magnitude of the highest-frequency modes in each direction. Lower level means elements closer to the wall, and higher level indicates elements farther from the wall.

for the highest-frequency modes in the x-, y-, and z-directions, respectively, in the element q. Again, we categorize the elements throughout the domain into three levels based on their distance from the wall.Then, we average the quantities defined in Equation 4.23 over the elements within the same level to obtain $\langle A_x(p) \rangle$, $\langle A_y(p) \rangle$, and $\langle A_z(p) \rangle$ at each level. The amplitude of the highest-frequency mode in each direction is shown in Figure 43 for three sample levels: 1, 3, and 5. It is observed that the amplitude of the highest-frequency modes is higher in the spanwise direction than it is in the other two directions. This is also identified as another reason why removing the highest-frequency modes in the spanwise direction is the most effective among three directions.

4.5   Computational Cost

The computational costs of the presented methods are quantified by running the same simulation using different models and measuring the run time. The LES of the isotropic turbulence is conducted for 10 time steps using the modal filter, series and 3D nodal filters, and the dynamic model. The run times are compared with a case without any turbulence model. Also, three polynomial orders of $P = 4$, 8, and 16 are considered to investigate the effect of P on the computational costs. The run times are averaged among 20 trials for each case. All simulations are performed using a single processor so that the results are not affected by the parallel efficiency of the code. Intel Xeon E5-2670 (2.60 GHz) processors are used.

Table IX presents the run times and the computational overheads for all cases as compared with the case with no model. The computational overheads are also depicted in Figure 44. It is observed that the modal filter is the least computationally costly method among presented models regardless of the polynomial order. It is also the only model whose computational cost reduces for higher polynomial orders, with an overhead of only 0.45% for $P = 12$. This could be attributed to the computational implementation; *FFTW* library, which is known as one of the fastest fast Fourier transform (FFT) libraries (76), is used to implement the transformation of the solution between nodal and modal representations. The dynamic model is the most computationally expensive choice; all filtering procedures are at least one order of magnitude less costly than the dynamic model. Also, the computational cost of the dynamic model does not have a meaningful dependence on the polynomial order. The series nodal filter has a constant overhead of roughly 4%, while the cost of the 3D nodal filter increases for higher polynomial

orders. The 3D nodal filter is less costly than the series version for the lower polynomial orders,

and it is more costly for higher orders.

TABLE IX

RUN TIMES (SECONDS PER TIME STEP) AND COMPUTATIONAL OVERHEADS FOR
THE LES OF THE ISOTROPIC TURBULENCE USING DIFFERENT POLYNOMIAL
ORDERS.

	P=4		P=8		P=12	
Case	Run time (s/time step)	Overhead (%)	Run time (s/time step)	Overhead (%)	Run time (s/time step)	Overhead (%)
No-model	0.875	-	4.85	-	14.73	-
Modal filter	0.898	2.55	4.94	1.93	14.80	0.45
Series nodal filter	0.910	3.93	5.04	4.01	15.35	4.18
3D nodal filter	0.900	2.85	5.01	3.40	15.49	5.12
Dynamic model	1.271	45.2	6.88	41.9	21.49	45.9

4.6   Summary and Conclusions

A modal low-pass filter is applied to a discontinuous spectral element method (DSEM), and

its performance is compared with two types of interpolation-based nodal filters, series and 3D,

and a dynamic Smagorinsky model for LES of turbulent flows with no additional SGS model.

An isotropic decaying turbulence and a periodic turbulent channel flow are used as the test

cases. The conclusions from the isotropic turbulence tests are as follows:
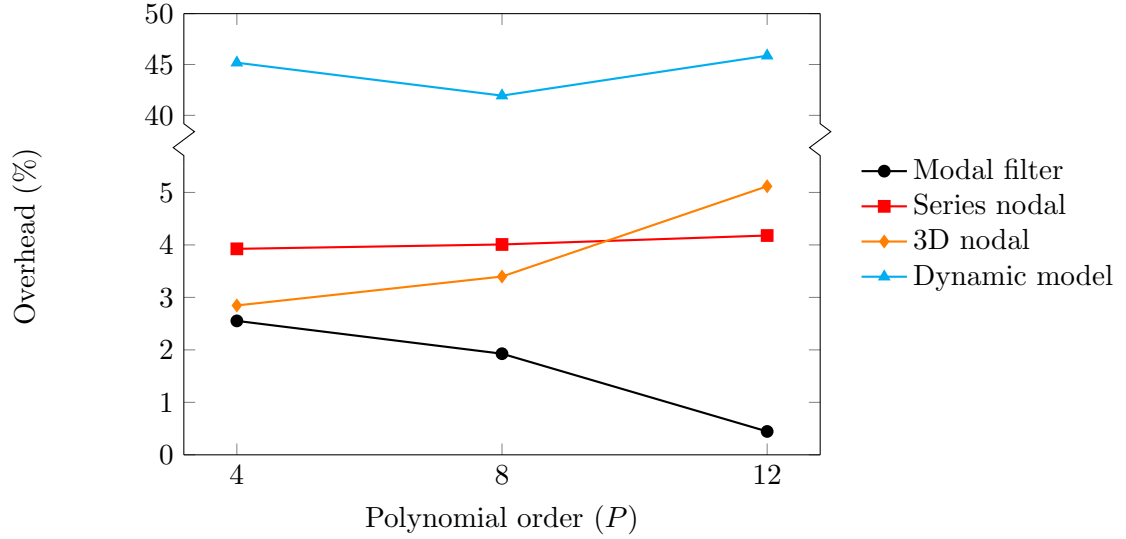
Figure 44. Computational cost overheads of the presented models for the isotropic turbulence case at different polynomial orders.

1. By removing the N_f highest-frequency modes using the modal filter, the solution becomes smoother step by step while increasing N_f, and the small-scale features are removed. However, by applying a nodal filter, especially for $N'_f > 2$, the shape of the function changes as well. The lower-frequency modes are also contaminated with nodal filters, except for the 3D nodal filter with $N'_f = 1$.

2. All filtering procedures provide better drop-off of the energy spectra at high wavenumbers compared with cases with no model. However, the nodal filters overpredict the spectra at the midrange and low wavenumbers. This overprediction is more severe in the series nodal filter than it is in the 3D version. Regardless of the filtering procedure, removing one mode provides the closest agreement with DNS.

3. The modal filter predicts the correct decay of the TKE for both $N_f = 1$ and 2. The series nodal filter underpredicts the rate of decay of turbulence regardless of N_f'. The 3D filter underpredicts the decay of TKE for $N_f' = 2$.

The modal filter provided more accurate statistics than the nodal filters in the isotropic turbulence tests. Therefore, this filtering procedure is chosen for further simulations. The modal filter, as well as an anisotropic version of the filter, is used in LES of a periodic turbulence flow. The conclusions are as follows:

1. The modal filtering procedure provides accurate statistics including the mean velocity, the friction Reynolds number, and velocity fluctuations, with respect to DNS.

2. The best choice of the filter strength (N_f) depends only on the polynomial order (P) and is independent of the h resolution. For a polynomial order of $P = 6$, a filter with $N_f = 1$ provides the best agreement with DNS, and for $P = 10$, the best results are obtained by $N_f = 3$, regardless of the grid resolution.

3. Applying a too strong filter results in an overprediction of the mean and fluctuations of the streamwise velocity and an underprediction of the friction Reynolds number and fluctuations of the wall-normal velocity. The opposite results are obtained by applying a too weak filter.

4. Removing the highest-frequency modes in the spanwise direction is the most effective among three directions and provides the closest predictions of the velocity profile and the rms velocity fluctuations to DNS results. This observation is attributed to (i) the fact that the one-dimensional energy spectra are higher in the spanwise direction than the

streamwise direction, and (ii) the fact that the amplitude of the highest-frequency mode is larger in the spanwise direction than the other two directions.

5. The frequency of the application of the filter does not affect the first- and second-order statistics as long as the cumulative strength of the filter is maintained; the cumulative strength of the filter is controlled by a function that updates the solution with a combination of the filtered and original values.

6. The amplitudes of the modes of the channel flow field decrease exponentially for successive modes from low-frequency to high-frequency regardless of the distance from the walls.

It is also observed that all filtering procedures are significantly less computationally expensive than the dynamic model, while the modal filter is the fastest model; The dynamic Smagorinsky model introduces a computational overhead of about 45%, while the other methods have less than 5% overhead. In general, the modal filter has shown good performance for both isotropic and wall-bounded flows; the calculated channel friction Reynolds number for the modal filter is within 0.26% error with respect to the DNS data, compared to 5.8% error for a case with no modeling.

CHAPTER 5

DIRECT NUMERICAL AND LARGE EDDY SIMULATIONS OF TURBULENT FLOW OVER BACKWARD-FACING STEP

5.1   Introduction

The flow over a backward-facing step (BFS) is a simple flow that can be used to evaluate the performance of turbulence models for separating and reattaching turbulent flows. In this chapter, LES of a 3D BFS configuration are conducted. The standard Smagorinsky model, with and without the addition of a newly developed wall sensor, are employed to evaluate their performance in simulating separating and reattaching flows. A direct numerical simulation (DNS) of turbulent flow over BFS is also performed and compared with previous work to validate our numerical method for such flow and also to provide a benchmark for LES simulations of the same problem. The conclusions that were obtained in chapter 3 regarding the near-wall resolution requirements for DNS of turbulent flows are employed in this chapter to produce the DNS grid for BFS.

The flow over a backward-facing step is regularly considered as a benchmark configuration for separating and reattaching flows. Dump combustors are also designed after such geometries. The flow dynamics in BFS can be described with the following stages. The boundary layer, which is formed near the wall before the step, separates from the bottom wall at the step corner. The flow then forms a free shear layer downstream of the step corner. The expansion of the free

shear layer downstream of the step creates a recirculation zone. The flow reattaches to the wall after the recirculation zone. An equilibrium boundary layer profile is recovered downstream of the reattachment.

5.2   Previous Work

The previous studies of the turbulent flow over BFS are surveyed in this sections. The previous works include experiments and numerical simulations.

5.2.1   Experiments

Starting with the pioneering experimental study by Eaton and Johnston (77), the BFS flow has been the subject of a significant quantity of experimental, theoretical, and numerical researches. Armaly *et al.* (78) experimentally studied the effect of Reynolds number on the reattachment length. The flow was shown to become 3D for Reynolds numbers (based on the inlet free stream velocity and step height) higher than 400. They revealed that with increasing the Reynolds number, the reattachment length increases for low Reynolds numbers ($Re <$ $1,200$). However, for moderate Reynolds numbers ($1,200 < Re < 6,600$) the reattachment length decreases with Reynolds number, and it remains relatively constant for high Reynolds numbers ($Re > 6,600$). Durst and Tropea (79) investigated the effect of expansion ratio on the reattachment length. The expansion ratio is defined as the ratio of the height of the post-expansion channel to that of the inlet section. The reattachment length is also affected by the flow conditions upstream of the step such as the ratio of the boundary layer thickness to the step height. The dependency of the reattachment length on the upstream boundary layer

profile was inspected by Adams *et al.* (80). Isomoto and Honami (81) considered the effect of the inlet turbulent intensity on the reattachment configuration.

5.2.2   <u>Numerical Simulations</u>

The flow over BFS has been the subject of numerous numerical studies as well during the past three decades. Early works mostly considered a two-dimensional description of the configuration. Kim and Moin (82) simulated a two-dimensional incompressible flow. The three-dimensionality of the flow for Reynolds numbers higher than $Re_c = 700$ was introduced by Kaikatis *et al.* (83) as the prime cause of the disagreement between the numerical results and the measurements. They also identified convective instabilities as the source of the unsteadiness of the flow (84). The first DNS of a three-dimensional flow over a BFS was carried out by Le *et al.* (85). The Reynolds number was $Re = 5,100$, and the expansion ratio was 1.2. They compared their results with the experiments of Jovic and Driver (86), which was conducted for the same geometry. They studied the unsteady characteristics of the flow such as the oscillation of the reattachment point as well as typical flow characteristics. The mean velocity and the Reynolds stresses agreed well with the Jovic and Driver measurements. They also calculated and analyzed the budgets of turbulent kinetic energy and Reynolds stresses. Wengle *et al.* (87) also simulated a moderate simulated BFS flow with a Reynolds number of $Re = 3,000$. In a later research, Barkley *et al.* (88) analyzed three-dimensional linear stability for a BFS geometry with an expansion ratio of 2.

5.3   DNS of Turbulent Flow Over BFS

In this section, the DNS of turbulent flow over a 3D BFS is presented. The results from this simulation will be used as the reference for the LES. The DNS of Le (89) and the experiment of Jovic & Driver (86) are used to validate the present DNS.

5.3.1   Problem Setup

A detailed description of the computational domain, the grid mesh generation, the flow conditions, and the flow initialization are included in this section.

5.3.1.1   Computational Domain

A schematic of the computational domain is shown in Figure 45. The flow enters the domain from the left using an inflow boundary condition. After passing over the step, which is located at the center of the domain in the streamwise direction, exits the domain from the right using an outflow boundary condition. Adiabatic walls are placed at the bottom of the domain as well as the vertical wall at the step. The free stream velocity is imposed at the top boundary of the domain. All the lengths are scaled by the step height, h. The length of the inlet section (upstream of the step), $L_{i,x}$, and the outlet section (downstream of the step), $L_{o,x}$, are both $20h$. Le (89) suggested that the inlet section should ideally be approximately $10h$, even though they used an inlet section of $10h$ due to computer resource restrictions. The height of the inlet section and the outlet section are $L_{i,y} = 5h$ and $L_{o,y} = 6h$, respectively. The depth of the domain in the spanwise direction is $L_z = 4h$. As shown in Figure 45, the streamwise direction, the normal direction, and the spanwise direction are called x-, y-, and z-directions, respectively.
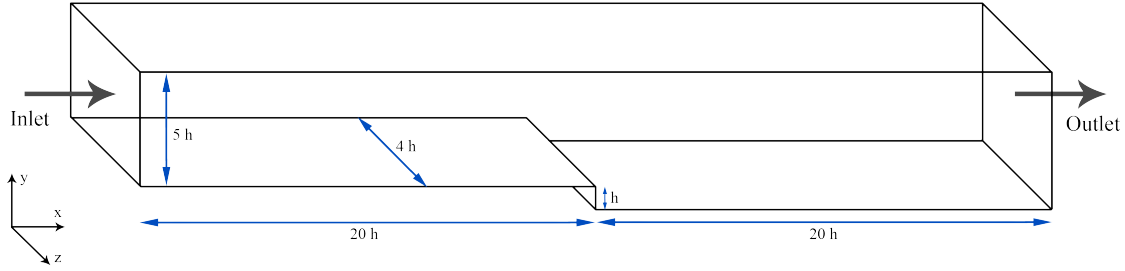
Figure 45. The computational domain used for BFS simulations.

The origin of the spatial coordinate system is fixed at the same streamwise location as the step, at the bottom wall and the minimum spanwise (z) location.

5.3.1.2   Grid Generation

The grid used for the DNS of BFS consists of $20,352$ elements. A 2D slice (normal to the z-direction) of the grid is shown in Figure 46. Note that in this figure, only the elements are shown. The approximation order inside each element is $P = 7$, which means there are $8^3 = 512$ solution points inside each element. This results in a total of $10,420,224$ solution points throughout the domain.

The grid is generated such that the resolution is high enough in the areas where higher resolution is needed, i.e., near the walls and the shear layer. The grid is coarsened elsewhere accordingly in order for the grid to be computationally efficient. The grid skeleton consists of three blocks, as shown in Figure 47. The number of elements in each direction for each of the three blocks are presented in Table X. Hyperbolic tangent functions are used to compress the
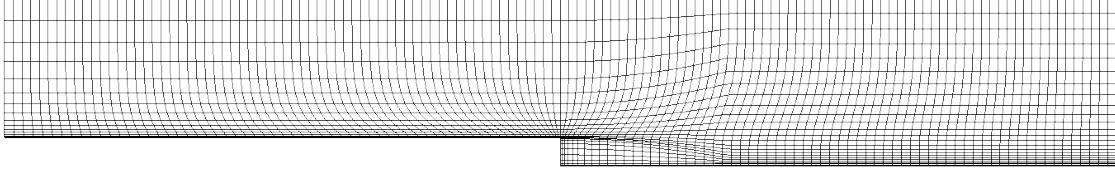
Figure 46. The grid used for the DNS of BFS. Only the elements are shown here.
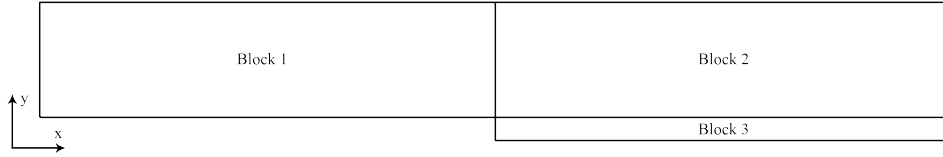
Figure 47. Three blocks used for the grid generation for DNS of BFS.

grid near the wall and in the shear layer area. The elements are uniformly distributed in the

z-direction.

In chapter 3, it was demonstrated for a polynomial order of $P = 7$, eight grid points within

below $y^+ = 10$ are needed for accurate flow statistics of the wall-bounded turbulent flows. In

the grid used for DNS of BFS, nine grid points are positioned within $y^+ = 10$ to ensure sufficient

near-wall resolution.

5.3.1.3   Flow Condition and Initialization

The flow conditions and parameters were chosen based on the DNS of Le (89) (hereinafter,

"Le94"), whose results are used to validate the present simulation. Their simulation was based

on the experiments of Jovic & Driver (86) (hereinafter, "JD"). The inlet mean velocity profile

TABLE X

NUMBER OF ELEMENTS IN EACH DIRECTION FOR THE THREE BLOCKS USED
FOR THE GRID OF DNS OF BFS.

Blcok	x-direction	y-direction	z-direction
1	64	15	8
2	66	15	8
3	66	9	8

is taken from Spalart's boundary layer (90) at the Reynolds number (based on momentum thickness) of $Re_\theta = 670$. The thickness of the inlet boundary layer is $\delta_{99} = 1.2h$, which is the same in Le94 and JD. The inflow free stream velocity and the step height are chosen as the reference velocity and the reference length. The Reynolds number based on the reference velocity and length is $Re = 5,100$. A stochastic model (91) is used to generate the inflow turbulence.

The streamwise velocity (x-direction) field is initialized with the inlet velocity profile. The normal (y-direction) and spanwise (z-direction) velocities are initialized as zero. The initial density is $\rho_0 = 1$, and the initial pressure is calculated from the ideal gas law.

5.3.2 Results

The simulation of the turbulent flow over the backward-facing step is started using a lower polynomial order in order to lower the computational cost; the flow is first simulated using the polynomial order of $P = 3$ for 15 flow-through times until the flow reaches a statistically stationary state. The flow-through time is defined as $t_{ft} = L_{o,x}/U_\infty$, where $L_{o,x}$ is streamwise
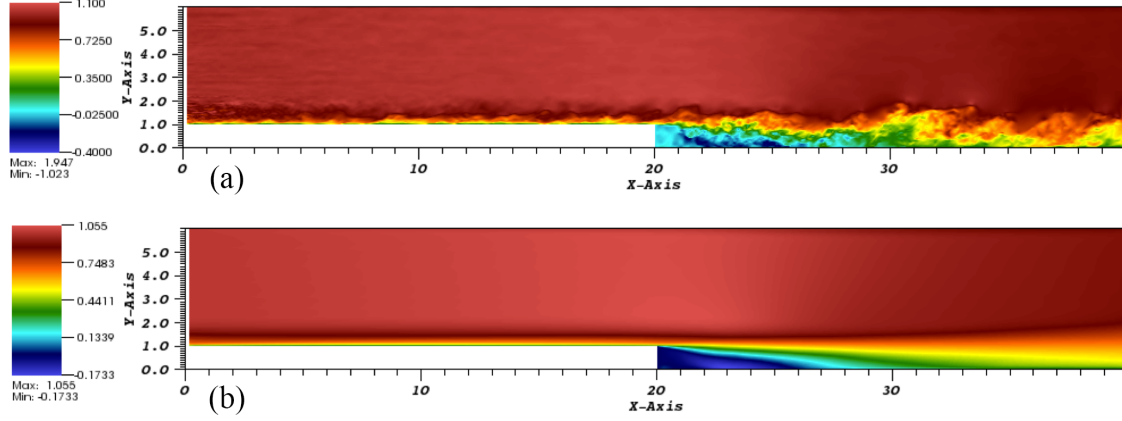
Figure 48. (a) Sample 2D slice of the instantaneous streamwise velocity and (b) average streamwise velocity for the DNS of BFS.

length from the step to the outlet boundary, and U_∞ is the free stream velocity. Then, the flow field is interpolated to a grid with a polynomial order of $P = 5$ using a spectral interpolation, simulated for another one flow-through time. Then, the flow is interpolated to a grid with the desired polynomial order of $P = 7$ and is simulated for another flow-through time. Then, the data is recorded for average statistics for 15 flow-through times. Finally, the rms statistics are recorded for 12 flow-through times. All average and rms data are averaged in time and the homogeneous direction (z). A sample 2D slice of the instantaneous streamwise velocity and average streamwise velocity are shown in Figure 48.

To assess the quality of the flow characteristics at the step, the rms velocity fluctuations are compared with previous DNS. Figure 49 compares the rms velocity profiles in three directions
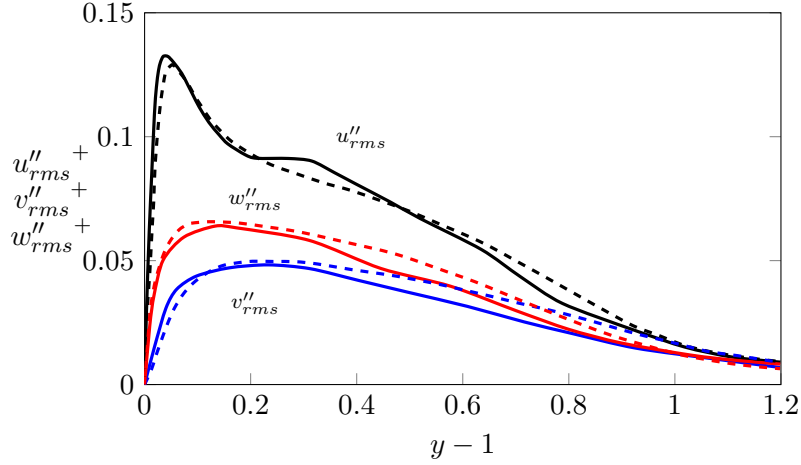
Figure 49. Rms velocity fluctuation profiles at the step ($x = 20$) of the present DNS (solid) as compared with DNS of Le (89) (dashed).

with previous DNS of Le94. The rms profiles are in good agreement with previous work. The slight differences may be alleviated by considering a longer inlet section.

In order to evaluate the adequacy of the grid resolution, one-dimensional energy spectra in the spanwise (z) direction are evaluated at different locations. The 1D energy spectra is defined by Equation 4.21. The locations of the probes used to calculate the energy spectra are shown in Figure 50. Three probes are located near the wall at streamwise locations: $x = -2.6$ (before the step), $x = 5$ (recirculation zone), and $x = 10$ (after reattachment). The distances from the wall are 0.039 before the step and 0.018 behind the step. Three other probes are also located away from the wall at a distance from the wall of $y = 1$ and three streamwise locations: $x = 5$, $x = 10$, and $x = 18$ (recovery region). The spectra for locations away from the wall are shown in Figure 51. The sufficient energy drop at high wavenumbers indicates adequate grid resolution.
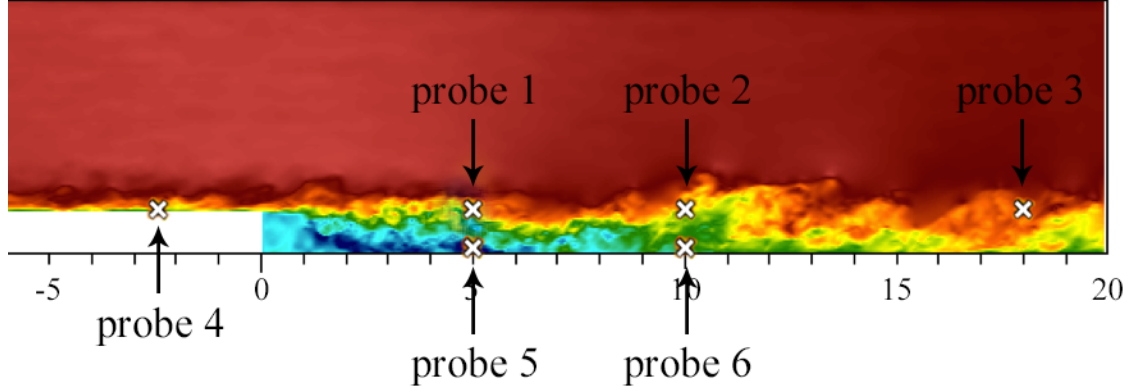
Figure 50. The location of the six probes used to evaluate the one-dimensional energy spectra for the DNS of BFS flow.

Shown in Figure 52 are the spectra for the locations near the wall. The sufficient energy drop is observed for E_{uu} and E_{ww}. The normal spectra, E_{vv}, suggest that higher spanwise resolution might be needed near the wall.

Examples of the two-point correlations of velocity components along the periodic direction (z) are presented in Figure 53 . The intent is to demonstrate that the computational domain is sufficiently large in the periodic direction to encompass the largest spatial scales of the flow. The correlations shown in this figure are from probes 1, 2, 4, and 5, which are shown in Figure 50. It is observed that all correlations fall below 5% for the largest separation, which means the quantities are decorrelated at this distance.
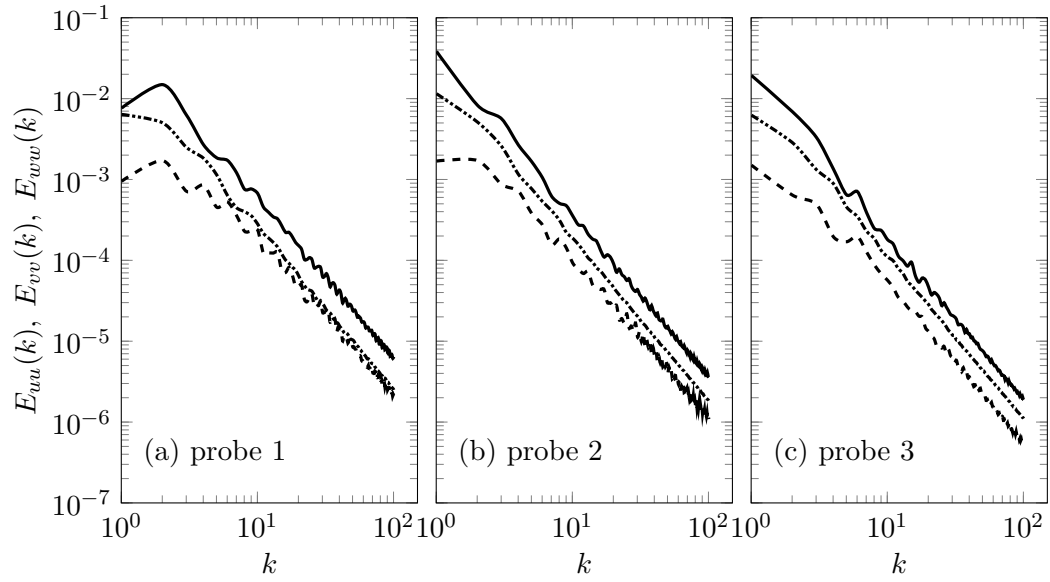
Figure 51. One-dimensional energy spectra for the DNS of the BFS based on the streamwise (solid), normal (dashed), and spanwise (dash-dotted) components of the velocity, along the periodic (z) direction at three probes away from the wall. The location of the probes are shown in Figure 50.
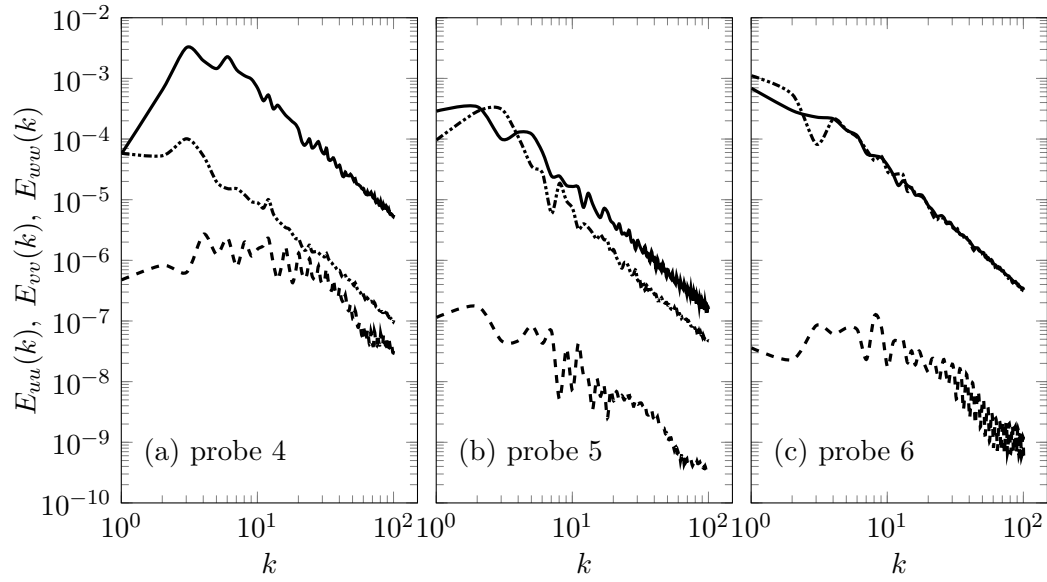
Figure 52. One-dimensional energy spectra for the DNS of the BFS based on the streamwise (solid), normal (dashed), and spanwise (dash-dotted) components of the velocity, along the periodic (z) direction at three probes near the wall. The location of the probes are shown in Figure 50.
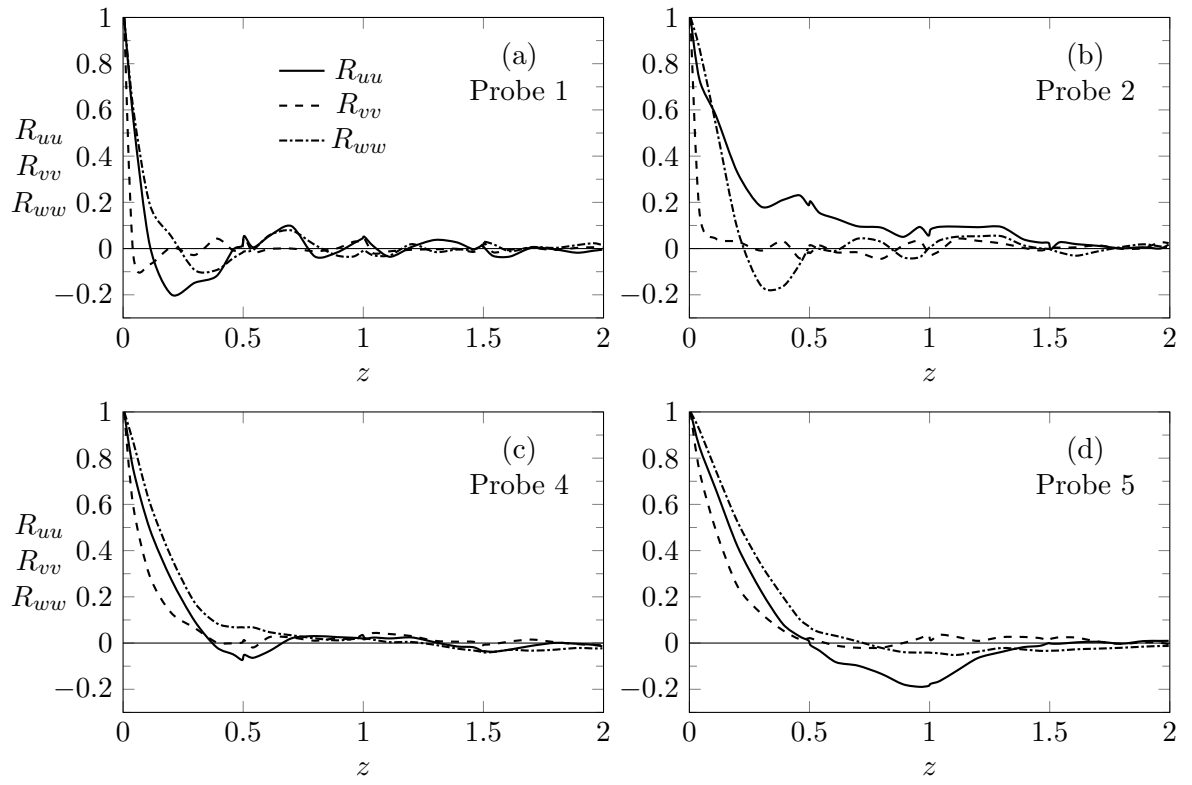
Figure 53. Two-point correlations of the velocity components along the periodic direction at probes 1, 2, 4, and 5, which are shown in Figure 50.

5.3.2.1   Average Statistics

One of the most important characteristics of a BFS flow is the reattachment length, which is the streamwise (x) distance between the step and the reattachment point on the bottom wall. The reattachment point is defined as the point at which the near-wall velocity is zero, i.e., the point where the streamline that separates the recirculation zone from the rest of the domain attaches to the wall. Different techniques are usually employed to detect the reattachment point. Here, we determine the reattachment point by finding the point where the slope of the velocity profile ($\partial u/\partial y$) is zero at the wall. The value of the reattachment length for the present DNS of BFS is measured as $L_r = 6.34$. This value is in a good agreement with previous DNS of Le (89), $L_r = 6.28$ (0.9% error).

Figure 54 presents the average velocity profiles at different streamwise (x) locations. The results are compared with previous works: DNS of Le (89), the experiment of Jovic & Driver (86), and LES of Sengupta (59). The velocity profiles of the present DNS generally agree with previous works at all three streamwise locations. It is observed that the present DNS, as well as the LES of Sengupta, have higher values of streamwise velocity in $1 < y < 2$ than DNS of Le94 and experiment of JD. This difference can be attributed to the compressibility effects. Both the present study and the LES study are performed using compressible flows, while the other two deal with incompressible flows. The same behavior, the streamwise velocity exceeding the free stream velocity around the height of the step, is also observed in Figure 2 of Liu *et al.* (92); they present the results of LES of compressible flow over BFS.
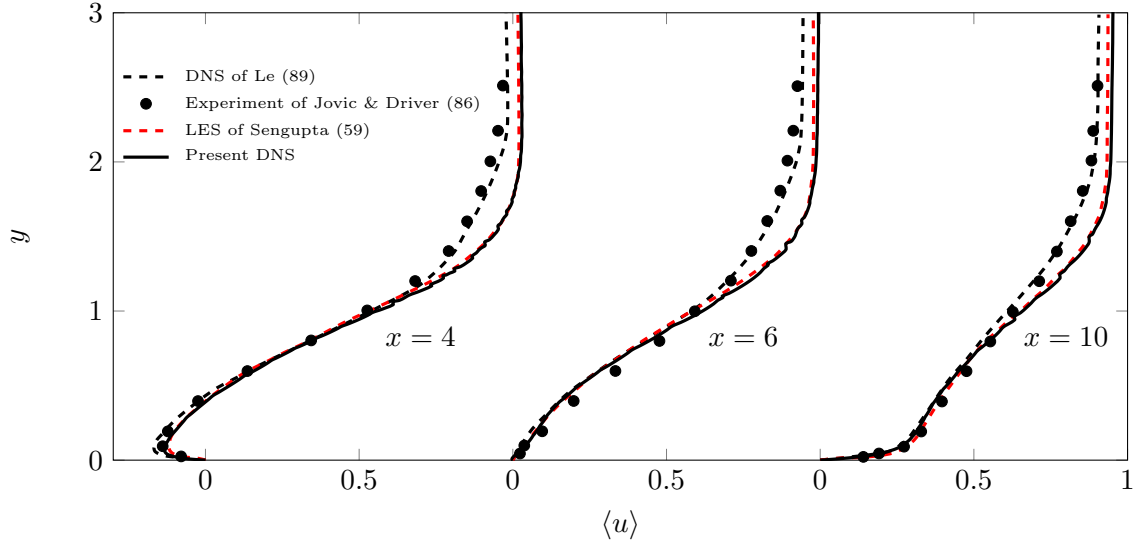
Figure 54. The average velocity profiles at different streamwise (x) locations, as acompared with previous works: DNS of Le (89), Experiment of Jovic & Driver (86), and LES of Sengupta (59).

5.3.2.2   RMS Statistics

The profiles of the rms velocity fluctuation in the streamwise (x) and normal (y) directions at different streamwise (x) locations are presented in Figure 55 and Figure 56, respectively. The results are compared with previous works: DNS of Le (89) and experiment of Jovic & Driver (86). The rms profiles of the present DNS are in good agreement with previous DNS and experiment at all three streamwise locations.

The Reynolds shear stress profiles, $\{u''v''\}$, are shown in Figure 57 and are compared with previous works: DNS of Le (89) and experiment of Jovic & Driver (86). The Reynolds shear stress profiles are also in good agreement with previous works.
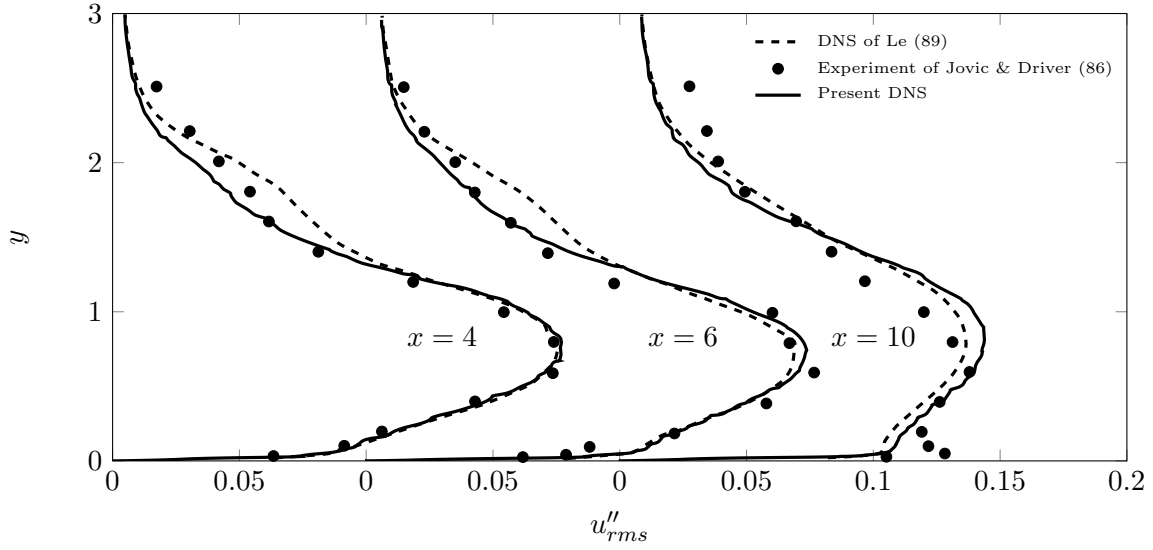
Figure 55. The streamwise (x) rms velocity fluctuations at different streamwise (x) locations, as acompared with previous works: DNS of Le (89) and Experiment of Jovic & Driver (86).
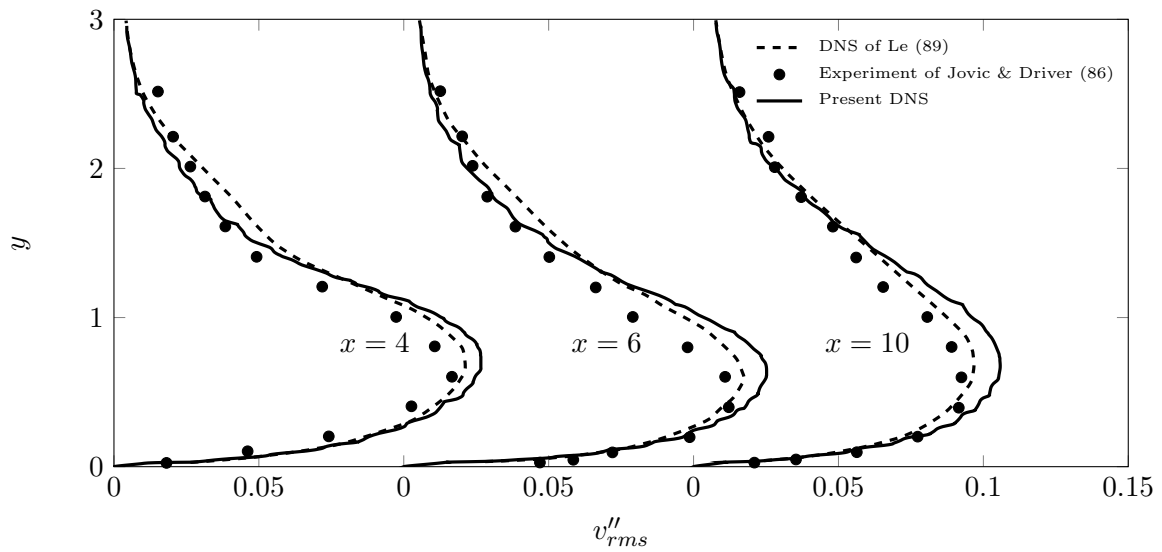
Figure 56. The normal (y) rms velocity fluctuations at different streamwise (x) locations, as acompared with previous works: DNS of Le (89) and Experiment of Jovic & Driver (86).
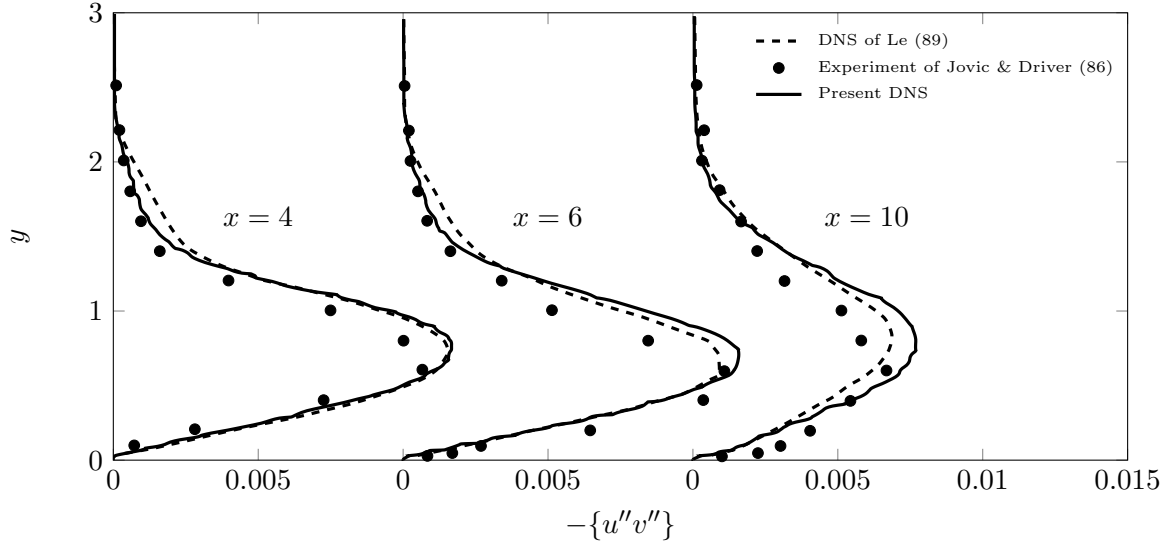
Figure 57. Reynolds shear stress profiles at different streamwise (x) locations, as acompared with previous works: DNS of Le (89) and Experiment of Jovic & Driver (86).

5.4 LES of Turbulent Flow Over BFS

In this section, the LES of turbulent flow over BFS is reported. A wall sensor is developed, implemented, and tested for Smagorinsky model. The results for the cases with and without the addition of the sensor are presented and compared.

5.4.1 Background

A turbulence model should ideally perform well in all regions of the flow over a BFS. The ideal turbulence model should represent an accurate boundary layer upstream of the step by predicting a correct mean profile and turbulence intensity; it should also provide accurate prediction of the growth rate of the shear layer that originates at the step corner; it should

also provide a good estimation of the location where the flow reattaches to the bottom wall downstream of the step.

Smagorinsky eddy-viscosity model (48) is one of the best-known turbulence models and the most commonly used eddy-viscosity models (For a detailed description, see (93)). It is based on the assumption that the effects of the small-scale unresolved motions of the flow can be modeled by means of artificial viscosity. This artificial viscosity is calculated as a function of the derivatives of the velocity field and the local grid size in the Smagorinsky model. The prescription for the eddy viscosity is

$$\nu_t = (C_s \Delta_G)^2 \sqrt{2\overline{S}_{ij}\overline{S}_{ij}}, \tag{5.1}$$

where C_s is the Smagorinsky constant, $\overline{S}_{ij}$ is the filtered rate of strain, and Δ_G is a length scale, representing the average distance between solution points in each element. We calculate this average spacing by

$$\Delta_G = \frac{J^{1/3}}{\left(\prod_{i=1}^{3} n_{g,i}\right)^{1/3}}, \tag{5.2}$$

where J is the determinant of the Jacobian of the element and $n_{g,i}$ is the number of (Gauss) solution points in the ith direction within the element. The attractions of the Smagorinsky model are its computational stability and its ease of application in numerical codes; the eddy-viscosity is calculated using only local information, and the procedure does not involve extensive computations; therefore, the model is not computationally expensive.

The advantages of Smagorinsky model make it a valuable tool for engineering problems (94). However, while the model provides acceptable results in LES of isotropic and homogeneous flows with $C_s \approx 0.17$, recommended by Lilly (95), it does not perform as well in LES of wall-bounded flows (96). The large value of the mean shear adjacent to the wall results in an excessive amount of eddy viscosity, which results in over-dissipating the flow. Furthermore, the model predicts non-zero eddy viscosity in laminar-flow regions. This non-zero viscosity dampens the small perturbations and therefore suppresses the transition to turbulence (97).

To reduce the effects of the above-mentioned flaw in the Smagorinsky model, the Smagorinsky constant is often multiplied by a damping factor, which is a function of distance to the wall (98). Even though the damping factor helps improve the performance of the method in some cases, the determination of the damping factor is arbitrary and problem dependent. Moreover, even though the determination of the damping factor seems straightforward for a plane wall, it is not trivial for a curved wall or sharp corners. Therefore, a more robust and dynamic improvement to the Smagorinsky model is desired.

The dynamic SGS model aims to improve the Smagorinsky model by dynamically calculating the Smagorinsky constant (49) and eliminating the need for manually tuning the value of C_s. In this model, the evaluation of the coefficient, C_S, is based on the Germano identity (99) and provides a dynamic value for $C_s(x,t)$, which is a function of space and time. The value of the coefficient ideally approaches zero near the wall (100). The dynamic SGS model certainly improves the performance and capability of the standard Smagorinsky model. However, the dynamic Smagorinsky model is accompanied with limitations such as numerical stability issues

and computational cost. Therefore, it is desired to seek a compromise between the accuracy of the dynamic SGS model and simplicity and manageability of the standard Smagorinsky model for wall-bounded turbulent flows.

5.4.2 Density-based Turbulence Wall Sensor

Our preliminary tests with LES of turbulent flow over a BFS using the standard Smagorinsky model demonstrated that the turbulent eddy viscosity in the inlet channel, especially within the boundary layer, notably affects the turbulence statistics and results in significantly dissipated turbulence after the step. Therefore, a density-based sensor is developed, which is multiplied by the turbulent viscosity and reduces the amount of the turbulent viscosity inside the boundary layer. The first version of the sensor, θ_1, is based on the gradient of the density and is defined as

$$\theta_1 = \frac{|\nabla \rho|}{|\nabla \rho| + 1},$$ (5.3)

where $\nabla \rho$ is the gradient of the density. The value of this sensor is zero where there is no density gradient (regions with no turbulence) and approaches unity where the magnitude of the density gradient is high (regions with strong turbulence). Although the first version of the sensor significantly removes the undesired viscosity from areas with weak or no turbulence, it still generates viscosity inside the inlet boundary layer due to the large value of the mean shear adjacent to the wall and results in dissipated turbulence. Therefore, we modified the formulation to obtain the second version of the sensor (101).

The idea behind designing the second version of the wall sensor is the fact that turbulence is by nature a three-dimensional phenomenon. Therefore, the sensor is designed such that it

adds viscosity only where the gradient of density is large in at least two out of three Cartesian coordinate directions. Inside the boundary layer, the density varies mostly in one direction (normal to the wall); therefore, this sensor reduces the amount of the added viscosity in those areas. The value of this sensor is zero where there is no density gradient and approaches unity where the magnitude of the density gradient is large in all three directions. The modified sensor, θ_2, is defined by

$$\theta_2 = C_\theta \sqrt{\frac{1/3}{\dfrac{1}{\rho_x^2 + \epsilon} + \dfrac{1}{\rho_y^2 + \epsilon} + 1} + \frac{1/3}{\dfrac{1}{\rho_x^2 + \epsilon} + \dfrac{1}{\rho_z^2 + \epsilon} + 1} + \frac{1/3}{\dfrac{1}{\rho_y^2 + \epsilon} + \dfrac{1}{\rho_z^2 + \epsilon} + 1}}, \qquad (5.4)$$

where C_θ is the sensor coefficient that is tunable. In Equation 5.4, ρ_x, ρ_y, and ρ_z are the gradients of the density in x, y, and z directions, and ϵ is a small positive real number chosen to avoid numerical divergence. The three terms inside the square-root are designed to serve the purpose of the sensor. In the areas where there are no significant density gradients (laminar areas) and in the areas where the density gradient is large in only one direction (boundary layer), all three fraction terms, and consequently the value of the sensor, approach zero, resulting in nearly zero eddy viscosity introduced by the turbulence model. On the other hand, in the areas where the density gradient is large in two or three directions (turbulent areas), one or three of the fraction terms, respectively, gain non-zero values, resulting in non-zero values of the sensor, therefore, introducing the eddy viscosity by the turbulence model.
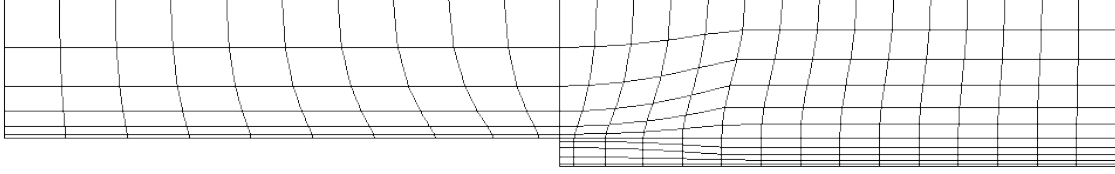
Figure 58. The grid used for the LES of BFS. Only the elements are shown here.

5.4.3   Problem Setup

In this section, the problem setup for LES of BFS is described. The computational domain used for LES is the same as the one used for DNS in section 5.3 and is shown in Figure 45.

The same meshing strategy as used for the DNS grid is used to generate the grid for LES. Also, the same polynomial order of $P = 7$ is used; however, the number of elements is reduced in all three directions. A 2D slice (normal to the z-direction) of the grid is shown in Figure 58. Note that in this figure, only the elements are shown. The total number of elements in the LES grid is 1,350 (compared to 20,352 elements for DNS). The total number of solution (Gauss) points for the LES case is $1{,}350 \times 8^3 = 691{,}200$ (compared to $10{,}420{,}224$ for DNS). The number of elements in each direction for each of the three blocks (shown in Figure 47) are presented in Table XI.

The flow conditions and parameters, the initial conditions, and the boundary conditions for the LES case are all similar to those of the DNS case.

TABLE XI

NUMBER OF ELEMENTS IN EACH DIRECTION FOR THE THREE BLOCKS (SHOWN IN Figure 47) USED FOR THE GRID OF LES OF BFS.

Blcok	x-direction	y-direction	z-direction
1	10	6	6
2	15	6	6
3	15	5	6

5.4.4   Results

The primary objective of the present simulations is to assess the performance of the wall sensor. The standard Smagorinsky model, both with and without applying the wall sensor, are considered, and first- and second-order statistics are compared to validate the effect of the wall sensor. The value of the Smagorinsky constant is set to $C_s = 0.15$ in all simulations in this chapter. The sensor coefficient is also set to $C_\theta = 20$ for all simulations except those presented in section 5.4.4.3, where we study the effect of the sensor coefficient. Each case is first simulated for 3 flow-through times before calculating the average statistics to make sure the interpolation effects on the flow are disappeared. Then, the simulation is continued for 6 flow-through times for average statistics, and then 12 flow-through times for rms statistics. All average and rms data are averaged in time and the homogeneous direction (z).

5.4.4.1   Mean Statistics

Figure 59 and Figure 60 compare the mean streamwise (u) and normal (v) velocity profiles at different streamwise locations for the LES with Smagorinsky model with and without applying

the wall sensor. The results are compared with those of the DNS case at three streamwise locations of $\tilde{x} = 4$, 6, and 10, where

$$\tilde{x} = x \, \frac{(L_r)_{\text{DNS}}}{L_r} = x \, \frac{6.34}{L_r}, \tag{5.5}$$

where L_r is the reattachment length. The locations of the velocity profiles are scaled with the reattachment lengths so that the differences in the reattachment lengths between different cases do not affect the comparison of the velocity profiles. It is observed that the case with the wall sensor provides significantly more accurate mean velocity profiles as compared with the DNS case for both streamwise and normal velocities. This improvement is more visible at $\tilde{x} = 4$ and 10 for the streamwise velocity and $\tilde{x} = 4$ and 6 for the normal velocity.

The reattachment length is one of the most important characteristics of the BFS flow and is often used to evaluate the accuracy of the simulations. The calculated reattachment length for the case with Smagorinsky model is $L_r = 7.51$. The simulation with Smagorinsky model overpredicts the quantity; it has 18.4% error from the value of DNS case ($L_r = 6.34$). The excess amount of eddy viscosity in the inlet section boundary layer prevents the turbulence from developing naturally, and results in weak turbulence downstream of the step. The weak turbulence inhibits the instabilities in the shear layer that is formed behind the step and delays the growth of the shear layer, and the delayed shear layer results in a longer reattachment length. The case that features the wall sensor, however, allows the turbulence to grow naturally and provides a shorter reattachment length of $L_r = 6.30$, which has only -0.5% error from DNS.
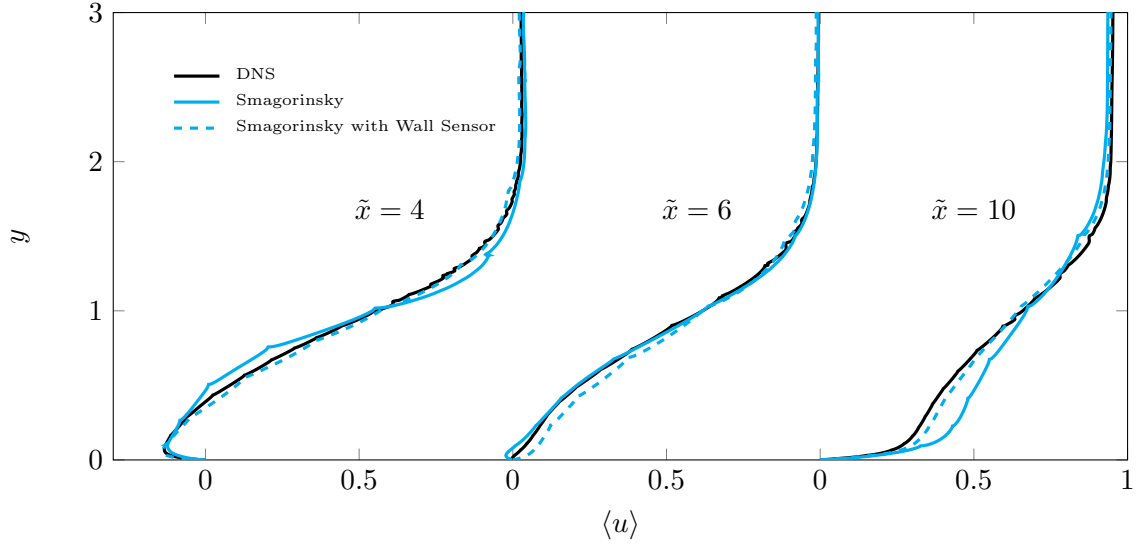
Figure 59. The average streamwise velocity (u) profiles at different streamwise (x) locations for the Smagorinsky case with and without the wall sensor, as compared with DNS.
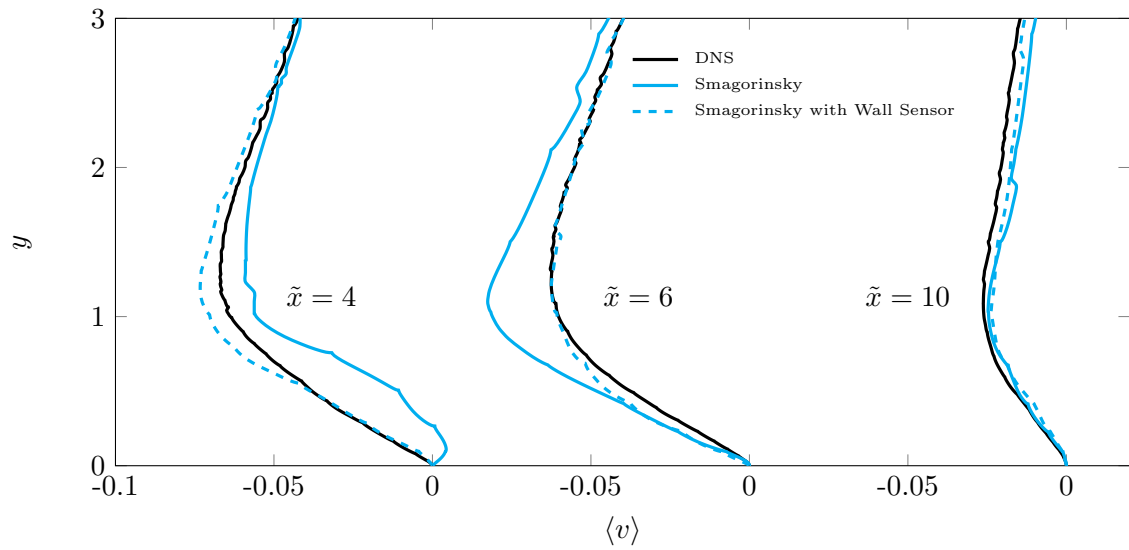
Figure 60. The average normal velocity (v) profiles at different streamwise (x) locations for the Smagorinsky case with and without the wall sensor, as compared with DNS.

It is observed from both velocity profiles and the reattachment length that the addition of the wall sensor significantly improves the mean statistics of the flow.

5.4.4.2   RMS Statistics

Figure 61 presents the rms velocity fluctuations, as well as the turbulence intensities, at the step for the Smagorinsky case with and without applying the wall sensor. The profiles are compared with those of the DNS case. It is observed that the case with Smagorinky model without the sensor significantly underpredicts the values of rms fluctuations as well as the turbulence intensity. The excess amount of eddy viscosity introduced by Smagorinsky model in the boundary layer of the inlet section suppresses the development of turbulence and results in a highly diffused flow, which is visible in the values of the rms fluctuations and the turbulence intensity at the step. With the addition of the wall sensor, the excess artificial viscosity is removed from the inlet boundary layer, the turbulence is therefore developed in a natural rate, and the rms profiles are comparable with those of DNS, as seen in Figure 61.

The same behavior is observed for rms velocity fluctuations behind the step. Figure 62 shows the streamwise rms velocity fluctuations (u''_{rms}) at different scaled streamwise locations ($\tilde{x} = 4$, 6, and 10) for both cases with and without the wall sensor. The results are compared with DNS. Again, the case without the wall sensor underpredicts the fluctuations due to the over-diffused flow. The case with the wall sensor, however, predicts fluctuations close to those of DNS.
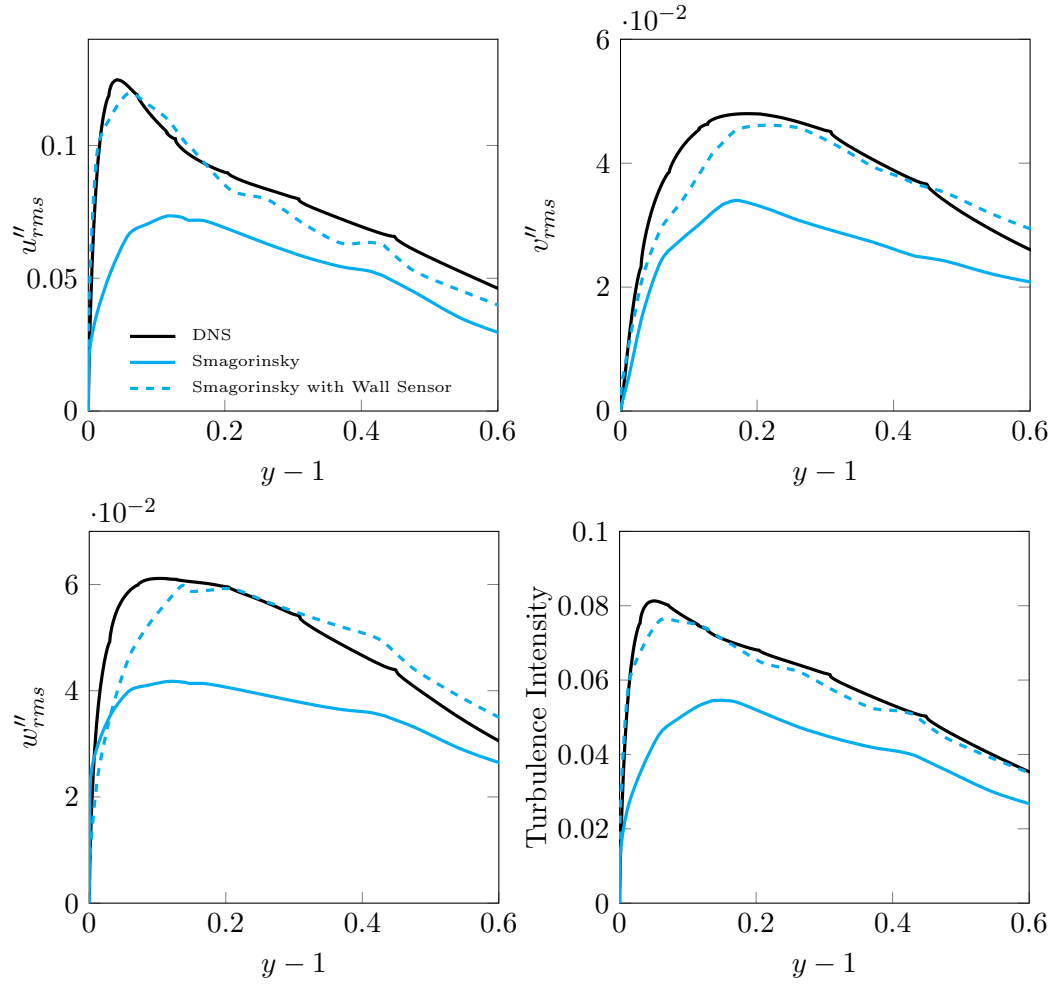
Figure 61. Rms velocity fluctuation profiles at the step ($x = 20$) for the LES with Smagorinsky model with and without applying the wall sensor as compared with DNS.
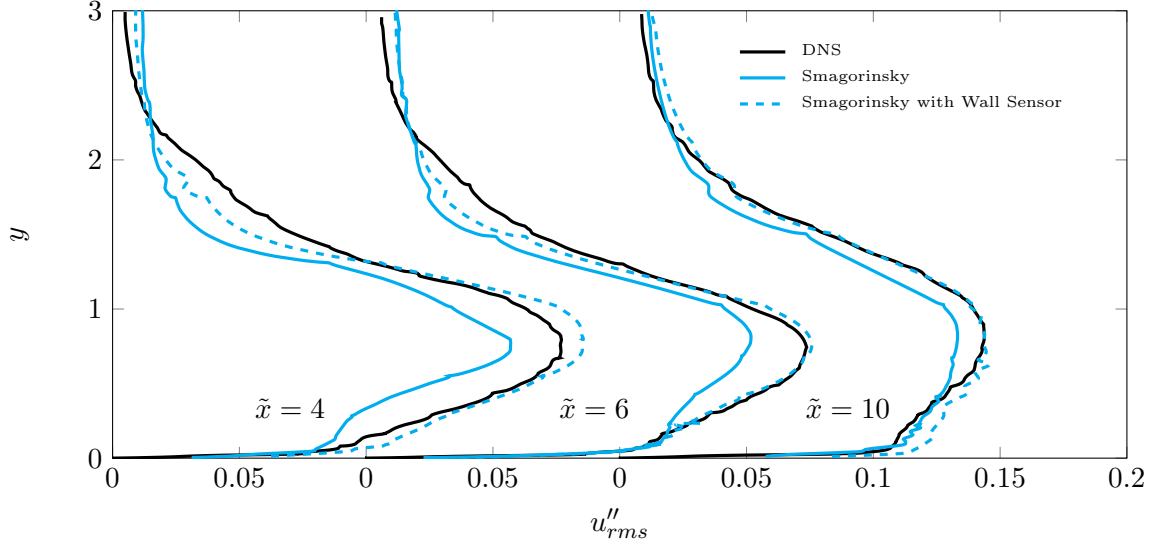
Figure 62. The streamwise (x) rms velocity fluctuations at different streamwise (x) locations for cases with and without the wall sensor, as acompared with DNS.

5.4.4.3   Sensitivity of the Wall Sensor

The sensor coefficient, C_θ in Equation 5.4, tunes the value of the sensor that is multiplied by the eddy viscosity suggested by the Smagorinsky model. We have studied the sensitivity of the performance of the wall sensor to its coefficient. In the previous simulations, the value of the coefficient was set to $C_\theta = 20$. Here, we repeated the same simulation with two other values of the coefficient: $C_\theta = 10$ and 40. Table XII compares the reattachment lengths for all LES cases as compared with DNS. The values are also depicted in Figure 63 for better comparison. It is observed that while the Smagorinsky model has a large error in the prediction of the reattachment length, all cases that feature the wall sensor provide close values to that of DNS

regardless of the value of C_θ. It is, therefore, concluded that the performance of the wall sensor has little dependency on the value of its coefficient for the BFS flow.

TABLE XII

THE REATTACHMENT LENGTHS, L_R, FOR CASES WITH DIFFERENT VALUES OF THE SENSOR COEFFICIENT, C_θ, AS COMPARED WITH THE LES CASE WITHOUT THE SENSOR AND DNS.

Case	C_θ	L_r	Error
DNS	-	6.34	-
Smagorinsky	-	7.51	18.4 %
Smagorinsky with Wall Sensor	10	6.27	-1.09 %
Smagorinsky with Wall Sensor	20	6.30	-0.5 %
Smagorinsky with Wall Sensor	40	6.24	-1.45 %

5.5 Summary and Conclusions

A density-based sensor is developed, implemented and tested for LES of wall-bounded turbulent flows using the standard Smagorinsky model. The sensor reduces the amount of the undesired eddy viscosity inside the boundary layer that is introduced by the Smagorinsky model. The excessive eddy viscosity is often problematic because it inhibits the disturbances that lead to the development of turbulence. The use of the sensor is tested for a turbulent flow over a backward-facing step. A DNS of the same configuration is also performed to serve as the reference for the LES cases. It is observed that the addition of the sensor significantly improves the mean and rms flow statistics. In fact, by applying the wall sensor, the error of
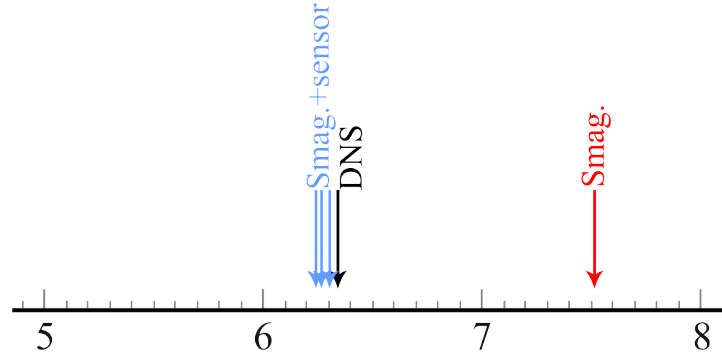
Figure 63. The reattachment lengths for cases with different values of the sensor coefficient as compared with the LES case without the sensor and DNS.

the calculation of the reattachment length reduces from 18.4% to 0.5%. It is also showed that the performance of the wall sensor is not sensitive to the value of its tunable coefficient.

CHAPTER 6

LARGE EDDY SIMULATION OF SUPERSONIC TURBULENT FLOW

OVER RAMP-CAVITY

The flow inside the combustion chamber of a high-speed combustor is a prime example of a

multi-physics and multi-scale flow, which is usually associated with the simultaneous existence of

turbulence and shock waves. In this chapter, the DSEM is employed to simulate the supersonic

non-reactive flow inside a 3D ramp-cavity combustor at a Mach number of $M = 2$ (102; 103; 12).

An entropy viscosity method is employed to capture the shocks, and the standard Smagorinsky-

Lilly model is used as the turbulence model. Results are presented for two simulations with

and without an injector and the results are compared. The effect of the Reynolds number is

also demonstrated.

6.1 Introduction

Designing stable and efficient high-speed engines requires a deep understanding of the

physics of the reacting flow within the supersonic combustor. In recent years, a variety of

injection and flameholding concepts have been studied experimentally, such as the use of in-

jector arrays (104; 105), struts or pylons (106), wall cavities (107; 108; 109), and combinations of these strategies (110). In this work, the focus will be on the numerical simulation of the supersonic non-reactive flow within a cavity flame holder with a nozzle attached to the ramped face of the cavity. The nozzle functions as the fuel injector in the actual combustion application.

The main challenge in supersonic turbulent flow simulations arises from the contradictory properties of numerical methods designed to treat shocks and turbulence, where the numerical scheme needs to satisfy two competing requirements. These requirements are capturing different types of discontinuities and simultaneously resolving the broadband scales of turbulence. The shock capturing is usually achieved through the addition of dissipation to the flow at the location of the shock in order to smear them sufficiently such that they can be represented on the numerical stencil. However, the use of a shock-capturing scheme can significantly affect the fidelity of the solution. A poorly designed shock capturing method can be over-dissipative and smear the solution, excessively dissipate turbulence, and thus lead to an inaccurate representation of the flow discontinuities and turbulence. One of the objectives of the present research is to provide an effective and accurate shock capturing method using high-order numerical methods. The method should be capable of locating strong shocks and capturing them within the numerical stencil as well as resolving a wide range of turbulence time and length scales.

A variety of shock capturing methods have been employed by various researchers, including employing limiters (111), using schemes such as essentially non-oscillatory (ENO) and weighted essentially non-oscillatory (WENO) schemes(112; 113), and applying artificial viscosity in the shock regions. All of mentioned methods operate based on smoothing the solution in the region

of shock while attempting to remove any Gibbs oscillations. This work explores the feasibility of the entropy viscosity (EV) method (114) as a shock capturing tool in simulation of supersonic turbulent flows in ramp-cavity combustors using a discontinuous high-order numerical method. We apply a modified formulation of the entropy viscosity method for turbulent flows that was proposed by Abbassi *et al.* (6). Using this methodology, we are able to extend the use of the entropy viscosity to high Reynolds number turbulent flows and other flows with strong physical fluctuations.

In the following section, the turbulence model and the shock capturing method will be discussed. Next, the results are presented for two cases, with and without an injector attached to the cavity. The approach taken to locally refine the grid near the injector is also explained. Finally, concluding remarks are provided.

6.2 Formulation and Methodology

6.2.1 Turbulence Modeling

All the simulations presented in this chapter use the standard Smagorinsky-Lilly turbulence model (48). The subgrid model introduces a turbulent viscosity that is similar to the entropy viscosity and is described in 5.4.1. The wall sensor introduced in section 5.4.2 is used in conjunction with the Smagorinsky model in all simulations in this chapter.

Moreover, we developed a sensor that removes the undesired turbulent viscosity from the shock areas. The value of this sensor varies from almost zero, in shock regions, to one, in incompressible flow regions. The underlying idea behind designing this sensor is that in the

high turbulence areas the magnitude of the vorticity is high, whereas in the shock areas the dilatation is strong. This sensor, ϕ, is defined as

$$\phi = \frac{|\boldsymbol{\omega}|^2}{|\boldsymbol{\omega}|^2 + (\boldsymbol{\nabla}.\boldsymbol{U})^2 + \epsilon}. \tag{6.1}$$

In Equation 6.1, $\boldsymbol{U}$ denotes the velocity vector, and $\boldsymbol{\omega}$ is the vorticity vector. For all the simulations in this chapter, both wall sensor and shock sensor are applied, and the effective turbulent viscosity is

$$\nu_{t.\text{ef}} = \theta_2 \times \phi \times \nu_t, \tag{6.2}$$

where θ_2, ϕ, and ν_t are given by Equation 5.4, Equation 6.1, and Equation 5.1, respectively. To demonstrate the effects of the wall sensor and the shock sensor on the turbulent viscosity, see Figure 64. It compares the instantaneous turbulent viscosity for a turbulent flow over a ramp-cavity geometry before and after applying the sensor. It is observed that the wall sensor removes a large portion of the turbulent viscosity in the inlet channel with very minor effects on the shear layer and the shock areas. It is also observed that the shock sensor completely removes the turbulent viscosity from the shock area while having nearly no effect in other regions of the flow despite large gradients of the flow variables.

6.2.2 <u>Shock Capturing</u>

The shock capturing tool utilized in this work is an entropy-based artificial viscosity method (114). Chaudhuri *et al.* (66; 6; 115) proposed a modified entropy viscosity method for supersonic
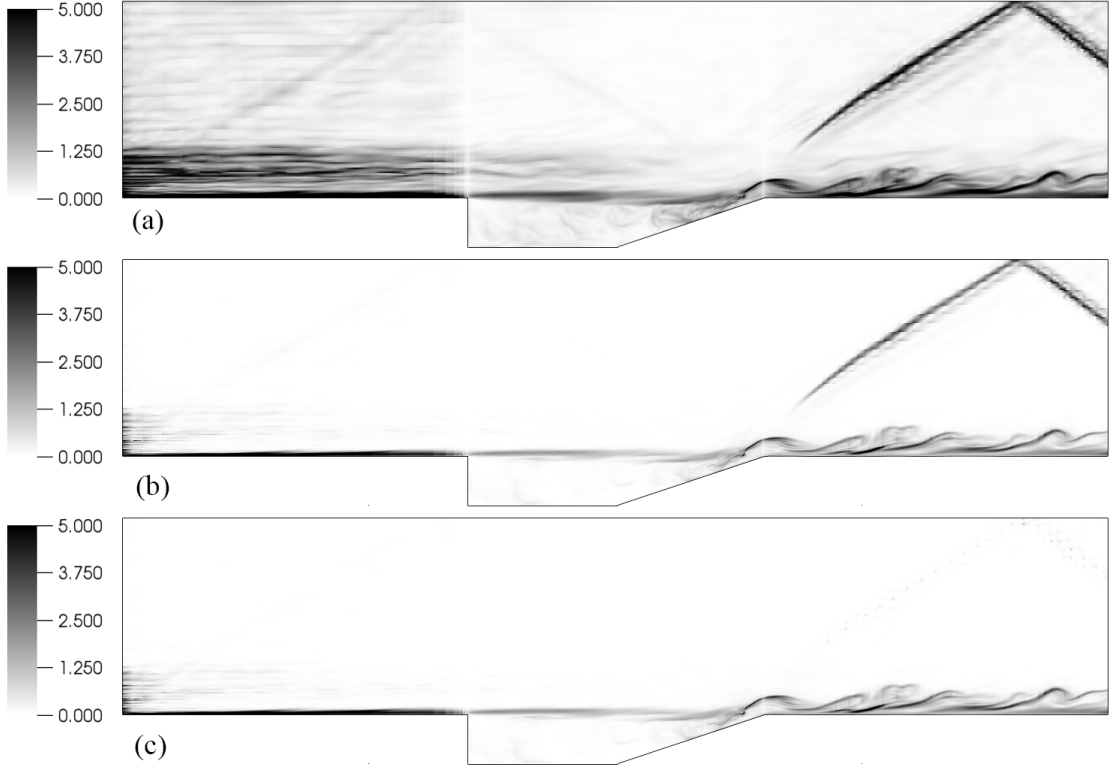
Figure 64. The effect of the wall sensor and the shock sensor on the turbulent viscosity: (a) the original turbulent viscosity, (b) turbulent viscosity after applying the wall sensor, and (c) turbulent viscosity after applying the wall sensor and the shock sensor.

turbulent flows. In entropy viscosity method, the viscosity is calculated based on a residual that measures the deviation of the flow from an isentropic flow.

The entropy transport equation for Navier-Stokes system of equations reads

$$\frac{\partial(\rho s)}{\partial t} + \frac{\partial(\rho s u_j)}{\partial x_j} - \Lambda = \frac{\Phi + \Gamma}{T} \,, \tag{6.3}$$

where s denotes the fluid's entropy and is calculated as

$$s = \frac{\ln(p/p^\gamma)}{\gamma(\gamma - 1)}, \tag{6.4}$$

and

$$\Phi = \frac{2}{Re_f}\left(S_{ij} - \frac{1}{3}\delta_{ij}S_{kk}\right)\left(S_{ij} - \frac{1}{3}\delta_{ij}S_{kk}\right), \quad \Gamma = \frac{1}{Re_f Pr_f(\gamma - 1)M_f^2}\frac{1}{T}\left(\frac{\partial T}{\partial x_j}\frac{\partial T}{\partial x_j}\right),$$

$$\Lambda = \frac{1}{Re_f Pr_f(\gamma - 1)M_f^2}\frac{\partial}{\partial x_j}\left(\frac{1}{T}\frac{\partial T}{\partial x_j}\right),$$

where S_{ij} is the Newtonian stress tensor and δ_{ij} is the Kronecker delta. In Equation 6.3, Φ and Γ are the entropy generation terms due to viscous and thermal dissipations, respectively. These terms remain positive and could be important in the regions where the velocity and temperature gradients are significant. We define the residual based on these two terms only. Therefore,

$$D = \frac{\Phi + \Gamma}{T}. \tag{6.5}$$

For more details of the entropy-viscosity method used in this work, see Abbassi *et al.* (6).

Our preliminary tests revealed that for high Reynolds number flows in the ramp-cavity geometry this method does not fully distinguish between the shocks and the regions with strong turbulent effects, i.e., the method introduces non-zero artificial viscosity in turbulent areas; therefore, a shock indicator proposed by Ducros *et al.* (116) (called Ducros sensor) is applied to improve the capability of the method in distinguishing between shocks and turbulent regions

and reduce the undesired dissipation in shock-free areas. The entropy viscosity residual is multiplied by the value of the Ducros sensor, which is defined by

$$\Psi = \frac{(\boldsymbol{\nabla}.\boldsymbol{u})^2}{(\boldsymbol{\nabla}.\boldsymbol{u})^2 + |\boldsymbol{\omega}|^2 + \epsilon}.$$

(6.6)

In Equation 6.6, $\boldsymbol{u}$ denotes the velocity vector, $\boldsymbol{\omega}$ is the vorticity vector, and ϵ is a small positive real number chosen to avoid numerical divergence for the areas where $\boldsymbol{\nabla}.\boldsymbol{u}$ and vorticity are both zero. The value of the sensor varies from zero, for incompressible regions, to almost one for shock regions.

The EV method features a tunable coefficient, C_E, to adjust the amount of the entropy viscosity (See Equation (9) of Abbassi *et al.* (6)). The magnitude of the artificial viscosity is proportional to this coefficient. Here, we chose $C_E = 8$.

An upper bound is also imposed for both entropy viscosity and turbulent eddy viscosity to control the viscous time step restriction and ensure stability.

$$\begin{cases} \mu_{EV} & \leq & 60\,\mu_{fluid} \\ \\ \nu_t & \leq & 60\,\mu_{fluid}/\rho \end{cases}$$

(6.7)

6.3   Results and Discussions

Two different cases have been studied for the three-dimensional cold flow in a ramp-cavity combustor, with and without a nozzle. The nozzle will be used as the fuel injector in future

simulations of the reacting flow. The two flows will be compared in the following sections. The case without the injector will also be analyzed for three different Reynolds numbers.

Figure 65 depicts the dimensions of the simulated combustor. The main flow is from left to right. The channel height is 5.22 mm and the cavity has a depth of 1.305 mm. The inlet duct and the exit channel both extend 9.135 mm in the streamwise direction. The flat and slanted parts of the cavity both have lengths of 3.915 mm in the streamwise direction. The width of the combustor is constant with a value of 5.22 mm. At the inlet, air enters the combustor at 800 K and atmospheric pressure with a Mach number of $M = 2$.
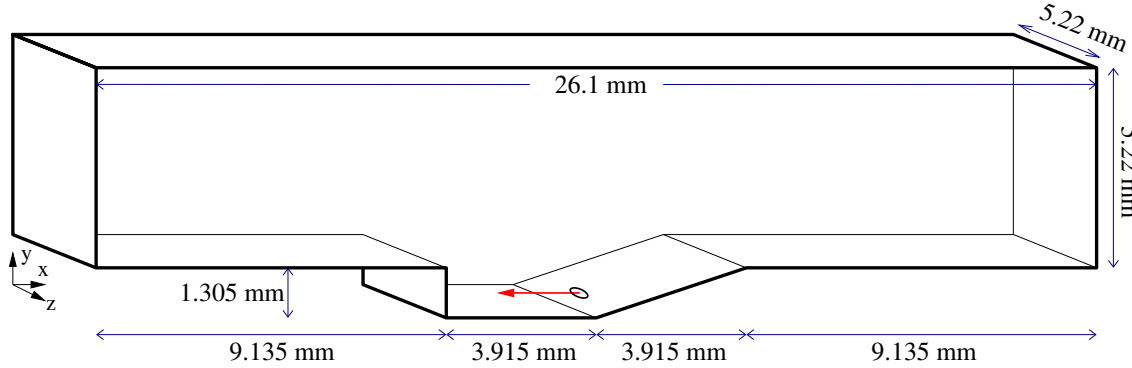
Figure 65. Dimensions of the simulated combustor.

The outflow boundary condition is set to a supersonic outflow condition. Top and bottom walls are adiabatic walls and the side boundaries are treated with periodic boundary conditions. A fully developed boundary layer profile is imposed at the inflow. The mean inflow velocity is

taken from Spalart's boundary layer (90). The inlet turbulence is comprised of synthetically generated fluctuations superimposed on the mean profile (91). The Reynolds number is $Re = 25,288$. The cavity height and the inlet mean velocity are taken as the reference length and the reference velocity, respectively.

6.3.1   Combustor without the Injector

The computational grid used for the simulation of the combustor without injector (Figure 66(a)), consists of 78,165 elements. Inside each element, the solution is approximated as a polynomial of order $P = 2$ resulting in a total of 2,110,455 solution points. There are 15 elements (45 grid points) in the spanwise direction in order to ensure capturing the three-dimensionality of the turbulence. A CFL number of 0.75 is chosen and the average time step size is 1.46×10^{-8} s. The computational cost for this simulation is approximately 357 CPU-hour per flow-through time. The flow-through time is calculated based on the mean velocity at the inlet and the length of the domain in the streamwise direction. A Smagorinsky constant of $C_s = 0.18$ is applied for this simulation. The values of the Smagorinsky constant used for each simulation is given in Table XIII. We selected the Smagorinsky constant for each case based on the stability of the simulation. It is important to note that the final value of the turbulent viscosity will be multiplied by the two sensors introduced earlier. Even though all the values used for C_s are within a small range, the differences could be due to the fact that the values of the sensors are dependent on the flow field and vary with different Reynolds numbers and addition of the injector.
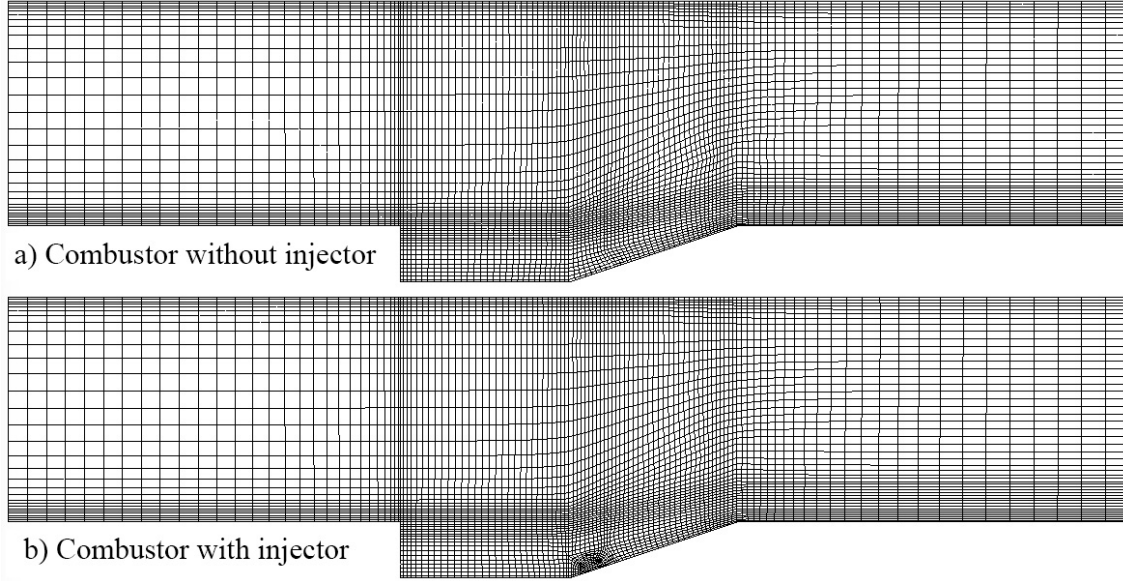
Figure 66. Two-dimensional view of the grid used for the simulation of the ramp-cavity combustor, (a) without injector and (b) with injector.

Figure 67(a)-(c) shows the instantaneous contours of u-velocity, non-dimensional entropy viscosity, and non-dimensional turbulent eddy viscosity for the simulation of the combustor without the injector after 20 flow-through times, plotted in a sample plane perpendicular to the spanwise direction. The entropy viscosity and the turbulent eddy viscosity are scaled by the dynamic viscosity of the fluid.

A number of observations are made from Figure 67. First, the plot of u-velocity shows that the flow is significantly slower inside the cavity than the channel above the shear layer, which is an expected observation for a separated flow. It also reveals that an oblique shock is formed above the end part of the ramped face of the cavity, where the shear layer meets the bottom

TABLE XIII

THE VALUE OF SMAGORINSKY CONSTANT (C_S) USED FOR EACH SIMULATION.

	Reynolds number	C_s
with injector	25,288	0.19
without injector	12,644	0.15
	25,288	0.18
	37,932	0.18

wall of the exit channel. We also observed that this region introduces the strongest numerical instability throughout the domain. Not only are the velocity fluctuations intensified due to the shear layer growth, but also shock and turbulence coexist in that region. The shear layer, which is already expanded, is also forced to adjust to the no-slip condition at the bottom wall of the exit channel. The shock then reflects from the top wall and exits the computational domain. This configuration of the shock agrees with previous work (117).

The plot of the entropy viscosity demonstrates the performance of the shock capturing method. A smooth distribution of viscosity is added at the location of the shock and nearly no viscosity is generated in other regions, despite having strong gradients of velocity and temperature in the turbulent regions. This makes the simulation stable while properly capturing characteristics of the turbulence and the shock.

Due to the density-based sensor applied to the Smagorinsky model, the turbulent eddy viscosity is more concentrated on the turbulent areas of the shear layer and large structures downstream of the shock, and a very low amount of viscosity is added at the inlet boundary

Figure 67. Instantaneous plots from the simulation of non-reactive flow in the combustor, without the injector after 20 flow-through times ($Re = 25,288$, $M = 2.0$). (a) Streamwise u-velocity, (b) Non-dimensional entropy viscosity, and (c) Non-dimensional turbulent eddy viscosity.

layers. The amount of turbulent viscosity added to the shock is also very small, which is a result of adding the previously mentioned shock sensor to the turbulence model.

Figure 68 shows the u-velocity, averaged in time, for the same case. In this plot, the shock does not appear as sharp as it does in the instantaneous plot due to its oscillation. The shock oscillates mainly in the streamwise direction. The location of the shock also varies in the z-
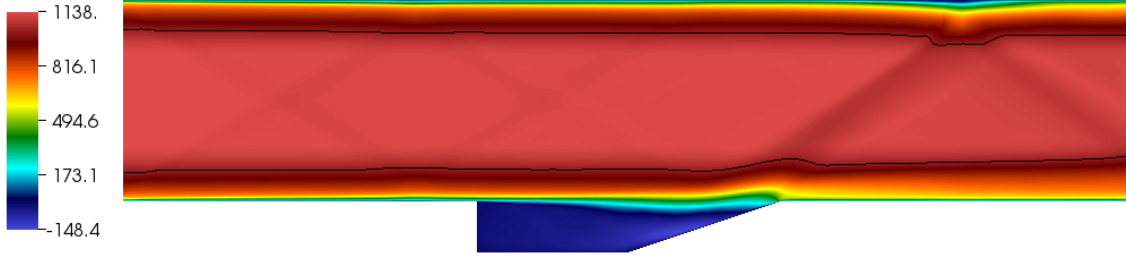
Figure 68. Time-averaged u-velocity (m/s) for the case without injector. The black solid band is the location of $u = 0.9\ u_{max}$.

direction as a result of three-dimensionality of the flow. The black solid band in Figure 68 represents the location where u-velocity is around 90% of the maximum channel velocity. We use this band to trace the behavior of the boundary layer during its interaction with the shock. The observation here is that the boundary layer thickens along the interaction region. This behavior agrees with the strong incident-reflected wave described by Green (118).

We use the invariant (Q) of the velocity gradient tensor,

$$Q = \frac{1}{2}(\Omega_{ij}\Omega_{ij} - \Xi_{ij}\Xi_{ij}), \text{ with } \left\{ \begin{array}{c} \Omega_{ij} = \frac{1}{2}(u_{ij} - u_{ji}) \\ \\ \Xi_{ij} = \frac{1}{2}(u_{ij} + u_{ji}) \end{array} \right\}, \text{ and } u_{ij} = \frac{\partial u_i}{\partial x_j}, \qquad (6.8)$$

to visualize the three-dimensional structures of the flow. Figure 69 shows the iso-surface of Q for the case without the injector. The figure shows half of the full computational domain. The two-dimensional contours superimposed on the plot, which show the density, are located at the center of the domain in the z-direction. From Figure 69 it can be seen that the oblique shock originates from the shear layer near the ramped section of the cavity. Also, turbulence
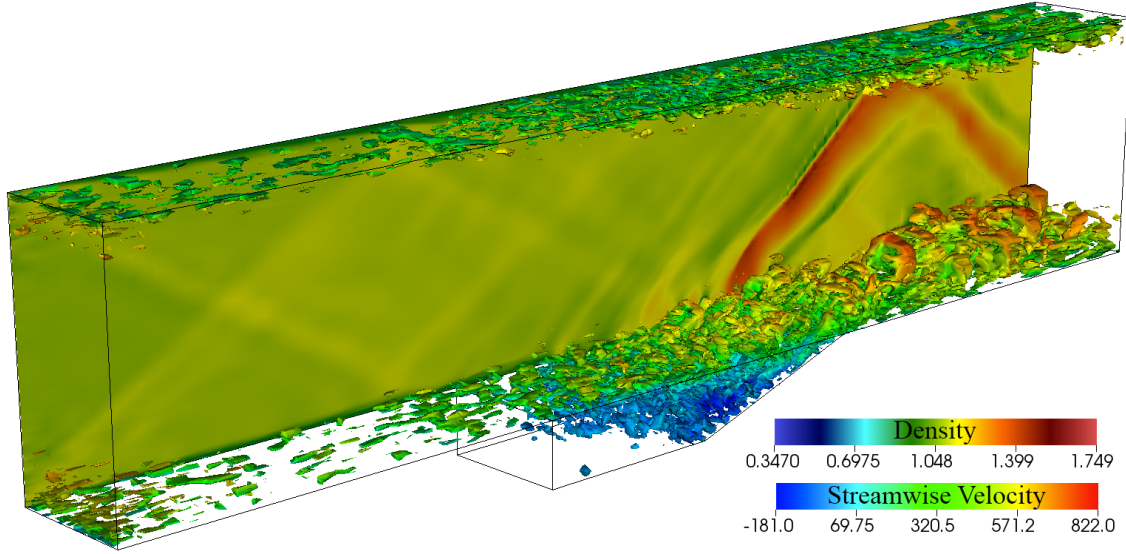
Figure 69. Three-dimensional iso-surfaces of Q colored with stream-wise velocity ($Q = 0.1$) at $Re = 25,288$ and $M = 2$. The color represents the u-velocity (m/s). The two-dimensional contours superimposed on the plot show the density (kg/m^3).

intensifies downstream of the shock and larger hairpin vortices are visible near the lower wall of the exit channel.

6.3.2 Effect of the Injector

The second case uses the same geometry and features a horizontal injector on the ramped face of the cavity (see Figure 65), which blows air in the counter-streamwise direction. According to Gruber *et al.* (108), direct fuel injection from the ramp downstream of the cavity provides the most robust compustion and best fuel mixing. The diameter of the nozzle is 0.138 mm and the center of the hole has a height of 0.18 mm with respect to the bottom of the cavity. The nozzle blows air at the same temperature and pressure as those of the inlet flow. The injector
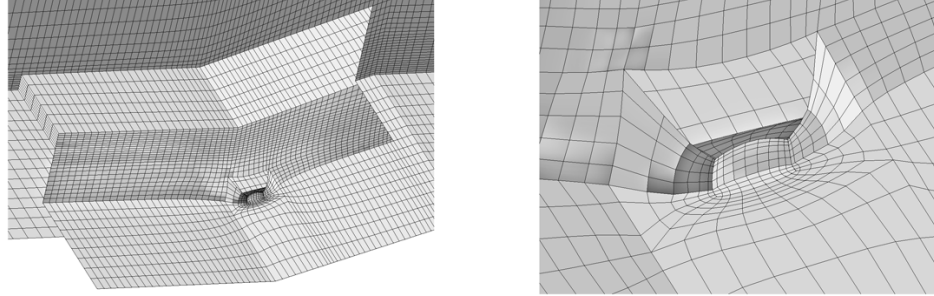
Figure 70. Locally refined unstructured grid to resolve the injector (left), and the magnified view of the injector grid (right).

has a laminar profile with a maximum velocity of 35% of that of the inlet flow and its mass flow rate is 9.6×10^{-5} times the inlet mass flow rate.

The computational grid used for this simulation is shown in Figure 66(b). It consists of 79,191 elements with polynomial order of $P = 2$ and has 2,138,157 solution points. One of the challenges in this simulation is to refine the grid in the vicinity of the injector in order to resolve the small scale mixing effect of the injector. The capability of DSEM in using unstructured grid allows us to efficiently and locally refine the grid such that the resolution is high enough near the injector. The refinement of the unstructured grid near the nozzle is depicted in Figure 70.

A CFL number of 0.75 is imposed for this simulation and the average time step size is 2.38×10^{-9} s. Since the grid spacing is small near the injector, the time step size is more restricted than that of the previous simulation. The computational cost for this simulation is approximately 427 CPU-hour per flow-through time.
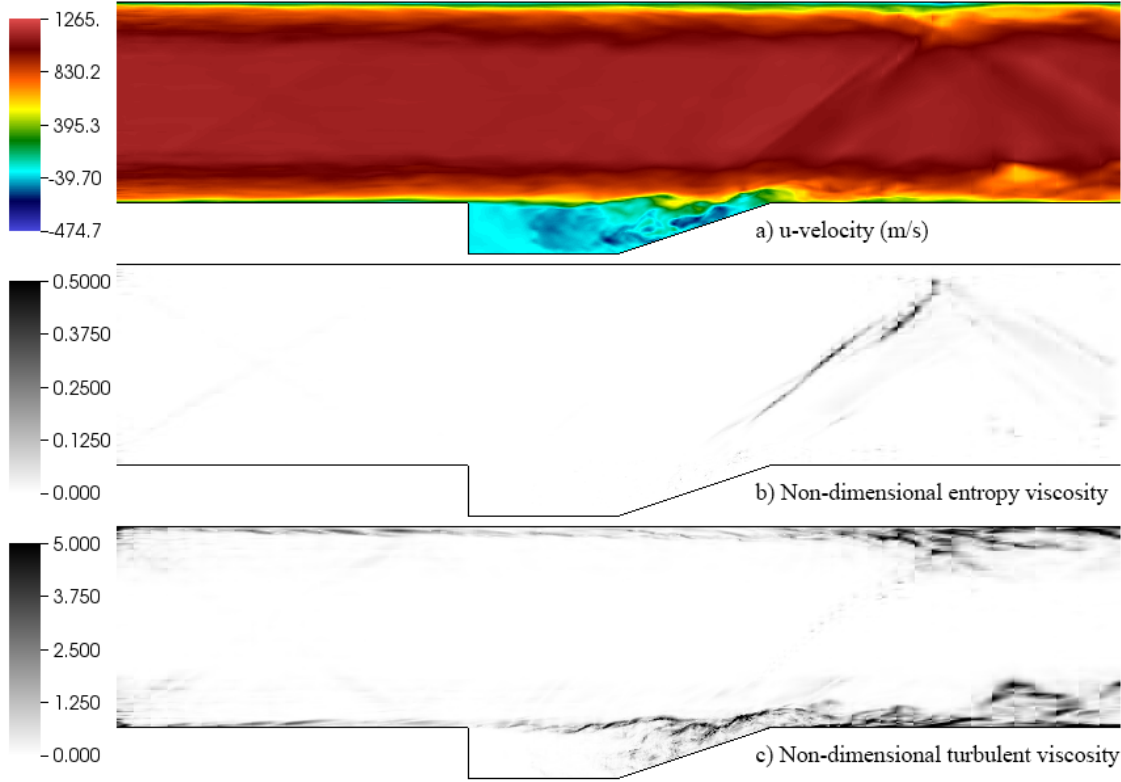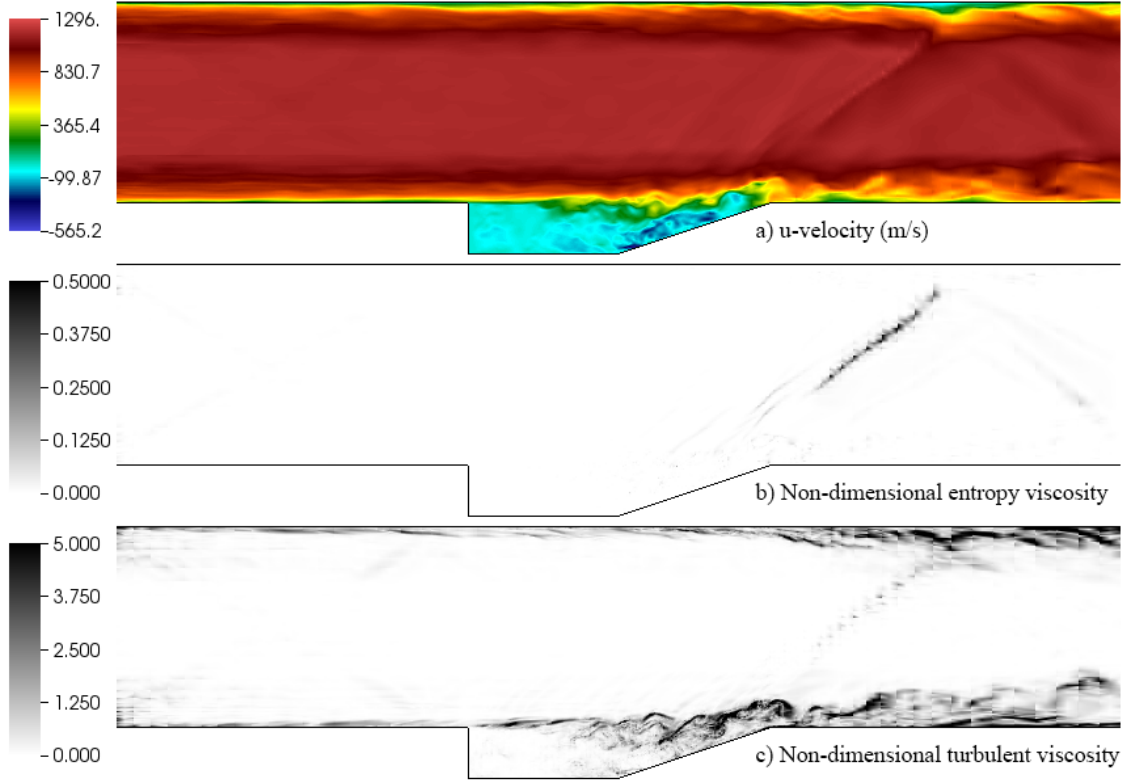
Figure 71. Instantaneous plots from the simulation of non-reactive flow in the ramp-cavity combustor, with the injector after 20 flow-through times ($Re = 25,288$, $M = 2.0$). (a) Streamwise u-velocity, (b) Non-dimensional entropy viscosity, (c) Non-dimensional turbulent eddy viscosity.

Figure 71(a)-(c) shows the instantaneous contours of u-velocity, non-dimensional entropy viscosity, and non-dimensional turbulent eddy viscosity for the simulation of the combustor with the injector after 20 flow-through times. The figures are plotted in the z-plane passing through the center of the injector. The same features as mentioned for the case without the injector can be seen in this figure.

Different aspects of the flow inside the cavity for two cases, with and without injector, are included in Figure 72. The 2D planes shown in this figure are the z-plane passing through the center of the injector for the case with injector and a sample z-plane for the case without injector. The location of the injector is specified with a dashed line. The streamlines in Figure 72(a) reveal more details on the instantaneous paths and directions of the flow inside the cavity and the shear layer. It is worth noting that the reason streamlines are terminated within the flow is the algorithm used to generate them. We seed the cavity with uniformly distributed source points and build each streamline starting from a source point and marching both backward and forward for a finite number of steps. A number of eddies are discernible in the central region of the cavity with the injector, which are observed in all of the instantaneous plots of this case. These eddies, which are fewer in number in the same region of the cavity without the injector, could increase the mixing effects of the cavity flow and improve the combustion quality. In general, more eddies are formed downstream of the cavity, above the ramp, than the upstream, near the step. The reason could be the interaction of the developed shear layer with the ramp.

Contours of the instantaneous magnitude of the temperature gradient for both simulations are shown in Figure 72(b). This parameter makes turbulent structures, as well as shock structures, clearly visible. Large gradients are the dark regions, while white areas indicate no temperature gradient. More structures are visible in the cavity with injector, especially in front of the injector, when compared with the base case. One of the crucial phenomena, which is inherent in this type of combustor, is the interaction of the shear layer with the ramp. Large gradients, as seen in Figure 72(b), meet the ramp at the bottom and the shock at the top. The

shear layer is also required to satisfy the no-slip condition at the corner. Based on our experience, this region is the source of most of the numerical instabilities throughout the domain. Since the case with the injector showed to be more sensitive in that region, we used a higher value of Smagorinsky constant ($C_s = 0.19$) for that case. The reason could be the interaction of the injector flow with the shear layer, resulting in more disturbed shear layer and larger structures meeting the ramp.

Figure 72(c) shows the vorticity contours calculated for the same field as shown in Figure 72(b). Shades of yellow, orange, and red indicate positive values of vorticity, and green, cyan, and blue show negative vorticity areas. According to the direction of the flow, the greatest negative values indicate where the shear layer is located. A wide region of relatively large, positive and negative, vorticity is visible above the ramp for both cases, indicating more eddies are formed in that region. Smaller values and gradients of vorticity are observed upstream of the cavity, which can be attributed to the lower velocity.

Figure 72(d) provides the time-averaged u-velocity at the shear layer and inside the cavity for both cases. For the case without injector, the solution is averaged in the homogeneous direction and time for 20 flow-through times. For the injector case, the solution is averaged only in time for 130 flow-through times. Based on the contour plot of the averaged u-velocity, the flow is similar for both cases, except for the injector flow, which is discernible with large negative values.

The behavior of the shear layer in this type of ramp-cavity geometry can be also seen in Figure 72(d). The shear layer first expands for about a half-length of the cavity followed by a
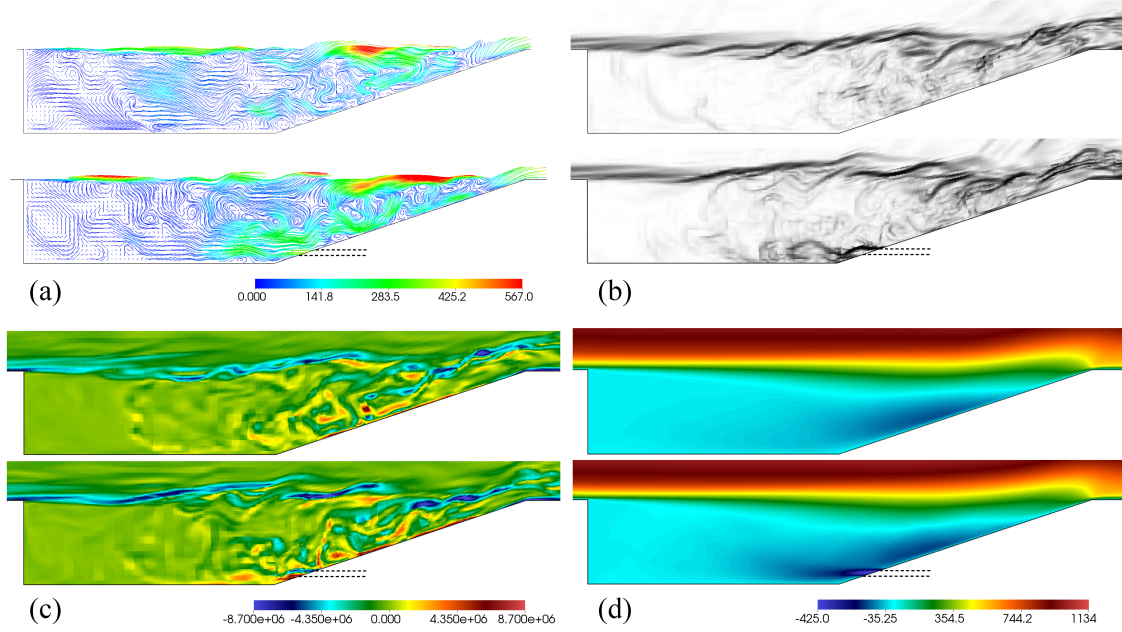
Figure 72. Results for the case with (bottom) and without (top) injector ($Re = 25,288$, $M = 2$): (a) Instantaneous streamlines, colored by velocity (m/s). (b) Instantaneous temperature gradient magnitude. (c) Instantaneous vorticity component, ω_z (s^{-1}). (d) time-averaged u-velocity (m/s).

gentle inclination toward the bottom of the combustor. At the fourth quarter of the cavity we observe a rise in height of the shear layer followed by a shrinkage landing at the ramp corner. The no-slip condition at the corner requires the shear layer to undergo this mechanism.

The contour plot provides a more global view of the flow features, but with less precision. In order to examine the cavity flow in more details velocity profiles are used. The profiles provide a more precise, but less global, means of comparison. Figure 73 compares the velocity profiles inside the cavity for both cases. It presents vertical line plots of u velocity and v velocity at

different x locations inside the cavity. The location of the profiles are shown at the top of the figure for reference. For the case with the injector, these profiles are at the z-plane that passes through the center of the injector.

The first observation from the plots in Figure 73 is that the difference between the two cases, as well as the flow speed, are minimal in the left side of the cavity ($x = 7.3$ and $x = 8.2$). From the u-velocity plots, it is also clear that in front of the injector ($x \leq 10$) the flow is faster at the lower half of the cavity comparing to the case without injector. As expected, this higher speed is the direct result of the injector flow, which is horizontal and directed to the left. This effect, however, is diminished as we approach to the upstream step. The injector flow, by virtue of its location and direction, also reinforces the large clockwise circulation throughout the cavity. The slightly larger u-velocity at the upper half of the cavity, downstream of the injector (seen at $x = 10$ and $x = 10.9$), could be associated with this effect.

The stronger clockwise circulation within the cavity for the case with the injector is visible also in v-velocity plots. The larger negative v-velocity at $x = 10.9$ and $x = 11.8$ is also related to this effect. At $x = 10$ and $y < 0.25$ we also see deviations in v-velocity from the base flow. Larger negative v-velocity at the bottom and smaller negative v-velocity at the top of the injector center-line are due to the expansion of the injector flow.

6.3.3 Effect of Reynolds Number

The non-reactive flow within the combustor without the injector has been simulated at different Reynolds numbers and the results are compared in order to examine the effect of the Reynolds number on the flow features. Different Reynolds numbers are achieved by propor-
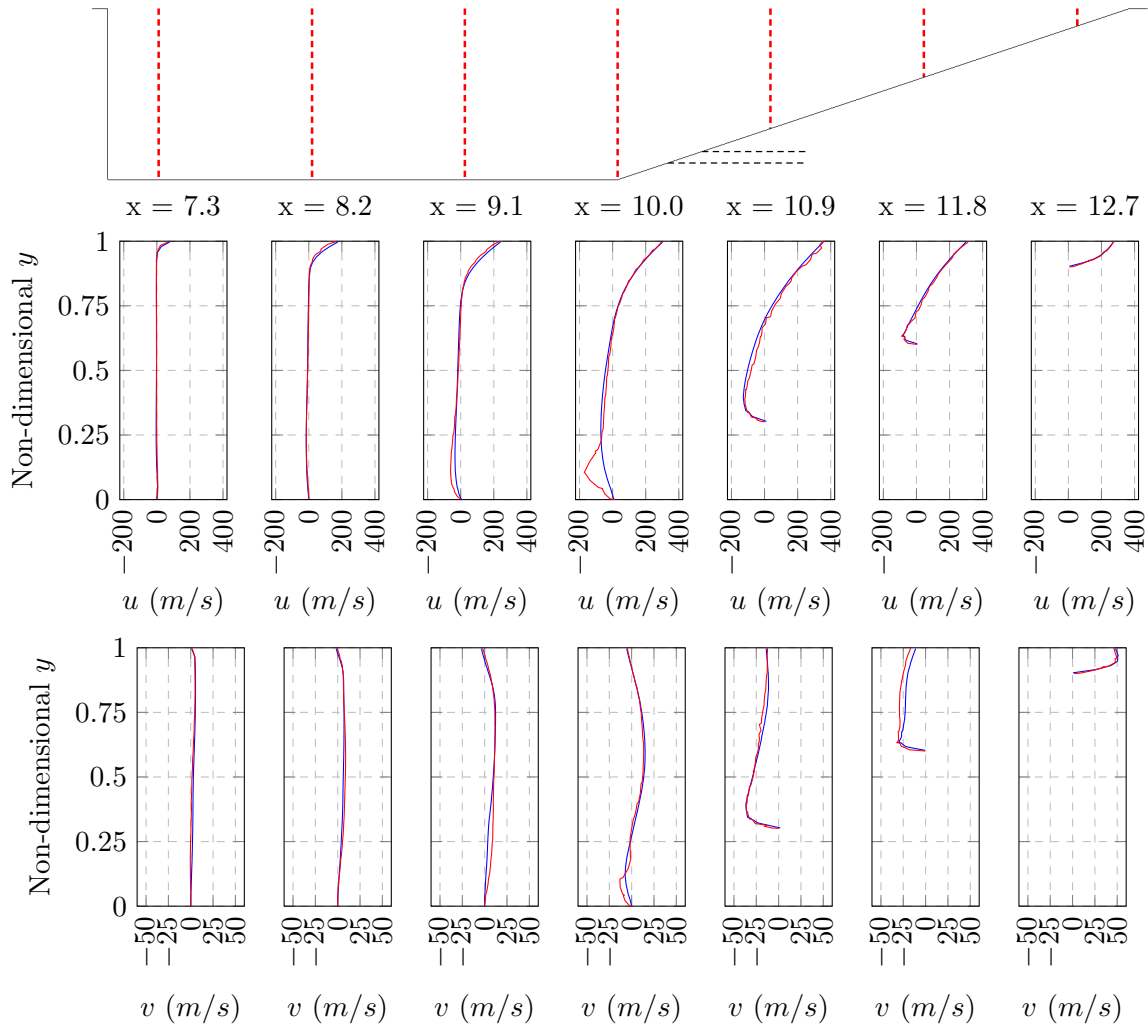
Figure 73. Vertical profiles of time-averaged u and v velocity for the combustor with (red) and without (blue) injector at different x-locations (x: Non-dimensional streamwise location). The location of the line plots are shown with dashed red line (top).

tionally changing the size of the combustor. Three cases have been simulated with Reynolds numbers of $Re = 12,644$, $Re = 25,288$, and $Re = 37,932$. The grid used for these simulations is the same grid used for the simulation of the combustor without injector.

The magnitude of the temperature gradient for the above-mentioned three cases are provided in Figure 74. The shear layer tends to be disturbed earlier at the higher Reynolds number and consequently results in more and stronger turbulent structures at the location of the interaction of the shear layer and the ramp.

Figure 75 shows contours of time-averaged pressure for the base case ($Re = 25,288$) and line plots of pressure across the shock for three different Reynolds numbers. The contour plot reveals the high pressure regions at the primary shock and the reflected shock wave. The highest pressure occurs at the location of the shock-boundary layer interaction with a value of $P_{max} = 1.56 \; atm$ in this case. The flow in the core of the channel experiences a rapid change in pressure due to the shock. In contrast, since the flow inside the boundary layer adjacent to the top wall has a subsonic speed, it cannot undergo a discontinuous change in pressure. Therefore, high pressure penetrates upstream through the subsonic layer of the boundary layer and the overall change in pressure takes place gradually within a distance inside the boundary layer. The weak Mach waves generated at the inlet are also more visible in this plot. These waves have shown to be intensified by increasing the amount of turbulent eddy viscosity at the inlet.

From the line plots of the pressure across the shock, we see the primary shock, located at $x = 14.75$ (non-dimensionalized by the cavity height) followed by the expansion wave. Then, the flow passes through the compression and expansion waves of the reflected shock wave,

Figure 74. Instantaneous temperature gradient magnitude for the combustor without injector, at three different Reynolds numbers.

respectively. Because of the shock oscillation, the shock appears less sharp in this plot than it does in the instantaneous plot. There is about 30% increase in pressure at the primary shock. The line plots also uncover the effect of the Reynolds number on the shock. With an increase in Reynolds number the shock, and consequently the reflected shock wave, gently incline toward
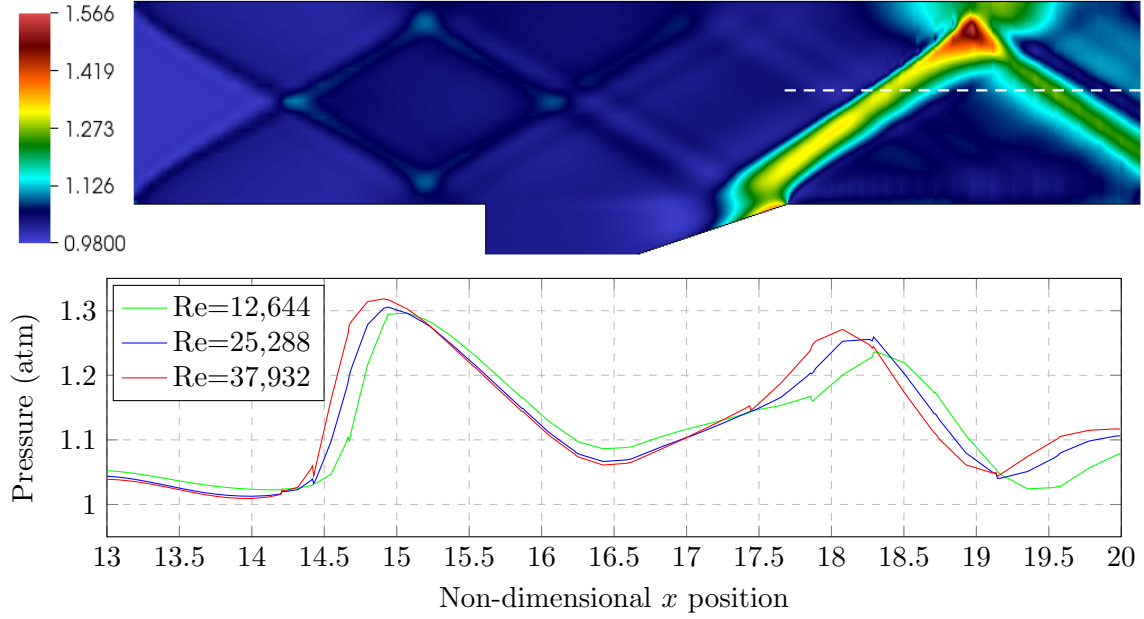
Figure 75. Contours of time-averaged pressure (atm) for $Re = 25,288$ (top) and pressure profiles across the shock for three different Reynolds numbers (bottom). The location of the profiles is specified with dashed white line in the contour plot.

upstream of the channel. We also observe slightly stronger shock at higher Reynolds numbers suggested by the larger change in pressure.

6.4   Summary and Conclusions

An entropy-based, artificial viscosity method has been implemented in a discontinuous spectral element method (DSEM) in order to simulate supersonic turbulent non-reactive flow in a ramp-cavity combustor. The simulation was then extended by adding a small injector at the back face of the cavity. Three-dimensional simulations have been performed for the supersonic combustor and stable solutions are obtained with well resolved shock and turbulence. Resolv-

ing both shock and turbulence has proven challenging in high-order numerical methods. The combustor without injector was also simulated for different Reynolds numbers and the results were compared. At higher Reynolds numbers, the shock was steeper and stronger.

The entropy-viscosity (EV) method introduced in this work was shown suitable for high Reynolds number supersonic flows, captures the shock adequately, and does not generate excessive viscosity in the regions with high turbulence effects. The high-order DSEM equipped with EV was shown to be able to successfully simulate supersonic turbulent flows in complex geometries.

The cavity flow and the shear layer at the cavity were compared for two cases, with and without injector. The shear layer for the case with injector had a slightly more disturbed shear layer and more eddies inside the cavity. Such features made the simulation more numerically unstable and required the addition of more turbulent viscosity.

CHAPTER 7

SUMMARY AND CONCLUSIONS

The objective of the present dissertation is to develop numerical tools and techniques for high-fidelity simulations of supersonic turbulent reacting flows using discontinuous spectral elements method (DSEM). The primary focus in this work is on the turbulence modeling, while preliminary steps are taken for the application of supersonic turbulent flows in high-speed combustors. A modal explicit filtering technique is introduced and tested for the use in LES using DSEM. A density-based sensor that improves the performance of the Smagorinsky model for separating flows is also developed, implemented, and tested for a turbulent flow over a backward-facing step (BFS).

The near-wall spatial resolution requirement for direct numerical simulation (DNS) of turbulent flows using DSEM is studied and presented in chapter 3. It is important to employ the correct resolution near the wall since an under-resolved grid leads to inaccurate flow statistics, and, on the other hand, an over-resolved grid near the wall greatly increases the computational cost due to the non-uniform nature of Chebyshev grids. DNS's of periodic channel flow are performed using different grid resolutions. Three different polynomial orders of $P = 2$, 5, and 7 are used to study the effect of approximation order on the resolution requirement, and three different near-wall resolutions are employed for each polynomial order. The major conclusions are as follows.

1. The near-wall resolution requirement strongly depends on the approximation order; for an approximation order of $P = 7$, eight grid points within y_{10}^{+} is sufficient for accurate statistics, while for an approximation order of $P = 2$, even having 11 points within y_{10}^{+} results in inaccurate statistics.

2. The near-wall resolution has little effect on the mean flow statistics; only $P2$ cases slightly underpredict the mean velocity and overpredict the friction Reynolds number.

3. By comparing the rms velocity fluctuations, we realize that higher polynomial order with the same resolution provides more accurate results, and regardless of the P, increasing resolution improves the statistics.

4. Higher-P cases are generally more computationally expensive than lower-P cases, with the same total number of grid points. However, they provide significantly more accurate results.

In chapter 4, a modal explicit filtering method is introduced and tested for the use in LES of turbulent flow using DSEM. The filter removes the high-frequency motions by setting higher modes of the flow to zero in the spectral space. The proposed method is tested for isotropic turbulence as well as turbulent flow in a planar periodic channel. The method produced promising results including first- and second-order statistics comparing with DNS. It is also shown that the strength of the filter should be a function of only polynomial order. The method also showed superior performance over nodal filtering and dynamic Smagorinsky model in terms of the computational cost.

LES as well as DNS of a turbulent flow over a BFS is performed and studied in chapter 5. A density-based sensor that improves the performance of the standard Smagorinsky model in the vicinity of walls is developed, implemented, and tested for the flow over BFS. The sensor removes the undesired viscosity that is introduced by the turbulence model inside the boundary layer and would inhibit the development of turbulence. It is shown that the addition of the sensor to the Smagorinsky model significantly improves the accuracy of the model. The LES case without the sensor has a large error in mean velocities and severely underpredicts the rms velocity fluctuations, while the case featuring the sensor predicts close values pf both mean and rms velocities to the DNS case. The error in the prediction of the reattachment length is dropped from 18.4% to -0.5% after applying the wall sensor.

Large eddy simulations of turbulent supersonic flow in a 3D ramp-cavity combustor are also presented in chapter 6. Stable solution is obtained using the standard Smagorinsky model featuring the wall sensor and an entropy-viscosity (EV) shock capturing method. A sensor is also developed and added to the turbulence model to distinguish between the shock and turbulent areas. The sensor removes the undesired viscosity that is introduced by the Smagorinsky model at the shock due to the large local gradient of the velocity field. A case with a fuel injector at the ramped wall of the cavity is also tested. It is shown that in the case with the injector, the shear layer formed at the step is slightly more disturbed, and there are more eddies inside the cavity. The effect of the Reynolds number on the shock is also studied by considering three different Reynolds numbers, and it was observed that a higher Reynolds number results in a steeper and a stronger shock.

The focus of the research that is presented in this dissertation is more on the turbulence than the other two major components of the high-speed engine flow, i.e., shock and reaction. However, preliminary results for turbulent supersonic flows are also presented. Preliminary simulations of turbulent reacting flow in ramp-cavity combustors with fuel injectors using scalar transport equations are also performed (119; 120; 121). The research may be continued by combining all three major components of the flow in a single stable simulation. The most prominent challenge toward such simulation is stability. Each of the three components are sources of strong instabilities, especially in such a high-order method.

APPENDICES

Appendix A

DISCRETE CHEBYSHEV TRANSFORM

In this appendix, the transformation procedures between the nodal space and the modal space are described. In a one-dimensional version, assume the solution values $\tilde{u}(X)$ within an element in the mapped space are defined using basis functions of order P on a grid with a Chebyshev distribution of points, $X'_{i+\frac{1}{2}}$, given by

$$X'_{i+\frac{1}{2}} = \cos\left(\frac{i + \frac{1}{2}}{N}\,\pi\right), \quad i = 0, \ldots, N - 1\,, \tag{A.1}$$

where $N = P + 1$ is the number of grid points. For simplicity, we assume that the solution is defined on the interval $[-1, 1]$. Then, the discrete Chebyshev transform (DChT) (69) of $\tilde{u}(X)$ is given by $\hat{u}_k$, where

$$\hat{u}_k = \frac{2}{N} \sum_{i=0}^{N-1} \tilde{u}(X'_{i+\frac{1}{2}})\, T_k(X'_{i+\frac{1}{2}}), \quad k = 0, \ldots, N - 1. \tag{A.2}$$

Here, T_k is the Chebyshev polynomial of degree k, defined by $T_k(x) = \cos(k \arccos(x))$. The inverse transform (iDChT) is given by

$$\tilde{u}(X_{i+\frac{1}{2}}) = \frac{1}{2}\,\hat{u}_0 + \sum_{k=1}^{N-1} \hat{u}_k\, T_k(X'_{i+\frac{1}{2}}), \quad i = 0, \ldots, N - 1. \tag{A.3}$$

Appendix A (Continued)

After applying Equation A.1 and the definition of the Chebyshev polynomial, Equation A.2

and Equation A.3 become

$$\hat{u}_k = \frac{2}{N} \sum_{i=0}^{N-1} \tilde{u}(X_{i+\frac{1}{2}}) \cos\left[\frac{k\pi}{N}\left(i + \frac{1}{2}\right)\right], \quad k = 0, \ldots, N-1, \tag{A.4}$$

and

$$\tilde{u}(X_{i+\frac{1}{2}}) = \frac{1}{2}\hat{u}_0 + \sum_{k=1}^{N-1} \hat{u}_k \cos\left[\frac{k\pi}{N}\left(i + \frac{1}{2}\right)\right], \quad i = 0, \ldots, N-1. \tag{A.5}$$

Equation A.4 and Equation A.5 are the DChT and iDChT and are used to transform the

solutions between the nodal and the modal representations. To implement the DChT and

iDChT in the DSEM code, the discrete cosine transform (DCT) and the inverse discrete cosine

transform (iDCT) from the library *Fastest Fourier Transform in the West* (FFTW) (70) are

used. The DCT and iDCT functions from FFTW are respectively defined by

$$G_k = 2 \sum_{i=0}^{N-1} F_i \cos\left[\frac{k\pi}{N}\left(i + \frac{1}{2}\right)\right], \quad k = 0, \ldots, N-1, \tag{A.6}$$

and

$$F_i = G_0 + 2 \sum_{k=1}^{N-1} G_k \cos\left[\frac{k\pi}{N}\left(i + \frac{1}{2}\right)\right], \quad i = 0, \ldots, N-1, \tag{A.7}$$

By comparing Equation A.6 and Equation A.7 with Equation A.4 and Equation A.5, one realizes

that the DCT and iDCT can be used to apply the DChT and iDChT with minor modifications

to the output arguments of DCT and iDCT, i.e., dividing the outputs of DCT and iDCT by N

and 2, respectively.

Appendix A (Continued)

The three-dimensional variations of DChT and its inverse are simply separable products of the one-dimensional definitions along each dimension and are defined by

$$\hat{u}_{k_1 k_2 k_3} = \left(\frac{2}{N}\right)^3 \sum_{i_1=0}^{N-1} \sum_{i_2=0}^{N-1} \sum_{i_3=0}^{N-1} \tilde{u}(X_{i_1+\frac{1}{2}}, X_{i_2+\frac{1}{2}}, X_{i_3+\frac{1}{2}}) \, C(k_1, i_1) \, C(k_2, i_2) \, C(k_3, i_3), \quad k_1, k_2, k_3 = 0, \ldots, N-1,$$

$$(A.8)$$

and

$$\tilde{u}(X_{i_1+\frac{1}{2}}, X_{i_2+\frac{1}{2}}, X_{i_3+\frac{1}{2}}) = \sum_{k_1=0}^{N-1} \sum_{k_2=0}^{N-1} \sum_{k_3=0}^{N-1} \hat{u}_{k_1 k_2 k_3} E_{k_1} E_{k_2} E_{k_3} C(k_1, i_1) \, C(k_2, i_2) \, C(k_3, i_3), \quad i_1, i_2, i_3 = 0, \ldots, N-1$$

$$(A.9)$$

respectively, where

$$C(p, q) = \cos\left[\frac{p\pi}{N}\left(q + \frac{1}{2}\right)\right], \tag{A.10}$$

and

$$E_r = \begin{cases} \frac{1}{2}, & r = 0 \\ \\ 1, & r \neq 0 \end{cases}. \tag{A.11}$$

The 3D versions of DCT and iDCT are also provided by FFTW.

Appendix B

DIMENSIONLESS WALL VARIABLES

In this appendix, the definitions of wall variables including the dimensionless wall distance (y^+) are provided. We start with non-dimensionalizations of the flow variables, which are as follows

$$
\begin{cases}
\rho^* = \rho.\rho_f^* \\[2ex]
\nu^* = \nu.\nu_f^* \\[2ex]
u^* = u.u_f^* \\[2ex]
y^* = y.l_f^* \\[2ex]
\tau^* = \tau(\nu_f^{*2} l_f^{*-2} \rho_f^*)
\end{cases}
\tag{B.1}
$$

The variables introduced in Equation B.1 are density, kinematic viscosity, velocity, distance from wall, and wall shear stress, respectively. Also, the superscript * denotes dimensional variables, and the subscript $_f$ indicates the reference variables. The reference Reynolds number is defined by

$$
Re_f = \frac{u_f^* l_f^*}{\nu_f^*}.
\tag{B.2}
$$

We also use the relation between the dynamic and kinematic viscosity,

$$
\mu^* = \rho^* \nu^*.
\tag{B.3}
$$

Appendix B (Continued)

The wall shear stress, τ_w^*, is defined by

$$\tau_w^* = \mu^* \left. \frac{\partial u^*}{\partial y^*} \right|_{y^*=0}, \tag{B.4}$$

where $\left. \frac{\partial u^*}{\partial y^*} \right|_{y^*=0}$ is the gradient of the streamwise velocity in wall-normal direction, determined at the wall. Applying the non-dimensional variables, the non-dimensional wall shear stress, τ_w, is obtained as

$$\tau_w = Re_f \rho \nu \left. \frac{\partial u}{\partial y} \right|_{y=0}. \tag{B.5}$$

The dimensional (u_τ^*) and non-dimensional (u_τ) versions of the shear velocity are also given by

$$u_\tau^* = \sqrt{\frac{\tau_w^*}{\rho^*}} \;\Rightarrow\; u_\tau = \frac{u_\tau^*}{u_f^*} = \sqrt{\frac{\nu \left. \frac{\partial u}{\partial y} \right|_{y=0}}{Re_f}}. \tag{B.6}$$

The friction (shear) Reynolds number is defined by

$$Re_\tau = \frac{u_\tau^* \delta^*}{\nu^*} = \sqrt{\frac{Re_f}{\nu} \cdot \left. \frac{\partial u}{\partial y} \right|_{y=0}}. \tag{B.7}$$

The dimensionless wall distance (y^+) is then defined by

$$y^+ = \frac{u_\tau^* y^*}{\nu^*} = y \sqrt{\frac{Re_f}{\nu} \cdot \left. \frac{\partial u}{\partial y} \right|_{y=0}} = y.Re_\tau. \tag{B.8}$$

Appendix B (Continued)

The skin friction coefficient is defined by

$$C_f = \frac{\tau_w^*}{\frac{1}{2}\,\rho^*\,\overline{U}^{*2}} = \frac{2\,\nu\,\left.\frac{\partial u}{\partial y}\right|_{y=0}}{Re_f\,\overline{U}^2}.$$

(B.9)

Finally, the wall shear (friction) temperature is defined as

$$T_\tau^* = \frac{q_w^*}{\rho^* c_p^* u_\tau^*} = \frac{k^*\,\left.\frac{\partial T^*}{\partial y^*}\right|_{y^*=0}}{\rho^* c_p^* u_\tau^*}.$$

(B.10)

Applying the non-dimensional variables, we obtain the non-dimensional wall shear temperature

as

$$T_\tau = \frac{T_\tau^*}{T_f^*} = \frac{\left.\frac{\partial T}{\partial y}\right|_{y=0}}{\rho u_\tau Re_f Pr_f}.$$

(B.11)

Appendix C

POISEUILLE FLOW TEMPERATURE PROFILE

In this appendix, the derivation of the non-dimensional temperature profile in a Poiseuille channel flow is provided. The dimensional temperature profile in a Poiseuille channel flow is given by (see Equation (12.44) of Boundary-Layer Theory (122))

$$\Delta T^* = T^*(y) - T_w^* = \frac{1}{3}\frac{\mu^*}{k^*}u_m^{*\,2}\big[1 - (y-1)^4\big]; \quad 0 < y < 2, \tag{C.1}$$

where u_m^* is the maximum velocity at the center of the channel (at $y = 1$). Applying the non-dimensional variables,

$$u^* = uu_f^*; \quad T^* = TT_f^*; \quad Pr_f = \frac{c_p^*\mu^*}{k^*}; \quad M_f = \frac{u_f^*}{\sqrt{\gamma R^* T_f^*}}, \tag{C.2}$$

and the relations between the specific heat capacities,

$$R^* = c_p^* - c_v^*; \quad \gamma = \frac{c_p^*}{c_v^*}, \tag{C.3}$$

the non-dimensional temperature profile reads

$$\Delta T = T(y) - T_w = \frac{(\gamma - 1)}{3}u_m^2 Pr_f M_f^2\big[1 - (y-1)^4\big]; \quad 0 < y < 2. \tag{C.4}$$

Appendix C (Continued)

Assuming a parabolic velocity profile with the bulk velocity as the reference velocity, we will have $u_m = 3/2$. Therefore, the temperature profile becomes

$$\Delta T = T(y) - T_w = \frac{3(\gamma - 1)}{4} Pr_f M_f^2 \left[1 - (y - 1)^4\right]; \quad 0 < y < 2. \tag{C.5}$$

Appendix D

KOLMOGOROV SCALES

In this appendix, the definitions of the Kolmogorov length and time scales for turbulent flows are provided. The source of the material provided in this appendix is *Turbulent Flows* book by Pope (93). The Kolmogorov length scale is the scale at which the turbulent energy is dissipated. This non-dimensional length scale is defined based only on dissipation rate (ϵ) and viscosity (ν) and is given by

$$\eta^* = \left(\frac{\nu^{*3}}{\epsilon^*}\right)^{1/4}. \tag{D.1}$$

The dissipation rate itself is estimated by

$$\epsilon^* \approx \frac{U^{*3}}{L^*}. \tag{D.2}$$

Applying the estimation of the dissipation to Equation D.1, we obtain

$$\eta^* \approx \left(\frac{\nu^{*3}L^*}{U^{*3}}\right)^{1/4} \tag{D.3}$$

Applying the definition of the reference Reynolds number, $Re_f = u_f^* l_f^* / \nu_f^*$, Equation D.3 becomes

$$\eta \approx \left(\frac{\nu^3 L}{U^3 Re_f^3}\right)^{1/4}. \tag{D.4}$$

Appendix D (Continued)

Equation D.4 is the definition of the Kolmogorov length scale based on non-dimensional flow variables.

Similar to the Kolmogorov length scale, we can define the Kolmogorov time scale, which is the time scale of the smallest eddies. This scale is also defined based only on dissipation rate (ϵ) and viscosity (ν) and is given by

$$t_\eta^* = \left(\frac{\nu^*}{\epsilon^*}\right)^{1/2}.$$
(D.5)

Using the estimation for the dissipation rate (Equation D.2), the Kolmogorov time scale becomes

$$t_\eta^{*2} \approx \frac{\nu^* L^*}{U^{*3}}.$$
(D.6)

Again, applying the definition of the reference Reynolds number, we can obtain the definition of the Kolmogorov time scale based on non-dimensional flow variables as

$$t_\eta \approx \left(\frac{\nu L}{U^3 Re_f}\right)^{1/2}.$$
(D.7)

Appendix E

PUBLISHERS COPYRIGHT POLICY

E.1   International Journal of Heat and Mass Transfer

Submission of an article implies that the work described has not been published previously (except in the form of an abstract, a published lecture or academic thesis, see 'Multiple, redundant or concurrent publication' for more information), that it is not under consideration for publication elsewhere, that its publication is approved by all authors and tacitly or explicitly by the responsible authorities where the work was carried out, and that, if accepted, it will not be published elsewhere in the same form, in English or in any other language, including electronically without the written consent of the copyright-holder. To verify originality, your article may be checked by the originality detection service Crossref Similarity Check. (123)

E.2   American Institute of Aeronautics and Astronautics

Appendix E (Continued)

License Number	4196631259648
License date	Sep 26, 2017
Licensed content publisher	American Inst of Aeronautics and Astronautics (AIAA)
Licensed content title	54th AIAA Aerospace Sciences Meeting
Licensed content date	Jan 1, 2016
Type of Use	Thesis/Dissertation
Requestor type	Author of requested content
Format	Print
Portion	chapter/article
Number of pages in chapter/article	14
Title or numeric reference of the portion(s)	My request: I would like to use the material from my paper in my PhD thesis. I am the first author of the paper. I am not sure if I am filling the right form or not. It is very confusing.
Title of the article or chapter the portion is from	Simulation of Supersonic Turbulent Non-Reactive Flow in Ramp-Cavity Combustor Using a Discontinuous Spectral Element Method
Editor of portion(s)	N/A
Author of portion(s)	Zia Ghiasi

CITED LITERATURE

1. Advanced Cyberinfrastructure for Education and Research. `http://acer.uic.edu/`, Accessed: 2018-02-06.

2. Prandtl, L.: On the motion of fluids of very small viscosity. In Third International Congress of Mathematicians, 1904.

3. Anderson Jr, J. D.: Introduction to Flight. McGraw-Hill, 2004.

4. Clancy, L. J.: Aerodynamics. Halsted Press, 1975.

5. Wang, Z. J., Fidkowski, K., Abgrall, R., Bassi, F., Caraeni, D., Cary, A., Deconinck, H., Hartmann, R., Hillewaert, K., Huynh, H. T., et al.: High-order cfd methods: current status and perspective. International Journal for Numerical Methods in Fluids, 72(8):811–845, 2013.

6. Abbassi, H., Mashayek, F., and Jacobs, G.: Entropy viscosity approach for compressible turbulent simulations using discontinuous spectral element method. In AIAA Paper, number 2014-0947, 2014.

7. Kopriva, D. A. and Kolias, J. H.: A conservative staggerd-grid Chebyshev multidomain method for compressible flows. Journal of Computational Physics, 125(1):244–261, 1996.

8. Kopriva, D. A.: A conservative staggered-grid chebyshev multidomain method for compressible flows. ii. a semi-structured method. Journal of Computational Physics, 128(2):475–488, 1996.

9. Kopriva, D. A.: A staggered-grid multidomain spectral method for the compressible Navier-Stokes equations. Journal of Computational Physics, 244:142–158, 1998.

10. Jacobs, G. B.: Numerical Simulation of Two-Phase Turbulent Compressible Flows with a Multidomain Spectral Method. Ph.D. Thesis, University of Illinois at Chicago, 2003.

11. Li, D., Ghiasi, Z., Komperda, J., and Mashayek, F.: The effect of inflow mach number on the reattachment in subsonic flow over a backward-facing step. In AIAA Paper, number 2016-2077, 2016.

12. Ghiasi, Z., Komperda, J., Li, D., and Mashayek, F.: Simulation of supersonic turbulent non-reactive flow in ramp-cavity combustor using a discontinuous spectral element method. In AIAA Paper, number 2016-0617, 2016.

13. Li, D., Ghiasi, Z., Komperda, J., and Mashayek, F.: A numerical study of compressibility effects in turbulent mixing layer. In Tenth International Symposium on Turbulence and Shear Flow Phenomena, 2017.

14. Patera, A. T.: A spectral element method for fluid dynamics - Laminar flow in channel expansion. Journal of Computational Physics, 54:468–488, 1984.

15. Liu, Y., Vinokur, M., and Wang, Z.: Spectral difference method for unstructured grids i: basic formulation. Journal of Computational Physics, 216(2):780–801, 2006.

16. Kopriva, D. A.: Implementing spectral methods for partial differential equations: Algorithms for scientists and engineers. Springer Science & Business Media, 2009.

17. Ghiasi, Z., Li, D., Komperda, J., and Mashayek, F.: Near-wall resolution requirement for direct numerical simulation of turbulent flow using multidomain chebyshev grid. International Journal of Heat and Mass Transfer, 126, Part B:746 – 760, 2018.

18. Karniadakis, G. E. and Sherwin, S. J.: Spectral/hp Element Methods for CFD. New York, NY, Oxford University Press, 1999.

19. Komperda, J., Ghiasi, Z., Mashayek, F., Irannejad, A., and Jaberi, F. A.: Filtered mass density function for use in discontinuous spectral element method. AIAA Paper 2014-3471, 2014.

20. Komperda, J., Ghiasi, Z., Li, D., Mashayek, F., Irannejad, A., and Jaberi, F.: Simulation of the cold flow in a ramp-cavity combustor using a DSEM-LES/FMDF hybrid scheme. In AIAA Paper, number 2016-1938, 2016.

21. Akherat, S. M. J. M.: Non-Newtonian effects in hemodynamic simulations of the cephalic vein in end stage renal disease patients. Master's thesis, Illinois Institute of Technology, 2013.

22. Ghiasi, Z., Li, D., Komperda, J., and Mashayek, F.: Wall resolution study for direct numerical simulation of turbulent channel flow using a multidomain chebyshev grid. In Tenth International Symposium on Turbulence and Shear Flow Phenomena, 2017.

23. Kim, J., Moin, P., and Moser, R. D.: Turbulent statistics in fully developed turbulent channel flow at low Reynolds number. Journal of Fluid Mechanics, 177:133–166, 1987.

24. Rai, M. M. and Moin, P.: Direct simulations of turbulent flow using finite-difference schemes. Journal of Computational Physics, 96(1):15–53, 1991.

25. Lyons, S. L., Hanratty, T. J., and McLaughlin, J. B.: Large-scale computer simulation of fully developed turbulent channel flow with heat transfer. International Journal for Numerical Methods in Fluids, 13(8):999–1028, 1991.

26. Crawford, C. H.: Direct Numerical Simulation of Near-Wall Turbulence - Passive and Active Control. Doctoral dissertation, Princeton University, 1996.

27. Moser, R. D., Kim, J., and Mansour, N. N.: Direct numerical simulation of turbulent channel flow up to $Re_\tau = 590$. Physics of Fluids, 11(4):943–945, 1999.

28. Del Alamo, J. C. and Jiménez, J.: Spectra of the very large anisotropic scales in turbulent channels. Physics of Fluids, 15(6):L41–L44, 2003.

29. Morinishi, Y., Tamano, S., and Nakabayashi, K.: Direct numerical simulation of compressible turbulent channel flow between adiabatic and isothermal walls. Journal of Fluid Mechanics, 502:273–308, 2004.

30. Lee, M. and Moser, R. D.: Direct numerical simulation of turbulent channel flow up to $Re_\tau \approx 5200$. Journal of Fluid Mechanics, 774:395–415, 2015.

31. Grötzbach, G.: Spatial resolution requirements for direct numerical simulation of the rayleigh-bénard convection. Journal of Computational Physics, 49(2):241–264, 1983.

32. Moin, P. and Mahesh, K.: Direct numerical simulation: A tool in turbulence research. Annual Review of Fluid Mechanics, 30:539–578, 1998.

33. Jacobs, G. B., Kopriva, D. A., and Mashayek, F.: A conservative isothermal wall boundary condition for the compressible navier–stokes equations. Journal of Scientific Computing, 30(2):177–192, 2007.

34. Toro, E. F.: Riemann solvers and numerical methods for fluid dynamics: a practical introduction. Springer Science & Business Media, 3 edition, 2013.

35. Mengaldo, G., De Grazia, D., Witherden, F., Farrington, A., Vincent, P., Sherwin, S., and Peiro, J.: A guide to the implementation of boundary conditions in compact high-order methods for compressible aerodynamics. In AIAA Paper, number 2014-2923, 2014.

36. Lenormand, E., Sagaut, P., and Ta Phuoc, L.: Large eddy simulation of subsonic and supersonic channel flow at moderate Reynolds number. International Journal for Numerical Methods in Fluids, 32(4):369–406, 2000.

37. Wang, S., Gao, Z., and Lee, C.: Numerical investigation of compressibility effects in turbulent channel flows using large eddy simulation. SCIENCE CHINA Physics, Mechanics & Astronomy, 55(2):305–315, 2012.

38. Kawamura, H., Ohsaka, K., Abe, H., and Yamamoto, K.: DNS of turbulent heat transfer in channel flow with low to medium-high prandtl number fluid. International Journal of Heat and Fluid Flow, 19(5):482–491, 1998.

39. Kader, B.: Temperature and concentration profiles in fully turbulent boundary layers. International journal of heat and mass transfer, 24(9):1541–1544, 1981.

40. Dean, R. B.: Reynolds number dependence of skin friction and other bulk flow variables in two-dimensional rectangular duct flow. Journal of Fluids Engineering, 100(2):215–223, 1978.

41. Huang, P. G., Coleman, G. N., and Bradshaw, P.: Compressible turbulent channel flows: DNS results and modelling. Journal of Fluid Mechanics, 305:185–218, 1995.

42. Vasilyev, O. V., Lund, T. S., and Moin, P.: A general class of commutative filters for LES in complex geometries. Journal of Computational Physics, 146(1):82–104, 1998.

43. Gullbrand, J. and Chow, F. K.: The effect of numerical errors and turbulence models in large-eddy simulations of channel flow, with and without explicit filtering. Journal of Fluid Mechanics, 495:323–341, 2003.

44. Lund, T. and Kaltenbach, H.: Experiments with explicit filtering for LES using a finite-difference method. Annual Research Briefs, Center for Turbulence Research, Stanford University, pages 91–105, 1995.

45. Lund, T.: On the use of discrete filters for large eddy simulation. Annual Research Briefs, Center for Turbulence Research, Stanford University, pages 83–95, 1997.

46. Winckelmans, G. S., Wray, A. A., Vasilyev, O. V., and Jeanmart, H.: Explicit-filtering large-eddy simulation using the tensor-diffusivity model supplemented by a dynamic Smagorinsky term. Physics of Fluids, 13(5):1385–1403, 2001.

47. Lilly, D. K.: A proposed modification of the Germano subgrid-scale closure method. Physics of Fluids A: Fluid Dynamics, 4(3):633–635, 1992.

48. Smagorinsky, J.: General circulation experiments with the primitive equations. I. The basic experiment. Monthly Weather Review, 91(3):99–164, 1963.

49. Germano, M., Piomelli, U., Moin, P., and Cabot, W. H.: A dynamic subgrid-scale eddy viscosity model. Physics of Fluids A: Fluid Dynamics, 3(7):1760–1765, 1991.

50. Bardina, J., Ferziger, J. H., and Reynolds, W. C.: Improved subgrid-scale models for large-eddy simulation. In American Institute of Aeronautics and Astronautics, Fluid and Plasma Dynamics Conference, 13th, page 10, 1980.

51. Grinstein, F. F. and Fureby, C.: Recent progress on MILES for high Reynolds number flows. Journal of Fluids Engineering, 124(4):848–861, 2002.

52. Margolin, L. G., Rider, W. J., and Grinstein, F. F.: Modeling turbulent flow with implicit LES. Journal of Turbulence, (7):N15, 2006.

53. Grinstein, F. F., Margolin, L. G., and Rider, W. J.: Implicit large eddy simulation: computing turbulent fluid dynamics. Cambridge university press, 2007.

54. Aspden, A., Nikiforakis, N., Dalziel, S., and Bell, J.: Analysis of implicit LES methods. Communications in Applied Mathematics and Computational Science, 3(1):103–126, 2009.

55. Bogey, C. and Bailly, C.: Computation of a high Reynolds number jet and its radiated noise using large eddy simulation based on explicit filtering. Comput. & Fluids, 35(10):1344–1358, 2006.

56. Mathew, J., Lechner, R., Foysi, H., Sesterhenn, J., and Friedrich, R.: An explicit filtering method for large eddy simulation of compressible flows. Physics of Fluids, 15(8):2279–2289, 2003.

57. Fischer, P. F. and Mullen, J. S.: Filter based stabilization of spectral element methods. Comptes Rendus a l'Academie des Sciences Paris, Ser. 1, Anal. Numer, 332:265–270, 2001.

58. Fischer, P., Lottes, J., Siegel, A., and Palmiotti, G.: Large eddy simulation of wire wrapped fuel pins i: hydrodynamics in a periodic array. In Joint International Topical Meeting on Mathematics & Computation and Super computingin Nuclear Applications (M&C+ SNA 2007), 2007.

59. Sengupta, K.: Direct and Large-eddy Simulation of Compressible Flows with Spectral/hp Element Methods. Ph.D. Thesis, University of Illinois at Chicago, 2008.

60. Kanchi, H., Mashayek, F., Sengupta, K., Jacobs, G., and Fischer, P.: Comparison of LES studies in backward-facing step using Chebyshev multidomain and Legendre spectral element methods. In AIAA Paper, number 2011-3557, 2011.

61. Boyd, J. P.: The erfc-log filter and the asymptotics of the Euler and Vandeven sequence accelerations. In Proceedings of the Third International Conference on Spectral and High Order Methods, pages 267–276. Houst. J. Math., 1996.

62. Boyd, J. P.: Two comments on filtering (artificial viscosity) for Chebyshev and Legendre spectral and spectral element methods: preserving boundary conditions and interpretation of the filter as a diffusion. Journal of Computational Physics, 143(1):283–288, 1998.

63. Levin, J. G., Iskandarani, M., and Haidvogel, D. B.: A spectral filtering procedure for eddy-resolving simulations with a spectral element ocean model. Journal of Computational Physics, 137(1):130–154, 1997.

64. Blackburn, H. M. and Schmidt, S.: Spectral element filtering techniques for large-eddy simulation with dynamic estimation. Journal of Computational Physics, 186(2):610–629, 2003.

65. Bouffanais, R., Deville, M. O., Fischer, P. F., Leriche, E., and Weill, D.: Large-eddy simulation of the lid-driven cubic cavity flow by the spectral element method. Search Results Journal of Scientific Computing, 27(1):151–162, 2006.

66. Chaudhuri, A., Jacobs, G. B., Don, W.-S., Abbassi, H., and Mashayek, F.: Explicit discontinuous spectral element method with entropy generation based artificial viscosity for shocked viscous flows. Journal of Computational Physics, 332:99–117, 2017.

67. Mullen, J. S. and Fischer, P. F.: Filtering techniques for complex geometry fluid flows. Communications in Numerical Methods in Engineering, 15(1):9–18, 1999.

68. Hesthaven, J. and Warburton, T.: Nodal discontinuous Galerkin Methods: algorithms, analysis, and applications. Berlin, Springer-Verlag, 2008.

69. Corr, P., Stewart, D., Hanna, P., Ming, J., and Smith, F. J.: Discrete Chebyshev transform. A natural modification of the DCT. In Proceedings. 15th International Conference on Pattern Recognition, volume 3, pages 1142–1145. IEEE, 2000.

70. FFTW documentations: 1d Real-even DFTs (DCTs). `http://www.fftw.org/fftw3_doc/1d-Real_002deven-DFTs-_0028DCTs_0029.html`, Accessed: 2017-09-07.

71. Fischer, P. F., Kruse, G. W., and Loth, F.: Spectral element methods for transitional flows in complex geometries. Search Results Journal of Scientific Computing, 17(1):81–98, 2002.

72. Blaisdell, G. A., Mansour, N. N., and Reynolds, W. C.: Compressibility effects on the growth and structure of homogeneous turbulent shear flow. Journal of Fluid Mechanics, 256:443–485, 1993.

73. Blaisdell, G. A., Mansour, N. N., and Reynolds, W. C.: Numerical simulation of compressible homogeneous turbulence. Advances in Compressible Turbulent Mixing TF-50, Stanford University, Stanford, CA, 1992.

74. Jacobs, G. B., Kopriva, D. A., and Mashayek, F.: Validation study of a multidomain spectral code for simulation of turbulent flows. AIAA Journal, 43(6):1256–1264, 2005.

75. Gullbrand, J.: Explicit filtering and subgrid-scale models in turbulent channel flow. Annual Research Briefs, Center for Turbulence Research, Stanford University, pages 31–42, 2001.

76. FFT benchmark results. `http://http://www.fftw.org/speed/`, Accessed: 2017-09-07.

77. Eaton, J. K.: Turbulent flow reattachment: an experimental study of the flow and structure behind a backward-facing step. Doctoral dissertation, Stanford University, 1980.

78. Armaly, B. F., Durst, F., Pereira, J. C. F., and Schonung, B.: Experimental and theoretical investigation of backward-facing step flow. Journal of Fluid Mechanics, 127:473–496, 1983.

79. Durst, F. and Tropea, C.: Turbulent, backward-facing step flows in two-dimensional ducts and channels. In Proceedings of 3rd Intl. Symp. on Turbulent Shear Flows, pages 18.1–18.5, Davis, CA, 1981. University of California.

80. Adams, E. W., Johnston, J. P., and Eaton, J. K.: Experiments on the structure of turbulent reattaching flow. Thermosciences Division, Department of Mechanical Engineering Report MD-43, Stanford University, Palo Alto, CA, 1984.

81. Ishomoto, K. and Honami, S.: The effect of inlet turbulence intensity on the reattachment process over a backward-facing step. ASME Journal of Fluids Engg, 111:87–92, 1989.

82. Kim, J. and Moin, P.: Application of a fractional-step method to incompressible Navier-Stokes equations. Journal of Computational Physics, 59:308–323, 1985.

83. Kaiktsis, L., Karniadakis, G. E. M., and Orszag, S. A.: Onset of three-dimensionality, equilibria, and early transition in flow over a backward facing step. Journal of Fluid Mechanics, 231:501–528, 1991.

84. Kaikatis, L., Karniadakis, G. E., and Orszag, S. A.: Unsteadiness and convective instabilities in a two-dimensional flow over a backward-facing step. Journal of Fluid Mechanics, 321:157–187, 1996.

85. Le, H., Moin, P., and Kim, J.: Direct numerical simulation of turbulent flow over a backward-facing step. Journal of Fluid Mechanics, 330:349–374, 1997.

86. Jovic, S. and Driver, M.: Backward-facing step measurements at low Reynolds number, Re_h=5000. NASA TM 108807, February 1994.

87. Wengle, H., Huppertz, A., Barwolff, G., and Janke, G.: The manipulated transitional backward-facing step flow: An experimental and direct numerical simulation investigation. European Journal of Mechanics - B/Fluids, 20:25–46, 2001.

88. Barkley, D., Gomes, M. G. M., and Henderson, R. D.: Three-dimensional instability in flow over a backward-facing step. Journal of Fluid Mechanics, 473:167–190, 2002.

89. Le, H.: Direct numerical simulation of turbulent flow over a backward-facing step. Doctoral dissertation, Stanford University, 1995.

90. Spalart, P. R.: Direct simulation of a turbulent boundary layer up to $Re = 1410$. Journal of Fluid Mechanics, 187:61–98, 1988.

91. Kanchi, H., Sengupta, K., and Mashayek, F.: Effect of turbulent inflow boundary condition in LES of flow over a backward-facing step using spectral element method. International Journal of Heat and Mass Transfer, 62:782–793, 2013.

92. Liu, H., Wang, B., Guo, Y., Zhang, H., and Lin, W.: Effects of inflow mach number and step height on supersonic flows over a backward-facing step. Advances in Mechanical Engineering, 5:147916, 2013.

93. Pope, S. B.: Turbulent Flows. Cambridge, UK, Cambridge University Press, 2000.

94. Rogallo, R. S. and Moin, P.: Numerical simulation of turbulent flow. Annual Review of Fluid Mechanics, 16:99–137, 1984.

95. Lilly, D. K.: The representation of small-scale turbulence in numerical simulation experiments. In Proceedings of IBM Scientific Computing Symposium Environmental Sciences, pages 195–210. IBM Form No. 320-1951, 1967.

96. Moin, P. and Kim, J.: Numerical investigation of turbulent channel flow. Journal of Fluid Mechanics, 118:341–377, 1982.

97. Piomelli, U. and Zang, T. A.: Large eddy simulation of transitional channel flow. Computer Physics Communications, 65:224–230, 1991.

98. Van Driest, E. R.: On turbulent flow near a wall. Journal of the Aeronautical Sciences, 23(11):1007–1011, 1956.

99. Germano, M.: Turbulence: The filtering appraoch. Journal of Fluid Mechanics, 238:325–336, 1992.

100. Piomelli, U.: Applications of large-eddy simulations in Engineering-An overview. In Large Eddy Simulations of Complex Engineering and Geophysical Flows, eds. B.

Galperin and S. A. Orszag, chapter 6, pages 119–137. Cambridge, U.K., Cambridge University Press, 1993.

101. Ghiasi, Z. and Mashayek, F.: Improved smagorinsky-lilly model for turbulent flow over backward-facing step. In The 7th International ENERGY Conference & Workshop, 2017.

102. Ghiasi, Z., Li, D., Komperda, J., and Mashayek, F.: Large eddy simulation of supersonic cold flow in ramp-cavity combustor with fuel injector. In APS Division of Fluid Dynamics Meeting Abstracts, 2015.

103. Ghiasi, Z., Li, D., Komperda, J., and Mashayek, F.: Large-eddy simulation of turbulent supersonic cold flow in ramp-cavity combustor with injector. In 15th European Turbulence Conference, 2015.

104. Jacobson, L., Gallimore, S., Schetz, J., O'Brien, W., and Goss, L.: Improved aerodynamic-ramp injector in supersonic flow. Journal of Propulsion and Power, 19(4):663–673, 2003.

105. Maddalena, L., Campioli, T., and Schetz, J.: Experimental and computational investigation of light-gas injectors in a mach 4.0 crossflow. Journal of Propulsion and Power, 22:1027–1038, 2006.

106. Doster, J., King, P., Gruber, M., Carter, C., Ryan, M., and Hsu, K.: In-stream hypermixer fueling pylons in supersonic flow. Journal of Propulsion and Power, 25(4):885–901, 2009.

107. Gruber, M., Baurle, R., Mathur, T., and Hsu, K.-Y.: Fundamental studies of cavity-based flameholder concepts for supersonic combustors. Journal of Propulsion and power, 17(1):146–153, 2001.

108. Gruber, M. R., Donbar, J. M., Carter, C. D., and Hsu, K.-Y.: Mixing and combustion studies using cavity-based flameholders in a supersonic flow. Journal of Propulsion and Power, 20(5):769–778, 2004.

109. Rasmussen, C., Dhanuka, S., and Driscoll, J.: Visualization of flameholding mechanisms in a supersonic com- bustor using plif. Proceedings of the Combustion Institute, 31:2505–2512, 2007.

110. Hsu, K.-Y., Carter, C., Gruber, M., Barhorst, T., and Smith, S.: Experimental study of cavity-strut combustion in supersonic flow. Journal of Propulsion and Power, 26(6):1237–1246, 2010.

111. Krivodonova, L.: Limiters for high order discontinuous galerkin methods. Journal of Computational Physics, 226:879–896, 2007.

112. Qiu, J. X. and Shu, C. W.: Runge-kutta discontinuous galerkin method using weno limiters. SIAM Journal on Scientific Computing, 26:907–929, 2005.

113. Qiu, J. X. and Shu, C. W.: Hermite weno schemes and their application as limiters for rungekutta discontinuous galerkin method ii: Two dimensional case. Computers & Fluids, 34:642–663, 2005.

114. Guermond, J. L., Pasquetti, R., and Popov, B.: Entropy viscosity method for nonlinear conservation laws. Journal of Computational Physics, 230:4248–4267, 2011.

115. Abbassi, H., Komperda, J., Mashayek, F., and Jacobs, G.: Application of entropy viscosity method for supersonic flow simulation using discontinuous spectral element method. In AIAA Paper, number 2012-1115, 2012.

116. Ducros, F., Ferrand, V., Nicoud, F., Weber, C., Darracq, D., Gacherieu, C., and Poinsot, T.: Large-eddy simulation of the shock/turbulence interaction. Journal of Computational Physics, 152(2):517–549, 1999.

117. Peterson, D. M., Hagenmaier, M. A., Carter, C. D., and Tuttle, S. G.: Hybrid Reynolds-averaged and large-eddy simulations of a supersonic cavity flameholder. In 43rd AIAA Fluid Dynamics Conference, number 2013-2483, 2013.

118. Green, J. E.: Interactions between shock waves and turbulent boundary layers. Progress in Aerospace Sciences, 11:235, IN9, 261–260, IN10, 340, 1970.

119. Ghiasi, Z., Komperda, J., and Mashayek, F.: Simulation of reacting flow with a discontinuous spectral element method. In APS Division of Fluid Dynamics Meeting Abstracts, 2013.

120. Ghiasi, Z. and Mashayek, F.: Subsonic slanted cavity combustor simulation with a discontinuous spectral element method. In 11th World Congress on Computational Mechanics (WCCM XI), 2014.

121. Ghiasi, Z., Komperda, J., Li, D., and Mashayek, F.: Simulation of subsonic turbulent reacting flow in scramjet with ethylene injector. In 12th World Congress on Computational Mechanics (WCCM XII), 2016.

122. Schlichting, H., Gersten, K., Krause, E., Oertel, H., and Mayes, K.: Boundary-Layer Theory, volume 7. Springer, 1955.

123. International Journal of Heat and Mass Transfer. `https://www.journals.elsevier.com/international-journal-of-heat-and-mass-transfer/`, Accessed: 2018-05-09.

VITA

Name	Zia Ghiasi

Education
B.Sc., Mechanical Engineering
University of Tehran, Tehran, Iran, 2011
M.Sc., Mechanical Engineering
University of Illinois at Chicago, Chicago, Illinois, United States, 2017
Ph.D., Mechanical Engineering
University of Illinois at Chicago, Chicago, Illinois, United States, 2018

Experience
Research/Teaching Assistant, University of Illinois at Chicago, 2012-2018
Research Assistant, Illinois Institute of Technology, 2011-2012
Teaching Assistant, University of Tehran, 2010-2011

Membership
American Physical Society (APS)
American Institute of Aeronautics and Astronautics (AIAA)

Abstracts
Ghiasi, Z., Mashayek, F.: Improved Smagorinsky-Lilly Model for Turbulent Flow Over Backward-facing Step. The 7th International ENERGY Conference & Workshop, 2017.

Ghiasi, Z., Komperda, J., Li, D., Mashayek, F.: Simulation of Subsonic Turbulent Reacting Flow in Scramjet with Ethylene Injector. 12th World Congress on Computational Mechanics (WCCM XII), 2016.

Ghiasi, Z., Li, D., Komperda, J., Mashayek, F.: Large Eddy Simulation of Supersonic Cold Flow in Ramp-Cavity Combustor with Fuel Injector. APS Division of Fluid Dynamics Meeting, 2015.

Ghiasi, Z., Li, D., Komperda, J., Mashayek, F.: Large-eddy Simulation of Turbulent Supersonic Cold Flow in Ramp-cavity Combustor With Injector. 15th European Turbulence Conference, 2015.

Ghiasi, Z., Komperda, J., Mashayek, F.: Simulation of Supersonic Reactive Flow in Ramped Cavity Combustor with Fuel Injector. APS Division of Fluid Dynamics Meeting, 2014.

Ghiasi, Z., Mashayek, F.: Subsonic Slanted Cavity Combustor Simulation With a Discontinuous Spectral Element Method. 11th World Congress on Computational Mechanics (WCCM XI), 2014.

Ghiasi, Z., Komperda, J., Mashayek, F.: Simulation of Reacting Flow with a Discontinuous Spectral Element Method. APS Division of Fluid Dynamics Meeting, 2013.

Publications   **Ghiasi, Z.**, Li, D., Komperda, J., and Mashayek, F.: Near-Wall Resolution Requirement for Direct Numerical Simulation of Turbulent Flow Using Multidomain Chebyshev Grid. International Journal of Heat and Mass Transfer, 126, Part B:746 760, 2018.

Ghiasi, Z., Komperda, J., Li, D., and Mashayek, F.: Modal explicit filtering for large eddy simulation in discontinuous spectral element method. *Under Revision.* Journal of Computational Physics, 2018.

Ghiasi, Z., Li, D., Komperda, J., and Mashayek, F.: Wall Resolution Study For Direct Numerical Simulation Of Turbulent Channel Flow Using A Multidomain Chebyshev Grid. Tenth International Symposium on Turbulence and Shear Flow Phenomena, 2017.

Li, D., **Ghiasi, Z.**, Komperda, J., and Mashayek, F.: A Numerical Study of Compressibility Effects in Turbulent Mixing Layer. Tenth International Symposium on Turbulence and Shear Flow Phenomena, 2017.

Ghiasi, Z., Komperda, J., Li, D., and Mashayek, F.: Simulation of supersonic turbulent non-reactive flow in ramp-cavity combustor using a discontinuous spectral element method. AIAA Paper, number 2016-0617, 2016.

Li, D., **Ghiasi, Z.**, Komperda, J., and Mashayek, F.: The effect of inflow mach number on the reattachment in subsonic flow over a backward-facing step. AIAA Paper, number 2016-2077, 2016.

Komperda, J., **Ghiasi, Z.**, Li, D., Mashayek, F., Irannejad, A., and Jaberi, F.A.: Simulation of the Cold Flow in a Ramp-Cavity Combustor Using a DSEM-LES/FMDF Hybrid Scheme. AIAA Paper, number 2016-1938, 2016.

Komperda, J., **Ghiasi, Z.**, Mashayek, F., Irannejad, A., and Jaberi, F.A.: Filtered Mass Density Function for Use in Discontinuous Spectral Element Method. AIAA Paper, number 2014-3471, 2014.